



HAL
open science

New way of synthesis of uniform gold nanoparticles for the detection of few molecules

Rana Omar

► **To cite this version:**

Rana Omar. New way of synthesis of uniform gold nanoparticles for the detection of few molecules. Material chemistry. Université de Lorraine, 2017. English. NNT : 2017LORR0364 . tel-01810729

HAL Id: tel-01810729

<https://theses.hal.science/tel-01810729>

Submitted on 8 Jun 2018

HAL is a multi-disciplinary open access archive for the deposit and dissemination of scientific research documents, whether they are published or not. The documents may come from teaching and research institutions in France or abroad, or from public or private research centers.

L'archive ouverte pluridisciplinaire **HAL**, est destinée au dépôt et à la diffusion de documents scientifiques de niveau recherche, publiés ou non, émanant des établissements d'enseignement et de recherche français ou étrangers, des laboratoires publics ou privés.



AVERTISSEMENT

Ce document est le fruit d'un long travail approuvé par le jury de soutenance et mis à disposition de l'ensemble de la communauté universitaire élargie.

Il est soumis à la propriété intellectuelle de l'auteur. Ceci implique une obligation de citation et de référencement lors de l'utilisation de ce document.

D'autre part, toute contrefaçon, plagiat, reproduction illicite encourt une poursuite pénale.

Contact : ddoc-theses-contact@univ-lorraine.fr

LIENS

Code de la Propriété Intellectuelle. articles L 122. 4

Code de la Propriété Intellectuelle. articles L 335.2- L 335.10

http://www.cfcopies.com/V2/leg/leg_droi.php

<http://www.culture.gouv.fr/culture/infos-pratiques/droits/protection.htm>

THÈSE EN COTUTELLE

Pour obtenir le grade de Docteur délivré par

Université de Lorraine

et

Université Libanaise

Discipline : chimie-physique

présentée et soutenue publiquement par

OMAR Rana

Le 21 Décembre 2017

**New way of synthesis of uniform gold nanoparticles for
the detection of few molecules**

Jury

Pr. Pierre-Michel Adam	Université de technologie de Troyes	Rapporteur
Pr. Michel Voué	Université de Mons	Rapporteur
Dr. Safi Jradi	Université de technologie de Troyes	Examineur
Pr. Fawaz El Omar	Université Libanaise	Invité

Directeurs de thèse (Université Libanaise) :

Pr. Joumana Toufaily et Dr. Hussien Mortada

Directeurs de thèse (Université de Lorraine) :

Dr. Akil Suzanna et Pr. Aotmane En Naciri

Acknowledgment

First and foremost, I thank God for letting me through all the difficulties. I have your guidance day by day. Thank you Allah for always being there for me.

I would like to offer my extreme thankfulness to my father, mother, and my brothers who stood beside me and supported me throughout the period of my research journey. In particular, I owe a lot to my parents who encouraged and helped me at every stage of my personal and academic life and longed to see this achievement come true. A special thanks to all my family members, especially my two grandmothers whose prayer sustained me this far.

I would also like to thank the committee members for the time and efforts given to evaluate my work: Pr. Michel Voué, Pr. Pierre-Michel Adam and Dr. Safi Jradi. Thank you for your helpful comments and suggestions.

I gratefully acknowledge the funding sources that made my Ph.D. work possible. Very special thanks to the "Lebanese University" and the "Association of Specialization and Scientific Orientation" for their financial support during all my stay in France.

I express my deepest thanks to my two supervisors Prof. Aotmane En Naciri and Dr. Suzanna Akil for accepting me in their group and giving me their time to hear, guide, keep me on the right track and give me the necessary advice required for the birth of this project.

My sincere gratitude goes to Pr. Aotmane for the continuous support of my Ph.D study and research, for his patience, motivation, and immense knowledge. I choose this moment to express my sincere appreciations for his significant effort in Ellipsometry and optical analysis. I learned from him how to be well organized and how to respect time. He gave me the moral support and the freedom I needed to move on during the most difficult times.

The enthusiasm, good advice and friendship of my supervisor, Dr. Suzanna, has been invaluable on both the research and the personal level, for which I am extremely grateful. It has been an honor to be her first Ph.D. student. I remember she used to say something like: "be unique and leave something special about you" to encourage me to add something new into my research work and to defend my thoughts and ideas. She has been supportive since the first days I arrived to France and entered the Lab. I would also like to thank her for encouraging my research in nanotechnology and plasmonics and for allowing me to grow as a researcher with great experience in writing and oral presentations. I will never forget the weekends we spent together with her family. Thank you Dr.!

I am also grateful for having a chance to meet so many wonderful people and professionals, who supported me throughout the period I had during this project. First, I thank Dr. Yann Battie

who was very kind and patient and always willing to lend his service whenever needed. Working with you Yann was a great experience. Special thanks to Pascal Franchetti who helped me in performing Raman experiments. I will never forget the best moments during the coffee time with the team members Christian Louis, José Lopez, Laurent Broch and Clarice Perrin-Mozet. Thank you all. The thesis would not have come to a successful completion, without the help I received from the staff of the Russian center, University of Troyes and Georgia tech to perform my SEM images.

My deepest gratitude goes to Pr. Olivier Pages for his support and guidance in our Lab (LCP-A2MC). I choose this moment to acknowledge his contribution gratefully.

I express my warm thanks to Dr. Fawaz Al Omar; Dean of Lebanese Doctoral School, for taking part in useful decisions and arranging all facilities to make my defense easier in France. Thank you for attending my defense.

I also want to thank all my friends who encouraged me to enrich my knowledge and to strive towards my goal. Special thanks to my friends Samah, Hadil, Mouhammad, Hassan and Ali for helping me get through the difficult times, and for all the emotional support, camaraderie, entertainment, and caring they provided. I can't list all the names here, but you are always on my mind.

I am also extremely thankful to my honest friend Jennifer who was always supportive and taking care of me. Your presence gave me the confident I needed to pass my defense. You proved for me that true friends still exist. I am also indebted to you not only for your help and support during my defense but also for leaving your work and travelling from Dubai to France just to be next to me. I love so much sister and I appreciate all what you've made to me.

And finally to Issraa, my closest friend who has been by my side throughout this PhD journey, living every single minute of it. We shared together the same lab, office and even the same supervisor. I'll never forget the daily lunches, dinners, fun activities and discussions we've done together. Thank you Issraa for being there to listen when I needed an ear. I am thankful for you for every single moment you let me smile from the bottom of my heart. My time at Metz was made enjoyable due to the many friends and families that became a part of my life. I would like to thank all of them for their services.

This thesis is only a beginning of my journey.

Rana OMAR

Abstract

Controlled synthesis of metallic nanoparticles (MNPs), according to particular morphologies and dimensions, is an interdisciplinary field of research because of the new, varied, rich and complex physical properties of MNPs. These properties are mainly governed by the collective oscillations of conduction electrons called plasmons.

This phenomenon is optically reflected by the sensitivity of the MNPs to the change in the surrounding refractive index and by the shift of their plasmon resonance band. This feature, according to the morphology of MNPs, is used in fairly modern applications such as cancer phototherapy and the development of the ultrasensitive sensors based on Surface Plasmon Resonance (SPR) or Surface Enhanced Raman Spectroscopy (SERS).

The sensitivity of MNPs as sensors is not only directly related to the chemical and crystalline nature of the metal but also to their ability to adsorb target molecules, absorb and/or confine and enhance incident light. This last property is generally more remarkable as the distance separating the MNPs is small. Thus, the control of the size, shape and density of the MNPs is of major interest. Therefore, the development of new synthesis methods of MNPs is still relevant.

Moreover, the fabrication of uniform metallic nanoparticles is mainly achieved by colloidal synthesis particularly by "seed mediated growth". On the other hand, this method always has certain limitations in the preparation time and the control of the size and shape. In this context, we have, in this thesis, developed a new fabrication method of MNPs of different shapes. The idea is to structure a polymer (PMMA) in the form of a nanoporous film and to use the nanopores as synthesis reactor for MNPs. Thus, the objective of this thesis was to investigate the proposed synthesis method in order to develop new detection nanosensors based on SERS phenomenon.

The work in this thesis has been divided into three main parts: the first is to study the synthesis mechanism in order to optimize the formation process of uniform metallic structures. The second aims to change the shape of the MNPs by playing on the parameters of synthesis. In parallel with these two aspects, an important task was devoted to morphological analysis using structural analysis techniques, and to the determination and the modelling of the optical responses of these MNPs particularly by the technique of spectroscopic ellipsometry.

Résumé en français

La synthèse contrôlée de nanoparticules métalliques (NPM) selon des morphologies et dimensions particulières est un domaine de recherche interdisciplinaire en raison des nouvelles propriétés physiques variées, riches et complexes des NPM. Ces propriétés sont principalement régies par les oscillations collectives des électrons de conduction appelées « plasmons ».

Ce phénomène se traduit optiquement par une sensibilité des NPM au moindre changement d'indice de réfraction par déplacement de leur bande de résonance plasmon. Ce phénomène en fonction de la morphologie des NPM est mis à profit dans applications assez modernes telles que la photothérapie contre le cancer et l'élaboration de capteurs ultrasensibles basés sur la Résonance Plasmon de Surface (SPR) ou sur la Spectroscopie d'Exaltation Raman de Surface (SERS).

La sensibilité des NPM en tant que capteurs est directement liée à la nature chimique et cristalline du métal mais également à leur capacité à adsorber les molécules cibles, à absorber ou/et confiner et exalter la lumière incidente. Cette dernière propriété est généralement d'autant plus remarquable que la distance séparant les NPM est petite. Ainsi, le contrôle de la taille, forme et densité des NPM présente un intérêt majeur et les travaux visant à développer de nouvelles méthodes de fabrication ou de nano-structuration sont toujours d'actualité.

D'ailleurs, la fabrication de nanoparticules métalliques (NPM) uniformes se fait principalement par synthèse colloïdale particulièrement par « seed mediated growth ». En revanche, cette méthode présente toujours certaines limitations dans le temps de préparation et le contrôle de taille et de forme. Dans ce contexte, nous avons, dans cette thèse, développé une nouvelle méthode de fabrication de nanoparticules métalliques (NPM) de différentes formes. Le principe consiste à structurer un polymère (PMMA) sous forme d'un film nanoporeux et d'utiliser les nanopores comme réacteur de synthèse de NPM. C'est ainsi que l'objectif de cette thèse était d'exploiter la méthode de fabrication ainsi proposée afin d'élaborer **de nouveaux nano-capteurs de détection** basés sur le SERS.

Les travaux dans le cadre de cette thèse ont été répartis sur trois grands volets : Le premier consiste à étudier le mécanisme de synthèse afin d'optimiser le processus de formation des structures métalliques uniformes. Le 2ème vise à faire évoluer la forme des NPM en jouant sur les paramètres de synthèse. En parallèle à ces deux volets, une tâche importante a été consacrée à l'analyse morphologique en utilisant les techniques d'analyses structurales, et à la détermination et la modélisation des réponses optiques de ces NPMs notamment par la technique d'ellipsométrie spectroscopique.

Publications

Omar, R., Naciri, A. E., Jradi, S., Battie, Y., Toufaily, J., Mortada, H., & Akil, S. (2017). One-step synthesis of a monolayer of monodisperse gold nanocubes for SERS substrates. *Journal of Materials Chemistry C*, 2017, 5, 10813 – 10821.

Contributions at national and international conferences

"Polymer self-assembly induced the formation of monodisperse gold nanoparticles" Akil S., Omar R., Battie Y., Toufaily J., Mortada H., Jradi S., En Naciri A. GDR Or-Nano, 12-14 Juin, Nancy, (2017) GDR Or-Nano, 12-14 June, Nancy, (2017).

"New Approach for the Synthesis of Uniform Gold Nanoparticles". Omar, R., Naciri, A. E., Jradi, S., Battie, Y., Toufaily, J., Mortada, H., & Akil, S. 15^{ème} journée de la matière condensée (JMC15), August 22-26, Bordeaux (2016).

"New Approach for the Synthesis of Uniform Gold Nanoparticles". Omar R., Akil S., Jradi S., En Naciri A., Toufaily J., Hamieh T., Mortada H. 9th International Conference on Material Sciences (CSM9), August 26-28, Nancy, France (2015).

Table of contents

Table of contents	1
List of figures	3
List of tables	8
List of schemes	8
List of abbreviations	9
General Introduction	10
1 Bibliographic study	12
1.1 Introduction	12
1.2 General shape-controlled synthesis strategies of metallic nanoparticles.....	13
1.2.1 Top-down synthesis.....	13
1.2.1.1 Physical top-down synthesis	13
1.2.1.2 Chemical top-down synthesis	15
1.2.1.3 Deposition methods	17
1.2.2 Bottom-up pathways	19
1.2.2.1 Colloidal synthetic strategies	19
1.2.2.2 Electrochemical synthesis	24
1.2.3 Self-assembly	24
1.3 Conclusion	32
1.4 References	33
2 Shape-controlled synthesis of gold nanoparticles	44
2.1 Introduction	44
2.2 Synthesis method of gold nanocubes.....	44
2.3 Development of polymer-self-assembly based synthesis of GNCs	46
2.4 Experimental section.....	47
2.4.1 Synthesis process.....	47
2.4.2 Substrate cleaning process	48
2.4.3 Characterization of GNCs	48
2.5 Results and Discussions: experimental approach to synthesize gold nanocubes	49
2.5.1 Adjustment of the concentration of gold precursor.....	49
2.5.2 Role of the solvents evaporation rate in GNCs synthesis.....	65
2.6 Conclusion	69
2.7 References	69
3 Synthesis strategy of gold nanoparticles with different shapes.....	73
3.1 Introduction	73
3.2 Shape-controlled nanotechnologies of metallic nanoparticles	74
3.2.1 Overview of colloidal synthesis of monodispersed metal nanoparticles	75

3.3	Development of shape-controlled synthesis of gold nanoparticles	79
3.3.1	Understanding the role of PMMA solvent (polymer solvent).....	81
3.3.2	Understanding the role of gold precursor solvent (polymer non-solvent)	84
3.3.3	Role of the gold precursor molecule	86
3.4	Improving the SERS enhancement through shape control	89
3.5	Conclusion	91
3.6	References	92
4	Optical properties of self-assembled gold nanoparticles.....	95
4.1	Introduction	95
4.2	Ellipsometry technique	96
4.2.1	Modeling	99
4.2.2	Ellipsometric data analysis.....	101
4.3	Results and Discussions.....	102
4.3.1	Optimizing the mechanical parameters	102
4.3.1.1	Effect of the speed (in NaAuCl ₄ / MIBK/ethanol).....	102
4.3.1.2	Effect of the speed (in NaAuCl ₄ /acetone/ethanol).....	107
4.3.2	Optical properties of shape-controlled gold nanoparticles (GNPs).....	113
4.3.2.1	Control the formation of uniform gold nanocubes (GNCs).....	114
4.3.2.2	Control the formation of non-cubic shapes: gold nanohexagons (GNHs) and gold nanotriangles (GNTs).....	119
4.4	Conclusion	128
4.5	References	129
5	Summary, conclusions and perspectives	132
5.1	Summary and conclusions	132
5.2	Future work and perspectives	133
	Appendix	135

List of figures

Fig. 1 Schematic illustration for the fabrication method of GNPs using EBL. Adapted from ref. [33].	15
Fig. 2 Schematic representation for the fabrication of 3D etch pit array on silicon substrate through the usage of a block copolymer as template and an aqueous solution of Hydrofluoric acid (HF) as etchant. Adapted from ref. [34]	17
Fig. 3 Generalized two-step mechanism for solution-phase Au nanoparticle synthesis. [84].	21
Fig. 4 Schematic representation for the generation of Gold Nanorods. [91]	22
Fig. 5 Schematic illustration for different stages of growth of Gold Nanorods using small (5.5 nm) and large size (8 nm) seeds. [91]	23
Fig. 6 Schematic representation of particle-loaded PS-b-P4VP micelles formed in a selective solvent (Toluene) for the PS block through controlling the morphology of the micelle upon addition of co-solvent (H ₂ O). [120]	27
Fig. 7 Vesicles loaded with metal nanoparticles are prepared in solution and regular honeycomb structures are fabricated via spin-coating. Nanostructured thin films of the inorganic material are obtained after oxygen plasma etching. Depending on the diameter of the vesicles large (b) or small (c) honeycomb patterns can be fabricated. The structure is preserved during O ₂ plasma etching (d). The insets in b-d are optical photographs of water droplets on top of the films indicating hydrophobic surface properties. Adapted from ref [120].	29
Fig. 8 Schematic illustration for DNA hybridization (interaction between cationic NPs and anionic DNA). [154], [155]	30
Fig. 9 Schematic representation of DNA mediated growth mechanism of Au Nanoprisms into different shapes in two Stages: Shape control followed by thickness growth. [156]	31
Fig. 10 Schematic representation of interactions of biotinylated GNPs with streptavidin: assembly and disassembly. [109]	32
Fig. 11 AFM images of GNPs obtained with different concentrations of gold precursor (40, 50, 60, 80 and 100 mM). The scale bar is 500 nm.	50
Fig. 12 SEM micrographs of GNPs obtained with different gold precursor concentrations (40, 50, 60, 80 and 100 mM). This scale bar is 100 nm.	50
Fig. 13 Histogram of nanocubes size distribution and its corresponding Gaussian fit for the 80 mM Au ³⁺ substrate.	51
Fig. 14 Dark-field light scattering images of GNCs obtained with different gold precursor concentrations (40, 50, 60, 80 and 100 mM). Scale bar corresponds to 1 μ m.	52
Fig. 15 Extinction cross section spectra for single and dimer of GNC calculated by BEM. Nanocube size is 65 nm and the gap between the dimer is 10 nm.	53
Fig. 16 Ellipsometric angles (Δ and ψ) values over increasing Au ³⁺ concentration measured at incident angle of 70°.	55
Fig. 17 Thickness of PMMA thin layer as determined by experimental ellipsometric measurements.	56
Fig. 18 Comparison between measured and calculated ellipsometric angles (Ψ and Δ) of a sample prepared with 80 mM of Au ³⁺ .	57
Fig. 19 Absorption coefficient of GNPs obtained with different gold precursor concentrations (40, 50, 60, 80 and 100 mM). The spectra were extracted from the analysis of ellipsometry data.	58

Fig. 20 SERS spectra of pyridine 10^{-5} M obtained during 10 sec for: (a) 5 different drops deposited on the surface of the 100mM substrate and (b) 3 independently repeated same samples.	60
Fig. 21 (a) Average Raman spectra of pyridine 1 M and SERS ones of pyridine 10^{-5} and 10^{-12} M obtained with 100 mM of Au^{3+} , the inset shows the pyridine molecule. (b) SPR band of the corresponding substrate as obtained by ellipsometry, the inset show the SEM micrograph of the corresponding substrate.	61
Fig. 22 SERS intensity of the 1023 and 1050 cm^{-1} bands as a function of pyridine concentration obtained for the 50 mM substrate during 10 sec.	62
Fig. 23 SERS intensity of the 1023 cm^{-1} band and SPR plasmon band as a function of gold precursor concentration obtained with 10^{-5} M pyridine during 10 sec.	63
Fig. 24 Average Raman spectra of 4,4-bipyridine 10^{-2} M and SERS of 4,4-bipyridine 10^{-5} M obtained with 100 mM of Au^{3+} , the inset shows a zoom in the 4,4-BP Raman spectrum.	64
Fig. 25 SEM images showing the influence of the evaporation rate on the size distribution of the gold nanoparticles (40 mM gold precursor).	66
Fig. 26 SEM images showing the influence of increasing the evaporation rate on the size distribution of the gold nanoparticles (40 mM gold precursor).	68
Fig. 27 Schematic representation of general synthesis approaches for size and shape control of metal nanoparticles combining with the LaMer diagram. Adapted from ref. [13]	76
Fig. 28 Illustration of the seed-mediated growth process to produce gold nanorods with different aspect ratios. Adapted from ref. [14].....	77
Fig. 29 Illustration of seed-mediated growth mechanism allowing the synthesis of metal nanorods of different aspect ratios through adjusting the surfactant amount (adapted from ref. 14).....	77
Fig. 30 General rules of shape-control in silver-assisted seed-mediated gold nanoparticles synthesis, where the shape of nanoparticles can be controlled simply by altering the reaction rate or the silver concentration. Ref. [18].....	78
Fig. 31 TEM images of shape controlled Pt nanoparticles: a) Pt cubes, b) Pt cuboctahedra, c) Pt octahedra, d) Pd triangular plates, e) Pd hexagonal plates, f) Pd nanobars, and g) Pd-Pt bimetallic nanodendrites. Adapted from ref. 21.....	79
Fig. 32 AFM images of 100 mM gold precursor ($\text{NaAuCl}_4 \cdot 2\text{H}_2\text{O}$) in different PMMA solvents; in acetone (a, b) and in MIBK (c, d). Images taken in contact mode at same spin coating parameters and different scan sizes. (5 and 10 μm).	82
Fig. 33 SEM images for 100 mM gold precursor ($\text{NaAuCl}_4 \cdot 2\text{H}_2\text{O}$ /ethanol dispersion) in different PMMA solvents; (a) & (b) sample prepared with MIBK. The insert in (a) corresponds to small scan size images of the same sample and (b) corresponds also to the same sample observed with high magnification in order to observe a single nanocube. (c) and (d) samples prepared with acetone.....	83
Fig. 34 SEM images for 100 mM gold precursor ($\text{HAuCl}_4 \cdot 2\text{H}_2\text{O}$ /ethanol) in different PMMA solvents; (a) & (b) sample prepared with MIBK observed by two different magnifications. (c) and (d) sample prepared with acetone.....	84
Fig. 35 SEM images for 100 mM gold precursor ($\text{NaAuCl}_4 \cdot 2\text{H}_2\text{O}$ /acetone) in two different precursor solvents; (a) sample prepared with ethanol. (b) sample prepared with isopropanol.85	
Fig. 36 SEM images for 100 mM gold precursor ($\text{HAuCl}_4 \cdot 2\text{H}_2\text{O}$ /acetone) in two different precursor solvents; (a) sample prepared with ethanol. (b) sample prepared with isopropanol.86	

Fig. 37 SEM images for samples prepared with acetone (PMMA solvent)/isopropanol (precursor solvent) combination with three different precursor molecules; (a) NaAuCl ₄ , (b) HAuCl ₄ and (c) KAuCl ₄	88
Fig. 38 Absorption spectra of gold nanoparticles prepared with different experimental conditions. (Black spectrum) polydispersed nanohexagons, (red spectrum) monodispersed nanocubes, (green spectrum) nanohexagons and nanotriangles and (blue spectrum) monodispersed sharp nanocubes.	90
Fig. 39 SERS and Raman spectra of Pyridine for samples shown in Fig. 38. All these samples have the same coating parameters and same gold precursor concentration (100 mM). 10 μ l drop of pyridine (10 ⁻⁵ M for SERS and 1 M for Raman)	91
Fig. 40 Schematic view of the UVISEL spectroscopic ellipsometer.	97
Fig. 41 Measurement of ellipsometric parameters of Ψ (blue curve) and Δ (red curve).The measurements are performed at an angle of incidence 60° on a silicon substrate coated with GNPs (40 mg of NaAuCl ₄ / MIBK/ethanol) at 10000 rpm.....	98
Fig. 42 (a) AFM image of GNPs loaded PMMA holes over a silicon substrate (image taken in contact mode). (b) SEM image showing clearly the GNPs inside the PMMA holes. The two samples are prepared according to the physio-chemical synthesis method that was introduced in chapter 2 (40 mg of NaAuCl ₄ / MIBK/ethanol using 10000 rpm).....	98
Fig. 43 Schematic representation for the physical model used ellipsometry data analysis....	100
Fig. 44 Ellipsometric spectrum of the experimental parameters (Ψ_{exp}) and (Δ_{exp}) values (scattered lines) compared with fitted ones (Ψ_{model} and Δ_{model}) (solid lines). The measurements are performed at an angle of incidence 60° on a silicon substrate coated with GNPs (40 mg of NaAuCl ₄ / MIBK/ethanol using 10000 rpm).	101
Fig. 45 Evolution of AFM images of GNPs using 40 mg of NaAuCl ₄ /ethanol/MIBK at increased ERs: (a) 2000 rpm, (b) 5000 rpm and (c) 10000 rpm. Images scanned in non-contact mode.	102
Fig. 46 Evolution of the measured ellipsometric angles (Ψ & Δ) in three different samples of GNPs (40 mg Au ³⁺). Measurements performed at room temperature at incident angle 60°. Samples prepared at increased spin-coating ERs as shown in the two spectra.....	103
Fig. 47 Comparison between the experimental SE data (squares) and the modeled (lines) achieved by the constructed model in three ERs. (a) 2000 rpm, (b) 5000 rpm and (c) 10000 rpm.	104
Fig. 48 Evolution of the film thickness as function of increased evaporation rates.	105
Fig. 49 Comparison between the dielectric function (ϵ_r and ϵ_i) of the three samples having increased ER that is determined using the model.	105
Fig. 50 The absorbance coefficient (α) spectra as a function of wavelength extracted by the model of the three samples that were performed at increased ERs.....	106
Fig. 51 SEM images of 40 mg gold precursor (NaAuCl ₄ /acetone/ethanol) showing GNCs at increased ERs: (a) 2000 rpm, (b) 5000 rpm and (c) 10000 rpm.	108
Fig. 52 Spectroscopic ellipsometric data (Ψ & Δ) of assemblies of GNCs attached to the PMMA film on silicon substrate at increased ERs. Measurements performed at room temperature at incident angle 60°.....	109
Fig. 53 Ellipsometric spectra of GNCs: squares spectra for measured (experimental) data and solid lines for the calculated (modeled). The incident angle is 60 °.	110
Fig. 54 Thickness plot (for PMMA film) as function of evaporation rate.	111
Fig. 55 Imaginary part (left) and Real part (right) dielectric function of monodispersed GNCs assembled in PMMA films.....	112

Fig. 56 Absorbance coefficient (α) plot of GNCs as a function of wavelength (nm) in increased ERs.	113
Fig. 57 SEM images showing various shapes of GNPs. (a) poly-dispersed GNHs and GNTs, (b) monodispersed GNCs, (c) poly-dispersed GNHs and (d) poly-dispersed GNCs and GNRs. (a) and (b) prepared with same PMMA solvent (acetone) and different Au precursor (a in HAuCl ₄ & b in NaAuCl ₄). (c) and (d) prepared at same PMMA solvent (MIBK) and different Au precursor (c in HAuCl ₄ & d in NaAuCl ₄). The four samples were prepared at the same standard spin-coating parameters and same solvent precursor (ethanol).	114
Fig. 58 Measured ellipsometric parameters of Ψ (left) and Δ (right) values for GNPs embedded in PMMA film on Si wafers prepared with different synthetic parameters. Samples prepared at same spin-coating conditions. Measurements performed at incident angle of 60°.	115
Fig. 59 Comparison between measured and calculated ellipsometric spectra for GNPs embedded in PMMA film over Si wafers prepared over various experimental conditions as shown in these spectra. Samples prepared at same spin-coating conditions and measurements performed at incident angle 60° as a function of the wavelength (λ).	116
Fig. 60 Evolution of the thickness of PMMA film in four different samples. Samples prepared at same spin-coating conditions.	117
Fig. 61 Dielectric function of ϵ_i (left) and ϵ_r (right) spectra for gold nanoparticles at different experimental conditions as shown in both spectra.	118
Fig. 62 UV-Vis absorption spectra of gold nanoparticles in four different samples prepared according to the experimental conditions displayed in the figure with their illustrated SEM images in the right side at scale bar of 200 nm. Samples prepared at same spin-coating parameters.	119
Fig. 63 Absorbance spectra showing the behavior of plasmon peak of monodispersed GNTs (blue spectrum), mono-dispersed GNHs (red spectrum) and poly-dispersed GNHs and GNTs (black spectrum). Samples prepared at same coating conditions and different gold precursors and PMMA solvents as presented in these spectra. The three insets (SEM images) correspond to various non-cubic shapes.	120
Fig. 64 SEM images of GNPs at large scan size. Samples (a) and (b) prepared with same gold precursor (HAuCl ₄), and different PMMA solvents: (a) MIBK and (b) acetone. Sample (c) differs from (b) by the gold precursor which is KAuCl ₄ . The three samples prepared at same coating conditions and with same gold precursor's solvent (isopropanol).	122
Fig. 65 Comparison between the measured and modeled ellipsometric spectra for GNPs of various shapes that correspond for samples which their SEM images are shown in Fig. 63 and Fig. 64. (a) Reflects poly-dispersed GNHs and GNTs, (b) presents the monodispersed GNHs and (c) contributes to monodispersed GNHs. Measurements are performed at incident angle 60°.	123
Fig. 66 Evolution of the thickness of PMMA film (nm) of the above three samples of GNPs. The insets show the various shapes of GNPs that can be obtained according to the presented experimental conditions.	124
Fig. 67 Evolution of the dielectric function of imaginary (ϵ_i) part of the above three samples of GNPs. Black spectrum refers to poly-dispersed GNHs and GNTs, red spectrum contributes to monodispersed GNHs and the blue spectrum presents the monodispersed GNTs.	125
Fig. 68 The absorbance spectra in (d), (e) and (f) represent the samples for which their SEM images are shown respectively in (a), (b) and (c). (a and d) Correspond to HAuCl ₄ precursor that results in the formation of poly-dispersed GNHs and GNTs in MIBK, (b and e) correspond to HAuCl ₄ precursor that forms monodispersed GNHs in acetone and (c, f) correspond to	

KAuCl ₄ precursor that yields to monodispersed GNTs in MIBK. The three samples were prepared by the same gold precursor's solvent (isopropanol) and in the same spin-coating parameters.	126
Fig. 69 The SEM images show the increase in the concentration of HAuCl ₄ precursor. (a) 10 mM, (b) 50 (mM) and (c) 100 mM. The samples prepared at the same spin-coating conditions.	135
Fig. 70 The SEM images show the increase in the speed of spin-coating for 50 mM HAuCl ₄ . Samples were prepared on Si-As substrates.....	136
Fig. 71 The SEM images show the influence of changing the substrate of 50 mM NaAuCl ₄ . Samples prepared at the same spin-coating conditions.....	137
Fig. 72 The SEM images show the influence of changing the substrate from Si-As to ITO in 60 mM of HAuCl ₄ and NAuCl ₄ precursors. The Samples prepared at same spin-coting conditions.	138
Fig. 73 AFM images of bimetallic system of Au and Ag NPs. (a) first layer of AuNps (40 mg of Au/Isopropanol-PMMA/MIBK), (b) Second layer of AgNPs (20 mg of Ag/Isopropanol-PMMA/MIBK) and (c) highlights two layers of Au-Ag NPs.....	138
Fig. 74 (a) AFM image of the first layer of AuNPs (20mg Au/ethanol-PMMA/MIBK), (b) bimetallic material of Au-Ag using 20mg of Ag/PVP and (c) bimetallic system of Au-Ag using 20 mg of Ag/Ethanol-PMMA/MIBK). The inset shows a bimetallic system of Au-Ag NPs that demonstrates a core-shell identity. Samples prepared at the same spin-coating parameters.	139
Fig. 75 AFM images of GNPs synthesized at different lots of PMMA. (a) 330,000 g/mol and (b) 120,000 g/mol. Samples prepared at the same spin-coating parameters on Si-As substrates using 100 mg of HAuCl ₄ precursor.....	139

List of tables

Table 1 Average diameter of gold nanoparticles obtained with different concentration of gold precursor.....	51
Table 2 Summary of the most known biological, chemical and physical methods used to synthesize metallic nanoparticles with different shapes. The table is adapted from ref. [10]..	74
Table 3 Combinations of the three solution components (solvent, non-solvent and precursor) for controlling the shape of GNPs.....	81

List of schemes

Scheme 1 Schematic representation of the fabrication method used in this chapter. It is observed that in the AFM image monodisperse gold nanocubes are approximately well dispersed on a silicon substrate.	46
Scheme 2 Schematic representation of the physical model used for ellipsometric data analysis.	54
Scheme 3 3D illustration of AFM image for gold nanocubes showing a strong adsorption of pyridine on their surface due to repulsive interaction forces with PMMA.....	63
Scheme 4 Combinations of the three solution components (solvent, non-solvent and precursor) in order to vary the growth rate through changing the volatility of solutions (effect of solvents) and pH (effect of precursor molecule type).....	89

List of abbreviations

AFM: Atomic Force Microscopy
As: Arsenic
AuNPs: Gold nanoparticles
BEM: Boundary elementary method
BEMA: Bruggeman effective medium approximation
DF: Dark field
EMT: effective medium approximation theory (EMT)
ER: Evaporation rate
GNCs: Gold nanocubes
GNHs: Gold nanohexagons
GNPs: Gold nanoparticles
GNR: Gold nanorectangles
GNTs: Gold nanotriangles
HGNs: hexagonal Gold nanoparticles
MG: Maxell-Garnet
MNPs: Metallic nanoparticles
NPs: Nanoparticles
NIR: Near Infra-red Region
SE: Spectroscopic ellipsometer
Sec: Seconds
SEM: Scanning Electron Microscopy
SERS: Surface Enhancement Raman Scattering
SEF: SERS Enhancement Factor
Si: Silicon
SMG: Seed mediated growth
SPR: Surface Plasmon Resonance
UPD: Under polar deposition
VIPs: Vapor Induced Phase Separation

General Introduction

The work presented in this thesis shows in **chapter 1** an overview of nanotechnology strategies allowing shape control of metal nanoparticles, focusing on a novel synthesis method of single shape of gold nanoparticles (GNPs) in **chapter 2**, discussing the shape control of these GNPs in **chapter 3**, and exposing their optical properties in **chapter 4**.

Different synthesis and fabrication methods of nanomaterials for GNPs have been shown in **chapter 1**, including both “top-down” (physical synthesis) and “bottom-up” (chemical synthesis) approaches. Considerable developmental works have been performed on GNPs fabrication methods through these approaches, most rely on size, shape and stability control.

The synthesis of controlled shapes of metallic nanoparticles (MNPs) has attracted attention particularly in sensing and catalysis, which mainly depend on MNPs morphology and surface characteristics. [1] In this context, the most cited studies in the literature rely on the development of seed-mediated growth and electrochemical methods. In **chapter 2**, we introduced a new fabrication way for the synthesis of gold nanocubes (GNCs) upon a fast and one-step nanofabrication method based on PMMA self-assembly. Through this chapter, we studied the influence of parameters that lead to the formation of the GNCs. We also emphasize the possibility to control the size of GNCs. Then, these GNCs were accomplished for SERS substrates because they are highly sensitive for the detection of small amounts of organic molecules such as Pyridine.

The shape is one of the most important factors in determining the structural, physical, and chemical properties of a nanoparticle. [2] For this aim, **Chapter 3** presents a modern way in shape-controlled nanomaterials through tuning the mechanism kinetic rate without the usage of any surfactant or reducing agent. It is known that the formation of different shapes is generally achieved by changing the reducing and the stabilizing agents upon colloidal synthesis. In parallel, many studies have investigated the role of ligands in controlling the NP morphologies. Despite the progress in the colloidal synthesis, it is still difficult to achieve systematic and predictive tuning of the NP morphologies because of the limited fundamental understanding of the formation of NP morphologies and the mechanistic roles of the used molecules especially the ligands. [3] Using our method that was described in chapter 2, we aimed to show the evolution of the cubic shape into another morphologies (such as gold nanohexagons (GNHs), gold nanoprisms and gold nanorectangles (GNRs)) by changing the major process components. The classical effective medium theories, used to exploit ellipsometric data consider only the spheroidal NPs. [4] In **chapter 4**, gold nanoparticles (GNPs) are optically characterized by

Spectroscopic Ellipsometry (SE) and compared to a theoretical modeling in order to understand the optical responses of their corresponding samples. We have presented a simple model which is based on two classical Lorentz oscillators (one for PMMA and another for GNPs) that generates quantitatively accurate results (optical constants). This model involves the primary measurement of the ellipsometric angles (Ψ and Δ) followed by a correct fitting of these angles. **Chapter 5** highlights the main conclusions derived from the previous four chapters and focuses on future perspectives of this work.

References

- [1] Scholl, J. A., Koh, A. L., & Dionne, J. A. (2012). Quantum plasmon resonances of individual metallic nanoparticles. *Nature*, 483(7390), 421-429.
- [2] Wang, Z. L. (1998). Structural analysis of self-assembling nanocrystal superlattices. *Advanced Materials*, 10(1), 13-30.
- [3] Nikoobakht, B., & El-Sayed, M. A. (2001). Evidence for bilayer assembly of cationic surfactants on the surface of gold nanorods. *Langmuir*, 17(20), 6368-6374.
- [4] Battie, Y., Izquierdo-Lorenzo, I., Resano-Garcia, A., Naciri, A. E., Akil, S., Adam, P. M., & Jradi, S. (2016). How to determine the morphology of plasmonic nanocrystals without transmission electron microscopy?. *Journal of Nanoparticle Research*, 18(8), 2.

1 Bibliographic study

1.1 Introduction

Over the last few decades, the field of nanotechnology has exponentially expanded and has been incorporated into many areas of science, including biology, environmental science, and energy research. [1-5] With the rising of the development of the applications in nanotechnology, synthesis strategies for nanomaterials have also evolved to meet the technological demands. Among these nanomaterials, metal nanoparticles with well-defined surfaces have attracted significant attention in many research areas, owing to their extraordinary catalytic properties. [6] By means of versatile, colloidal synthetic approaches, a variety of shapes have been achieved so far, including not only simple shapes (sphere, cube, tetrahedron, octahedron, decahedron, and icosahedrons), but also 1- or 2-dimensional shapes (rod, wire, plate, disc, triangular- and hexagonal-plate, and more complicated bi-pyramid, tetrapods, and hyper-branched structures). Nanoparticles with high surface areas can provide more active sites to lower the activation energy of the catalytic reactions, and unique surface structures such as steps, kinks, and terraces to influence the reaction pathways leading to product selectivity. [7-11]

In the case of gold, the most attractive feature of shape is the appearance of a plasmon band in the near infrared (NIR). Such property is necessary in biomedical applications that require nanomaterials of low frequencies absorption to preserve the cells. Thus, the “water window” between 800 nm and 1300 nm could be beneficial for medicinal diagnostics and photothermal therapy “theranostics”. [12],[13] This NIR absorption is shape and medium dependent. [14] In particular with Au nanoshells, nanorods, hollow nanospheres, and nanocubes. This property has led to significant progress in disease diagnostics and therapy. [13] Thus, synthesis and shape control of GNPs has attracted interest because of the new properties that appeared for non-spherical GNPs. As an example, triangular or hexagonal plates have a potential interest due to their sharp edges. These edges may lead to high local electric field gradients under illumination making them attractive candidates for various applications including optical biosensing and surface-enhanced Raman spectroscopy (SERS). [6] Moreover, catalytic properties of small GNPs (<5 nm) on textured surfaces have been widely explored. [7]

Colloidal synthesis approaches allowed the fabrication of a wide variety of morphologies like rods, rectangles, hexagons, cubes, triangles, and star-like outlines to branched Au particles in high yields at room temperature. This is achieved using only single surfactant (CTAB) within

an aqueous solution through the most common seed-mediated growth method that will be discussed later. Even though the colloidal approaches are the most common ways to fabricate nanoparticles with controlled morphologies, broad processes were explored until now. On this basis, the present chapter gives an overview of the most used bottom-up and top-down approaches that produce metallic nanoparticles with different shapes. Herein, we summarize the recent advances in nanotechnologies allowed shape control of the metallic nanoparticles including gold ones.

1.2 General shape-controlled synthesis strategies of metallic nanoparticles

1.2.1 Top-down synthesis

Top-down approach corresponds to the usage of nanofabrication tools that can be controlled by external experimental parameters to create nanostructures or functional devices with the specific shapes and characteristics, by reducing larger dimensions into the required values. [15], [16] Top-down strategies begin with a bulk gold substrate (mainly film or pellet), followed by a nanoscale patterning procedure through which the major part of the gold film is removed, thus producing GNPs with fixed scale and shape. [17] Electron-beam lithographic (EBL) method is the most commonly utilized top-down technique that leads to the formation of various shaped nanostructures with nanometer length scale. [18] In addition, the laser-based ablation [19] is one of the popular top down techniques. While the bottom-up approach constructs nanomaterials from basic building blocks like atoms or molecules, the top-down approach yields in nanostructures by breaking larger materials with the use of lithographic tools (i.e. physical top-down) or through chemical-based processes (i.e. chemical top-down).

1.2.1.1 Physical top-down synthesis

1.2.1.1.1 Optical lithography or photolithography

This technique which was known as the workhorse of the semiconductor industry for high volume manufacturing [20], has been also used to fabricate discrete monodisperse colloidal particles [21],[22]. The optical lithography, which was first discovered in the 1960's, is one of the most applicable physical top-down methods that can be used in fine scale patterning of integrated circuits [15],[16]. It requires an ultra violet light (UV) which can be collimated through a quartz plate in order to create patterns on a surface. [15],[21] Thus, the light can transfer the desired pattern from the quartz plate that serves as a mask into an organic light-

sensitive material called photoresist which can be coated on semiconductor substrates or wafers. [23],[24] Then, the pattern can be transferred into the underlying substrate just by etching. Resolution is enhanced through the usage of projection lens systems between the mask and substrate in order to image the mask onto the surface of the photoresist. [15] When the photoresist is exposed to light, it may form two possible transformations. First, the exposed regions will show a higher solubility in the formed solutions if a positive photoresist material is illuminated followed by the removal of the exposed photoresist from the solution. In addition, negative photoresist material will be cross-linked when exposed to light so they present a high solubility in the developing solution. However, after the interaction with the developing solution, areas that were deprived from the exposition to light will be etched away. The remaining photoresist patterns serve as a protector for the substrate from being removed. When the desired process is completed and the pattern is designed on the substrate, photoresist can be removed. [15] Both Mason [21] and Stroock [25] have reported using this type of approach; the possibility to generate highly monodisperse, shape-specific colloidal particles. This type of processing is characterized by the excellent formation of submicrometer level and by high throughput. [26]

1.2.1.1.2 Electron beam lithography

Electrons can be used instead of photons in a very known process called electron beam lithography (EBL) [27],[28] in order to create nanometer ranged features (smaller than 10 nm) and to overcome the diffraction limit of light, knowing that photolithography is limited by the diffraction limit in the size resolution of features (around 60 nm) and it is based on the wavelength of available lasers [3]. E-beam lithography was developed for manufacturing integrated circuits and leads to the formation of low-dimensional structures in the resist that will be transferred into the substrate material just by etching. Moreover, it is a mask-less form of lithography and very known in photomask-making for photolithography [27] where the pattern can be generated directly using a focused beam of accelerated electrons through 2D scanning over the substrate (surface of the material) that has been coated with any type of electron-reactive resist. Therefore, this is a relatively low throughput process. In comparison to photolithography, it has rather low productivity because it is a serial process and often a manual one. Even though, both techniques are only able to create a 2-dimensional structure in a single step. [3] It is the most common lithography technique to generate metallic nanostructures (GNPs) [29],[30] and allows the precise control of the size, shape and the spatial distribution of the formed nanoparticles [31]. The synthesis of GNPs could be achieved by EBL through

coating a substrate (eg. glass slide) with an electron-sensitive resist such as polymethyl methacrylate (PMMA). The electron beam dissociates such coated substrate into fragments, which can be selectively removed with a chemical developing agent. The remained nanoscale structure is suitable for the deposition of gold in the formed pattern by thermal evaporation. The unexposed PMMA film with the gold film deposited over it will be removed by acetone, thus keeping the desired gold nanoparticle arrays on the glass slide [30] as shown in Fig. 1. In fact, top-down electron beam lithography (EBL) is the most accurate experimental approach for achieving high level of control, but it suffers from some disadvantages. The required physical vapor deposition of metals can form non-crystalline structures, which is known to introduce imperfections that can increase the plasmon resonance linewidth by means of non-elastic scattering. However, EBL is not a realistic technique for the production of nanoparticle assemblies of controlled geometry, due to its high cost, relatively low speed and the limited transfer rate to design data. [32]

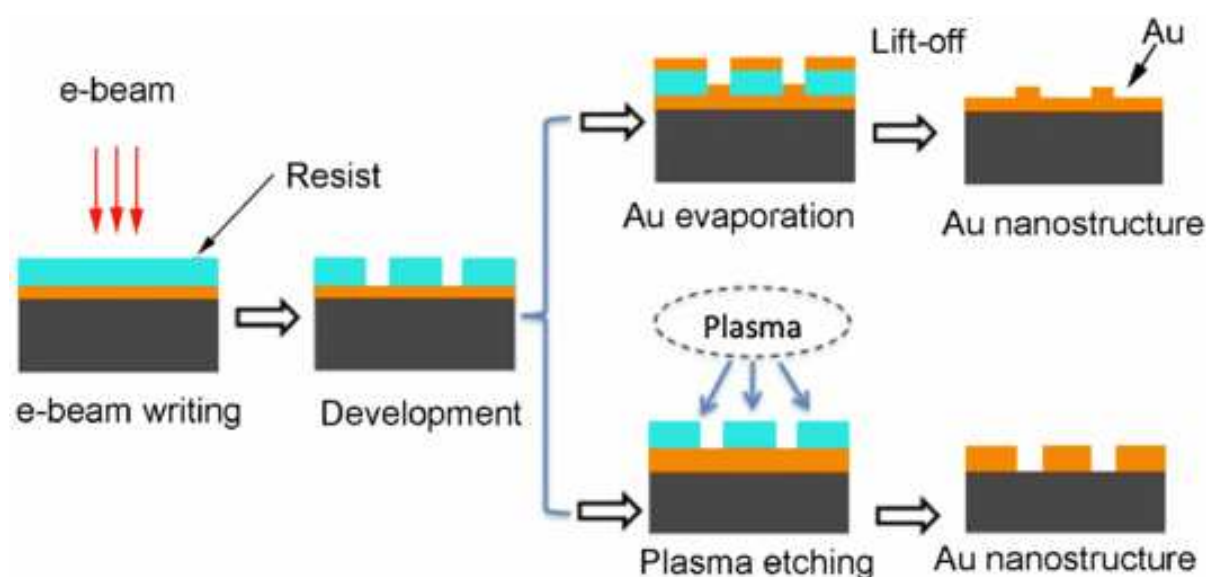


Fig. 1 Schematic illustration for the fabrication method of GNPs using EBL. Adapted from ref. [33]

1.2.1.2 Chemical top-down synthesis

Physical top-down approach has achieved great success in nanoscale fabrication. However, great efforts were made in developing new methods for chemical top-down nanofabrication. While physical top-down nanofabrication has shown the capability to produce nanoscale patterns on substrates in vacuum, chemical top-down approach has offered advantages in crafting nanostructures in solids as well as in solutions. Chemical routes to top-down nanofabrication have been attracting scientific interests in recent years due to their low cost and facile use that allow them to be used in various applications, such as sensing, biomedicine and catalysis. Unlike physical top-down techniques, the chemical based routes do not require tightly

controlled environments (cleanroom) and they are characterized by their synthetic versatility, ability to generate nanoporous material and variety of three-dimensional (3D) nanostructures features, wide applicability, suitable for manipulation, and great potential for large-scale production [28]. All these properties offer the chemical route a great success in nanostructure fabrication. Templated etching, anisotropic dissolution, and thermal decomposition are the major chemical routes [34-40]. While templated etching utilizes a template that serves as an etching mask to guide the formation of nanoscale features on a substrate, thermal decomposition involves heat treatment to transform the maternal inorganic solid into 3D nanoporous structures of controlled porosity with a simple one-step fabrication way. Selective dealloying forms a nanoporous metal from a metallic alloy [41] using chemicals to remove the most reactive metal constituent found within the alloy. Finally, anisotropic dissolution generates nanostructures with well-defined morphologies through selective dissolution of certain crystallographic facets. Such chemical top-down nanofabrication routes are less expensive than the physical ones, so they could be applied in large-scale device fabrication. Basically we will focus on template etching.

1.2.1.2.1 Template etching route

This method results in a nanoscale pattern which has been crafted on the surface of the substrate after subsequent removal of the template. Using a template such as block copolymer micelles, it is possible to fabricate well-defined 3 D etch pit array on silicon substrate (see Fig. 2) [28], [34]. The template can be obtained through spin-coating, by which amphiphilic polymer micelles are assembled on the substrate surface. The nanoscale pattern of the polymer template is then transferred to the underlying substrate via a selective etching agent (such as an aqueous solution of hydrofluoric acid that results in selective localization of fluoride ions within the micellar cores). The silicon etch pit array can be obtained after the removal of the polymer template through ultra-sonication in a solvent (toluene). The formed etched features on the silicon surface can be later functionalized into gold nanoparticles, leading to the generation of more complex architectures. [42] It was reported in literature that the templated etching could successfully produce long-range ordered arrays of nanoscale features on silicon substrates, which can allow the nanofabrication approach to form non-lithographic nanopatterning over silicon surfaces. Thus, templated etching technique could provide low-cost ways to fabricate large-area nanoscale patterns similarly to lithographic techniques. On the other hand, selective deploying, anisotropic dissolution and thermal decomposition have made it possible to construct different nanostructures having higher structural complexity. Such complex

nanoscale architectures can be useful for many disciplines beyond the microelectronics applications, such as catalysis [43], energy-related technologies [44],[45] and environmental monitoring [46].

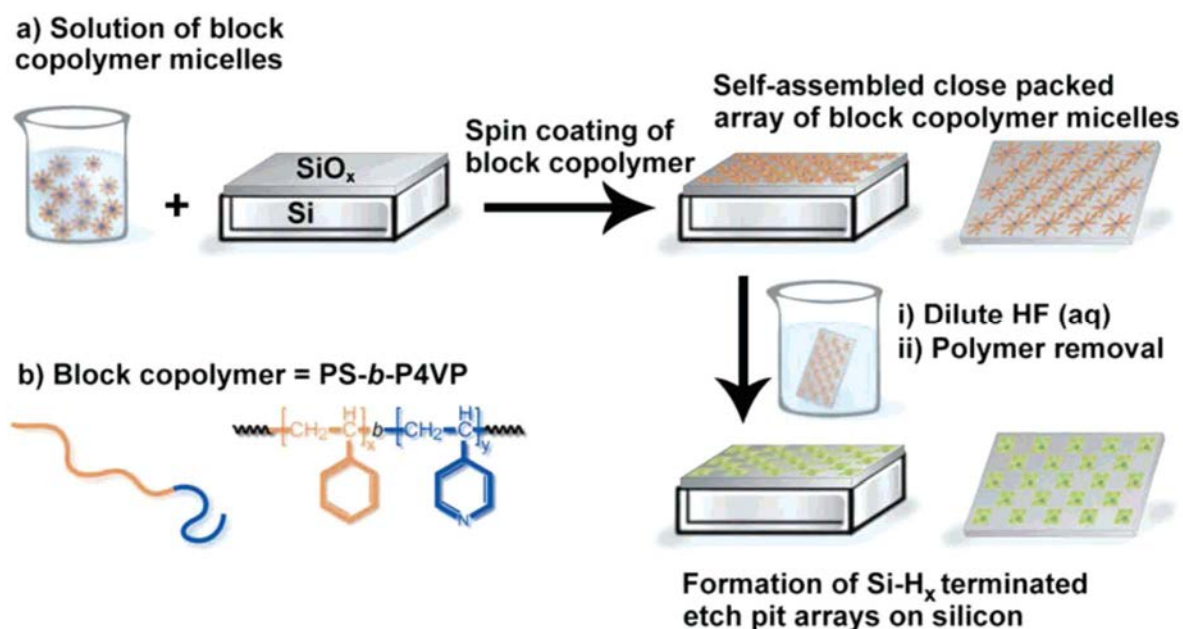


Fig. 2 Schematic representation for the fabrication of 3D etch pit array on silicon substrate through the usage of a block copolymer as template and an aqueous solution of Hydrofluoric acid (HF) as etchant. Adapted from ref. [34]

1.2.1.3 Deposition methods

1.2.1.3.1 Chemical and physical vapor deposition

Physical vapor deposition (PVD) and Chemical vapor deposition (CVD) techniques combine the research of nanomaterial synthesis. Such deposition methods provide an opportunity of the nanofabrication of highly complex nanostructures that are impossible to be obtained using other nanofabrication techniques. CVD is one of the most common processes that deposit thin films of many different materials [47]. It is widely used in microelectronics production because it generates uniform, conformal, and continuous films upon metal deposition. Nevertheless, it is possible to synthesize specific shapes of gold metal nanocrystals by CVD. In this approach, the deposition substrate plays an important role in determining the initial structure of deposited features. However, precursor ligand systems or highly Lewis basic coordinating ligands which can stabilize metal centers by increasing the thermal stability of the compounds, can be also used in vapor deposition techniques. Coordinative ligands such as N-heterocyclic carbenes (NHCs) [48],[49] are similar to the chemical surfactants and capping agents that are used in wet synthesis of metal nanocrystals. These precursors have a significant role in directing the growth during CVD by slowing growth on certain gold facets after dissociation. New advances in CVD

such as initiated chemical vapor deposition (CVD) give a possibility for the deposition of polymers without reducing the molecular weights during the CVD process. [27] Unlike CVD, in PVD method, materials are evaporated through an electron beam, plasma, or laser. [27] The evaporation material is vaporized with a supplied energy followed by the solidification of the surface of the substrate. Moreover, PVD processes are usually carried out in high vacuum environment which exclude the vapor towards the substrate without interacting with any other gaseous atoms in the reaction chamber. However, Biswas et al presented an advancement in PVD using a versatile e-beam-assisted co-deposition technique which has been developed to fabricate multicomponent nanomaterials. [50] Both deposition methods possess versatile nanofabrication tools for fabrication of nanomaterials (nanocomposites). Moreover, they are characterized by controlled deposition of several materials including metal, semiconductors, insulators and polymers. Furthermore, it is possible to deposit porous nanofilms using these methods. In contrast, these methods are highly expensive because of the expensive vacuum component in PVD and high temperature process in the case of CVD. Actually, shape control in chemical vapor deposition (CVD) has not been well explored, and metallic gold films are typically limited to nanoparticles or thin film morphologies. [51]

1.2.1.3.2 Atomic layer deposition

Atomic layer deposition (ALD) technique was first developed by Suntola and Antson. [52] It is currently used for surface engineering of high complex nanomaterials. This method is characterized by various advantages including; ability to control the thickness of the deposited layer which helps new approaches to modify the physico-chemical surface properties of the nanosized materials and it provides many opportunities for the new synthesis of new nanostructures and devices [53],[54]. It is based on self-terminating surface reactions of gaseous precursors that produces extremely thin, high-quality, and conformal films with controlled thickness at atomic level by depositing one atomic layer. ALD can generate Materials with 1D characteristics by complete filling of the porous holes of such materials with different aspect ratios. Furthermore, this approach can be used for a variety of materials, such as metals, semiconductors, or oxides, in order to produce 1D structures that exhibits excellent conformity and gap-filling abilities. [55] This method produces pin-hole free nanostructured films over large areas and it is a reproducible method with good adhesion due to the formation of chemical bonds at the first atomic layer. However, it is a slow process, an expensive one due to the usage of vacuum components as in PVD methods , and it is not suitable for certain metals. [27]

1.2.2 Bottom-up pathways

Bottom-up approaches construct multifunctional nanostructural materials and devices by directed self-assembly of molecular or atomic components [56] without generating waste or the need to eliminate the parts of the final system. Bottom-up nanofabrication often uses deposition techniques (atomic layer deposition & vapor phase deposition) and assembly processes (Chemical self-assembly, molecular or colloidal self-assembly, etc...), bottom-up nanosphere lithography, chemical, photochemical, electrochemical, templating, sonochemical and thermal reduction techniques [27],[57-60]. Bottom-up approaches have received great attention in biomedical applications (such as imaging, gene or drug delivery) through fabricating organic particles [26]. In addition, bottom up synthesis techniques involve an agent to stop the growth of the particle at the nanoscale [61], where capping materials, such as a surfactant or polymer can be used in this technique to prevent aggregation and precipitation of the metal nanoparticles out of solution. Some of the more commonly used bottom up techniques and those chemical methods that involve “bottom up” method for making GNPs are discussed below. Bottom-up approaches are readily scalable, but can lack fine control of the particle size and dispersity, and can be limited in the variety of shapes which produced.

1.2.2.1 Colloidal synthetic strategies

1.2.2.1.1 Seed mediated method

Metal nanoparticles are well known for their promising future applications in the fields of electronics, photonics, biochemical sensing and imaging, etc. due to their unusual properties, especially the optical ones such as: strong plasmon band absorption, enhanced Rayleigh scattering, and surface enhanced Raman Scattering. As mentioned before, nanoparticles can be synthesized by different ways which are divided into two main categories: top-down and bottom-up methods. In general, the growth of metal nanoparticles passes through two successive steps: nucleation, followed by controllable growth of the existing nuclei. The fundamental factor that enables the growth of metal nanoparticles is the presence of the corresponding metal salt in addition to a reducing agent. In the normal conditions, spherical nanoparticles will be formed due to their lowest surface energy. [62] On the other hand, anisotropic nanoparticles are obtained by promoting the growth step in a particular direction using special additives referred to as: "capping agents". Accordingly, a special and popular technique based bottom up method: "seed-mediated growth method" is used for the synthesis

of metal nanoparticles. [63-68] In this technique, the added capping agents reduce the growth rate, guiding the growth of the nanoparticle into non-spherical geometries including nanorods, nanocubes, nanoprisms, nanostars, and nanohexagons. [69],[70] The size and the shape of the obtained particles are controlled by the reaction conditions as well as the variation of the type and the concentration of the reagents utilized. The most common methods for size control require capping agents [71-74] such as: surfactants, ligands, and polymers whose role is to reserve the growth in the nanometer pattern.

According to the prolonged research studies, the synthesis of GNPs by seed-mediated method has developed stage-wise by the different research groups. The seed mediated growth method should provide the possibility to exclude the nucleation step and to boost the growth step. In such situations, small nanoparticles are assembled and later used as seeds to prepare larger particles in the presence of metal salt and weak reducing agents [75-77]. The idea of a two-step seeding-growth method to prepare monodispersed gold nanoparticles, was progressed by Zsigmondy et al. [78] who reported the two-phase method which has been later named: "the seed-growth method" and used afterwards by Turkevich et al. [79]. To control the particle size in particle synthesis, a well-known tool can be applied which is the usage of a capping agent. [80],[81] The stabilizer can strongly cap the particle, inhibiting its growth and producing capped metal particles that act, in their turn, as electron transfer catalysts. [82] Natan et al. reused citrate and borohydride-reduced gold particles as seeds for preparing larger nanoparticles having diameters between 30 and 100 nm employing citrate as a growth reducing agent. [76] Later, they have improved the monodispersity of particles relative to those prepared in one-step reduction of Au^{3+} with citrate. [83] Moreover, Jana et al. [84] have found that the presence of a seed can lead to the formation of nanoparticle products even smaller than the seed itself, indicating that seeds promote nucleation; and this problem have been also observed by other workers [85],[86]. Thus, controlling the rate of reagent addition directly over the seed can influence the particle size and distribution. For instance, the slow addition of a diluted reducing agent solution hides additional nucleation, and leads to the formation of large particles of improved monodispersity with size ranged between 20 and 100 nm. To illustrate more, ascorbic acid reduced gold nanoparticles, being prepared by fast addition, showed a broad size distribution (22 ± 10 nm) in the absence of seeds. However, the presence of seeds can recover such monodispersity when growth defeats nucleation (20 ± 6 nm). El-Sayed et al. have suggested two explanations for the formation of faceted and rod-shaped particles. In the first, the growth rate varies at different planes of the particles. Secondly, particle growth competes with capping action of stabilizers (the ionic reagents in Jana's work). [87] 5 nm particles

produced from seeds of the same size were more spherical for faster addition of reducing agent, but faceted in case of slow addition of the reducing agent. Even though, the faster addition in the absence of seeds, or in the presence of relatively small amount of seeds, leads to the formation of rods and facets. This observation was coherent to that obtained in earlier works. [88] The nucleation step that was proposed by Jana's group increases as the reaction progress slows down, and terminates when dominated by the growth. From the kinetic evidence, Finke et al. [89] proposed continuous slow nucleation with fast autocatalytic growth for transition-metal nanocluster formation. The size distribution obtained by Natan group [83] was similar to this exploration. In reduction without seeds, these faceted particles are sometimes obtained for weak reducing agent where growth occurs over a long period [88]. Jana et al. (or Murphy et al.,2001) [84] reported two mechanistic steps in seed mediated method, where the presence of seed can lead to nanoparticle products smaller than the seed as mentioned above, suggesting that seeds promote nucleation. This approach was defined by an initial slow nucleation, followed by burst of nucleation mediated by seeds and growth. The two-step mechanism presented in Fig. 3 for solution-phase gold nanoparticle synthesis shows narrower size distribution in response to separation time between nucleation and growth.

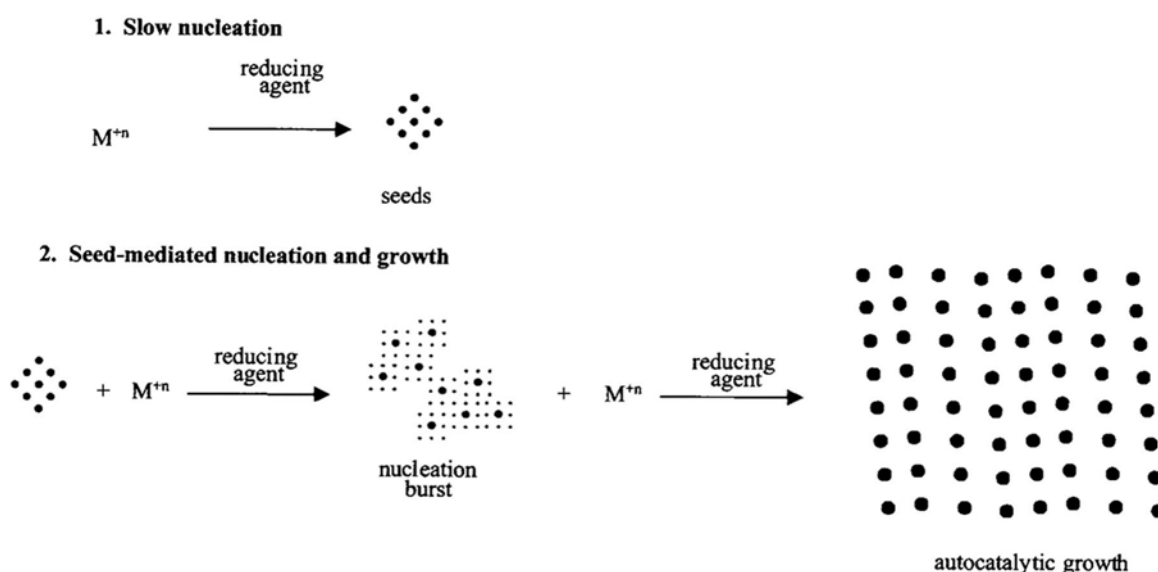


Fig. 3 Generalized two-step mechanism for solution-phase Au nanoparticle synthesis. [84]

Three-step seed-mediated growth method was used to make gold nanoparticles using different stabilizers like alkyltrimethylammonium bromides (C_n TAB). It was reported from this approach that the increase in the length of the surfactant chain results in increasing the gold nanoparticles aspect ratio [90]. Also, the maximal plasmon absorption for gold nanoparticles has varied with respect to change in shape. It was 520 nm for spheres, and reached 2000 nm for

high aspect ratio nanorods. Hence, the length of the surfactant tail is crucial for producing gold nanorods, where the increase in the length of the alkyl chain results in the production of higher-aspect ratio nanorods. The aspect ratio was 1 (for C₁₀TAB), 5 ± 2 (C₁₂TAB), 17 ± 3 (C₁₄TAB), and 23 ± 4 (C₁₆TAB) [90]. A relationship between the nanorod aspect ratio and the size of the seed was observed in literature [91] in a seed mediated synthesis of gold nanorods. In this study, it was shown that the aspect ratio of the nanorods increases with the decrease in the seed size under the usage of constant concentration of reagents. Then, the initial stage of the seeding step helps to determine the final nanorod size and shape formation. Not only the size, but also the charge on the seed plays an essential role in determining the nanorod aspect ratio. For instance, the variation in the aspect ratio of the positively charged seeds is not as pronounced as that of the negatively charged seeds. To clarify more, it was reported that the variation in parameters such as length, width, and aspect ratio of the gold nanorods (AuNRs) synthesized using different seeds follow a pattern as a function of seed size for negatively charged seeds. As the size of the seed increases, a reduction in the length as well as in the width of the final nanorods was observed, unlike the case of the positively charged seeds. Murphy's team [8] has developed the theory of the preferential binding of CTAB molecules assuming that (100) crystal face is the most preferable face in the nanorod synthesis and growth mechanism. That's why the introduction of a seed leads to rapid reduction of gold salt on the seed surface with competitive and preferential binding of CTAB molecules on the (100) surface. This stands to be the driving force of the generation of faceted spheres which then develop to form rods (see Fig. 4).

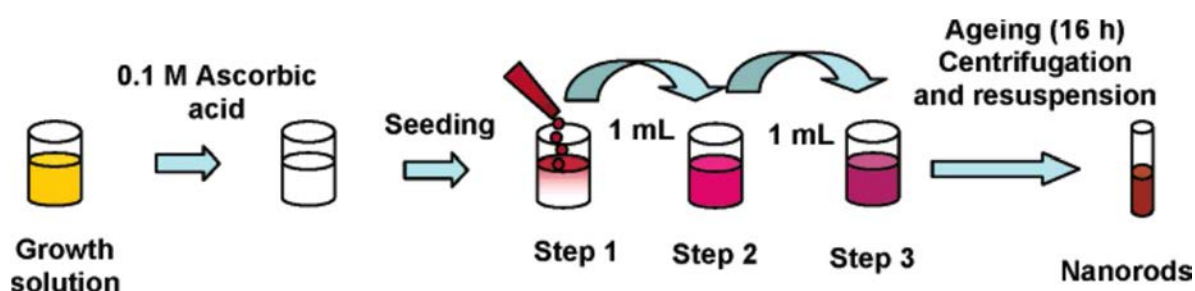


Fig. 4 Schematic representation for the generation of Gold Nanorods. [91]

Seed mediated growth allows shape control

In short, there is a general trend of the decrease in the gold nanorods' aspect ratio with an increase in the seed size, see Fig. 5. This clearly indicates that the seeds produced by (Nikoobakht and El-Sayed method) do not follow the general trend observed in this three-step seeding protocol. The main reason might be due to the doubt in determining the exact size of

the seed; which could be linked to the difficulty of removing excess CTAB molecules (by centrifugation). [91]

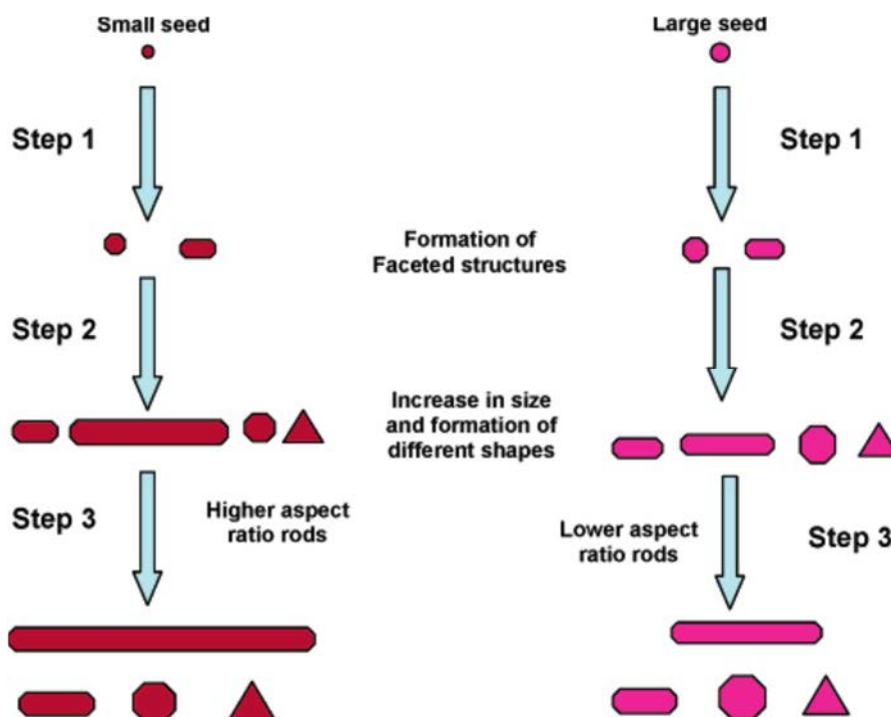


Fig. 5 Schematic illustration for different stages of growth of Gold Nanorods using small (5.5 nm) and large size (8 nm) seeds. [91]

It has been demonstrated that some alteration in the synthesis procedure such as increasing in the pH or the surfactant concentration, or adding extra halide ions can lead to the formation of planar nanostructures. Additionally, various structural architectures of Au particles can be produced in high yields at room temperature using only a single surfactant (CTAB) within an aqueous solution can be achieved using the most common seed mediated growth method. [92] Using this method, it is important to know that it involves the preparation of Au seed particles and the posterior addition of an appropriate quantity of the Au seed solution into an aqueous growth solution containing proper quantities of CTAB, HAuCl_4 , ascorbic acid (AA), and in some cases a small quantity of AgNO_3 . The final morphology and size of the Au nanoparticles depend on the concentrations of the seed particles and CTAB, in addition to the reactants (Au^{3+} and AA). All these factors were related to each other producing interesting combinations for various shapes. Other than chemical reagents, many natural reducing agents have been displayed to stimulate the formation of non-spherical morphologies. One of the most notable examples of biologically prepared gold nanoparticles is gold triangular nanoplates which were grown in the extract of living plants. For example, gold nanoplates were obtained in yield of 50% through the usage of extract of boiled lemongrass leaves which serve as both reducing and shape directing agent. [93] It has been also stated that sugars (aldoses) and aldehydes/ketones

act as interesting compounds for nanoparticle formation, knowing that modification in the concentration of lemongrass extract in solution could alter the average edge length of the prisms (100 to 1800 nm). [94]

1.2.2.2 Electrochemical synthesis

The electrochemical method has become an efficient and unique method to synthesize noble metal nanoparticles with diverse high-index facets. By comparison with common solution-phase methods, the electrochemical method can control the nucleation and growth thermodynamics as well as the kinetics of the metal nanoparticles through the externally applied potentials. [95] The electrochemical method to produce GNPs was first reported by Svedberg in 1921 [96] and then developed by Wang and co-workers who reported the formation of AuNRs through an electrochemical synthesis of metal clusters in reversed micelles in an organic solvent. The synthesis of AuNRs is conducted within two-electrodes, Au plate anode and a Pt plate cathode were immersed in an electrolyte containing CTAB and tetradodecylammonium bromide (TOAB) as a co-surfactant and small amounts of acetone and cyclohexane were also added into the electrolytic solution before the electrolysis. Acetone was used for untying the micellar framework, while cyclohexane was used to enhance the formation of elongated rod-like CTAB micelles. [97] During electrolysis, the bulk gold metal anode undergoes oxidation to form AuBr_4^- , which forms a complex with the CTAB and migrates towards the cathode, where the cathodic reduction into Au^0 occurs. Moreover, the aspect ratio of the formed AuNRs was controlled by gradually immersing a silver plate in a position behind the platinum cathode where a redox reaction between Au III and Ag plate takes place. The ultrasonification was used to disperse the AuNRs and keep them away from the cathode during the electrolysis. [97],[98] This method produces AuNRs with aspect ratios of 3-7 that are single crystals. [99] The electrochemical method is one of the pioneering methods for the synthesis of anisotropic GNPs; it is a simple, efficient and highly applicable technique. [100],[101]

1.2.3 Self-assembly

Self-assembly fabrication methods involve manipulating particle-particle or particle-scaffold interactions to enhance the assembly of the nanoscale building blocks into certain ordered structures so that molecular self-assembly can be achieved. The intrinsic feature of self-assembly is characterized by the spontaneous organization of building blocks into a relatively stable structure at a thermodynamic equilibrium state that corresponds to the minimum Gibbs

free energy [102]. In particular, fabrication methods using different self-assembly techniques is now possible [103] but it seems that much of these approaches cannot be easily extrapolated for producing assemblies of controlled geometries with particles of high aspect ratio. That's why, such assemblies were integrated to a variety of materials and techniques including surface modification [104],[105], templates [106], and polymer-mediated assembly of gold NPs including assembly using linear block copolymers, functional polymers [107],[108] as well as recent studies using biopolymers such as proteins [109-111] and DNA [112-114] and they were also subjected to external fields [115],[116]. From these assemblies, spherical nanoparticles [117], as well as anisotropic nanorods [118] can be obtained. Non-directed or molecular self-assembly methods are simple, but they are limited in morphologies and sensitive to the experimental parameters including the concentration of the solution. Therefore, we describe here the self-assembly methods that allow shape control of metallic nanoparticles.

1.2.3.1.1 Polymer mediated self-assembly

Currently, self-assembly of NPs in a well-ordered 2D arrays presents an important target in microelectronics providing a wide access to components of high density memory devices and integrated circuits. Nanoparticle assembly can be achieved through the usage of polymers as ligand or matrix. The polymer scaffold in metal-polymer composites play an important role in the assembly of NPs into composite material. It acts as a matrix by inducing ordering and anisotropic orientation on surfaces and processes an electronic property. Polymer composites that can be produced through a chemical approach oblige polymers to serve any or all of these functions [109]. For this target, Layer-by-layer (LbL) assembly is a simple technique for the fabrication of structural and functional thin films on substrates, where Crespo-Biel et al. developed many patterning strategies to generate polymer assembled NP films on cyclodextrin (CD)-functionalized self-assembled monolayers (SAMs) through host-guest (CD-adamantyl (Ad)) interactions [119]. The integration of GNPs into thin films is particularly important for various applications including, biosensors, and electronic optical nano-devices [109]. On the same basis, the use of prefabricated templates or a co-assembling polymer matrix can give rise to controlled orientation and distribution, but it requires the potentially difficult fabrication for template and the need for controlling of the orientation of the co-assembling polymer [114]. Recently, multifunctional nanostructures are fabricated in a fast, simple, parallel and flexible manner via self-assembly of building blocks of copolymers knowing that block copolymers are particularly interesting due to their ability to self-assemble into thermodynamically highly stable microphase-separated domains with precisely controlled size and shapes. In fact,

Nanofabrication via self-assembly of block copolymer templated inorganic nanomaterials such as gold or silver precursors allows the fabrication of multifunctional nanostructures with significantly enhanced mechanical, optical, electronic and magnetic properties. In this respect, 0D nanostructure in its spherical morphology (copolymer micelle) can be fabricated [120] in diblock copolymer system, polystyrene-*b*-polyvinyl pyridine (PS-*b*-P4VP) where particle (Au) loaded PS-*b*-P4VP micelles form in selective solvent for the PS block. To illustrate, these micelles can form spontaneously in block copolymer solutions due to the presence of a selective solvent to one of the two blocks and sufficiently high polymer concentration. Herein, PS and P4VP of amphiphilic block copolymers are incompatible with each other, so that the solvent should be good to one of these blocks and prevent the solubility of the other. Therefore, spherical aggregates of core-shell micelle will be generated according to the length of the blocks and the nature of the solvent (Fig. 6). Basically, the micelle morphology stabilizes the nanoparticles in solution and provides simple ways of tuning their diameter and distance when deposited over a solid substrate. Thereby, monolayers of particle-loaded micelles are interesting candidates for many applications including catalysis, surface modification and optical coatings. [120]

In fact, the morphology of block copolymer aggregates in solution relies on three factors: the repulsive interaction between coronal chains (e.g. Ps shell chains), the degree of stretching of the core-forming chains (P4VP) and the interfacial tension at the core-corona interface [121], [122]. When a polar co-solvent is added to the block copolymer solution, it swells selectively the micelle's core (P4VP), which can switch the spherical morphologies of the micelles into a variety of 1D nanostructures (rods, rings) as seen in Fig. 6.

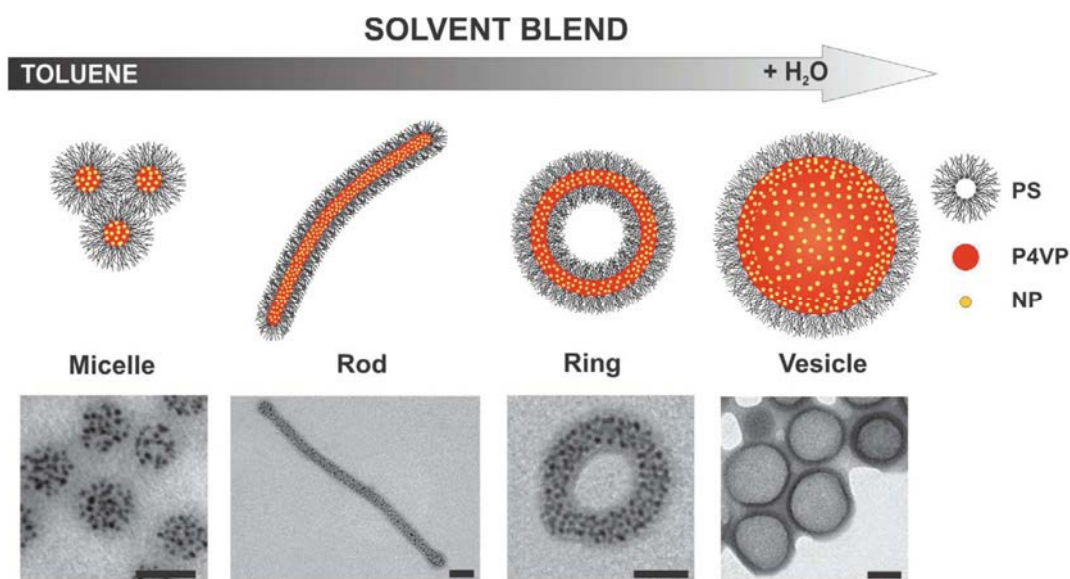


Fig. 6 Schematic representation of particle-loaded PS-b-P4VP micelles formed in a selective solvent (Toluene) for the PS block through controlling the morphology of the micelle upon addition of co-solvent (H₂O). [120]

An interesting challenge in nanotechnology is to tune the surface properties of thin films by controlling the lateral nanostructure of the functional hybrid materials and this was reported simply by spin-coating of solutions of the PS-b-P4VP hybrid material onto solid substrates [123], [124]. Actually, block copolymer vesicles loaded with inorganic nanoparticles that were fabricated via addition of the co-solvent (H₂O) can be used again as building blocks to fabricate 2D nanostructures in thin film. In such a way, the vesicles are spin-coated onto solid substrates to form porous thin film structures, where the pore size is determined by the vesicle diameter, followed by the extraction of the block copolymer matrix through oxygen plasma etching, generating purely inorganic nanostructures, which replicate the original film morphology (see Fig. 7). Moreover, these films significantly affect the surface properties, such as the wetting behavior of the coated substrate knowing that the original solid substrate (SiO₂) is moderately hydrophilic (water contact angle WCA = 38°) and these films show strongly hydrophobic surface properties with contact angles up to 115°. Plasma etching decreases hydrophobicity properties of the surface through decreasing the contact angle (WCA = 89°). The surface properties are highly dependent on the size of the film structures as well as on the film thickness [125]. Top down lithographic techniques are successful for nanostructuring materials ranging 100 nm to several micrometers [125]. Hence, for applications with scales smaller than 50 nm, lithographic methods are not convenient and they are expensive methods. On this respect, many methods were investigated to fabricate 3D nanostructures, that incorporate the inorganic particle into the block co-polymer system without well control over the size and shape [126], [127]. This is due to the fact that the reduction of the inorganic precursors takes place in a

solvent that can swell or dissolve one or both of the blocks of the polymer. Later, this method has been expanded into a successful approach by Wiesner and co-workers [128] in bulk that takes advantage of a coordination process that begins in solution. The generation of the nanoparticles starts by a selective coordination of an inorganic precursor (a metallic salt), specifically to one functional block of a diblock copolymer in solution. Through the evaporation of the solvent, the BCP (block-copolymer) directs the self-assembly process, by which the functional block carries the precursor to its own nanodomains, separating it from the non-functionalized domains. After the solvent evaporation, the system is no more mobile and the microphase separated morphology is fixed [129]. Actually, the inorganic precursor (Au-precursor) is reduced to the form of nanoparticles, and the growth begins while nanoparticles are still confined to the functional block (for example P4VP) of the block-copolymer (PS-b-P4VP). This block acts as a nanoreactor or nucleation center that controls the growth of GNPs with respect to size and size distribution. Add to that, block copolymers can control the spatial arrangement of the inorganic components (Au precursor) into 3D structures of different morphologies just by altering the volume fraction of one of the blocks. Therefore, self-assembly of the block copolymer can be tuned by changing the molecular weight, volume fraction or solution conditions, so that well-defined nanostructured hybrid materials, suitable to wide range of nanotechnology applications, can be fabricated. While great progress has been made in terms of controlling the morphologies and the physical properties of GNPs assembly, it is necessary to understand clearly the fundamental principles of self-assembly. In particular, self-assembly approach using amphiphilic diblock copolymers as templates is one of the most used approaches in the field of fabrication of MNPs, although it requires many purification steps to obtain pure MNPs that are strongly bound to the substrate. Because self-assembly products are very low, combined techniques are required. [103]

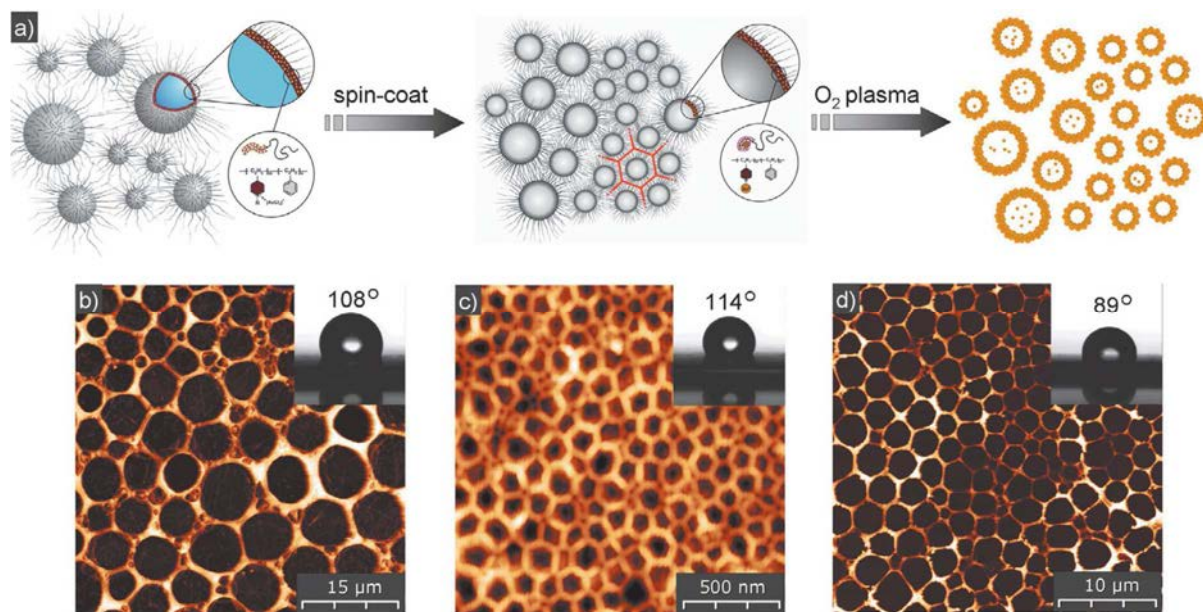


Fig. 7 Vesicles loaded with metal nanoparticles are prepared in solution and regular honeycomb structures are fabricated via spin-coating. Nanostructured thin films of the inorganic material are obtained after oxygen plasma etching. Depending on the diameter of the vesicles large (b) or small (c) honeycomb patterns can be fabricated. The structure is preserved during O_2 plasma etching (d). The insets in b-d are optical photographs of water droplets on top of the films indicating hydrophobic surface properties. Adapted from ref [120].

1.2.3.1.2 DNA mediated assembly

Structural DNA nanotechnology [130] and in particular DNA origami [131] has emerged as a versatile ‘bottom-up’ approach for the assembly of two and three-dimensional nanostructures with tailored geometries [132],[133]. Such structures were assembled by folding a long ‘scaffold’ strand of viral single-stranded DNA (ssDNA). This technique has been used in a variety of applications including, molecular transport in cells [134],[135], drug delivery systems [136] and biosensors [137]. Moreover, sequence programmability, selective molecular recognition ability and the relative rigidity of the double-helical structure of DNA [138] & [109], provide a platform for DNA to direct the assembly of NPs into ordered nanomaterials [139],[140]. On the same basis, it was reported that a DNA origami design allows a reliable assembly of 40 nm Au NP dimer structures with strong plasmonic coupling that obeys the characteristic polarization-dependent response of strongly coupled NPs and has a significant influence on the dimer plasmonic properties [110]. Furthermore, DNA hybridization [141],[142] is an approach which can assemble GNPs with controlled spatial arrangement of two or more distinct GNPs. Today, DNA has emerged as an interesting ligand for controlling NP morphologies because it can program them with information that directs their self-assembly [143-146] towards a prescribed structure or yield desired behavior. However, DNA-mediated NP assembly can generate DNA-Au NP assemblies through a strong electrostatic interaction between cationic NPs and anionic DNA that is aligned along the DNA scaffold. Murray and

Wang have controlled the assembly of GNPs having cationic trimethyl (mercaptoundecyl) ammonium monolayers with anionic DNA [147], so that one-dimensional water-soluble chains with spacing between NPs, which can be determined through monolayer thickness, can be produced. These highly organized chains of metal NPs have potential applications as soluble conductive nanowires. DNA-grafted particles can be prepared via several synthesis routes. At the nanoscale level, DNA oligonucleotides are often attached to gold nanoparticles through a thiol functional group [148],[149]. Regardless the synthetic method, the particles attract one another via the formation of DNA bridges. These bridges can be formed when a DNA strand is grafted to one particle and can directly hybridize a strand being grafted to a second particle [150],[151] , or when the two grafted strands hybridize with a third strand called a linker [152],[153]. By changing the NP to DNA ratio, network structures could be formed. However, highly ordered linear structure assemblies of GNPs along stretched DNA molecules on substrates can be generated too [154],[155] (see Fig. 8).

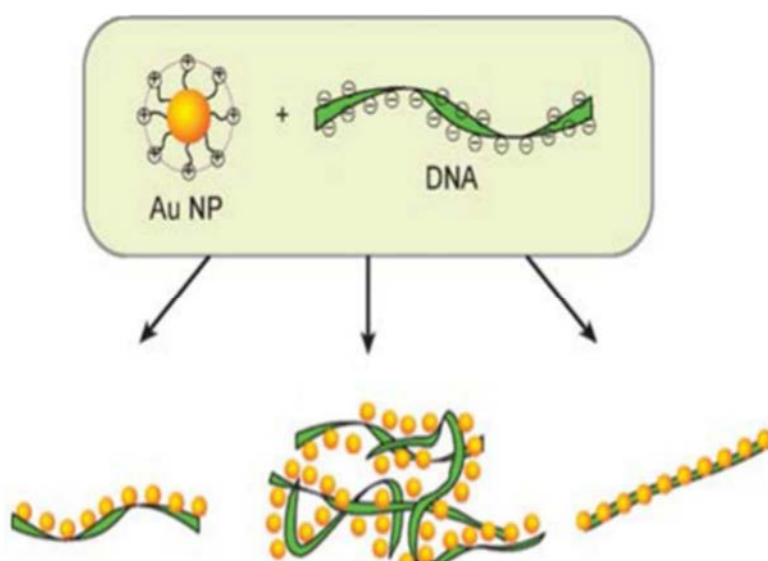


Fig. 8 Schematic illustration for DNA hybridization (interaction between cationic NPs and anionic DNA). [154], [155]

Recently, it was reported the DNA-mediated growth system, which is a perfect system to study the growth mechanism of Au nanoprism seeds into variety of shapes. [156] In this study, the interactions between the DNA and nanomaterials allowed the control of shapes and surface properties of many nanomaterials. (see Fig. 9)

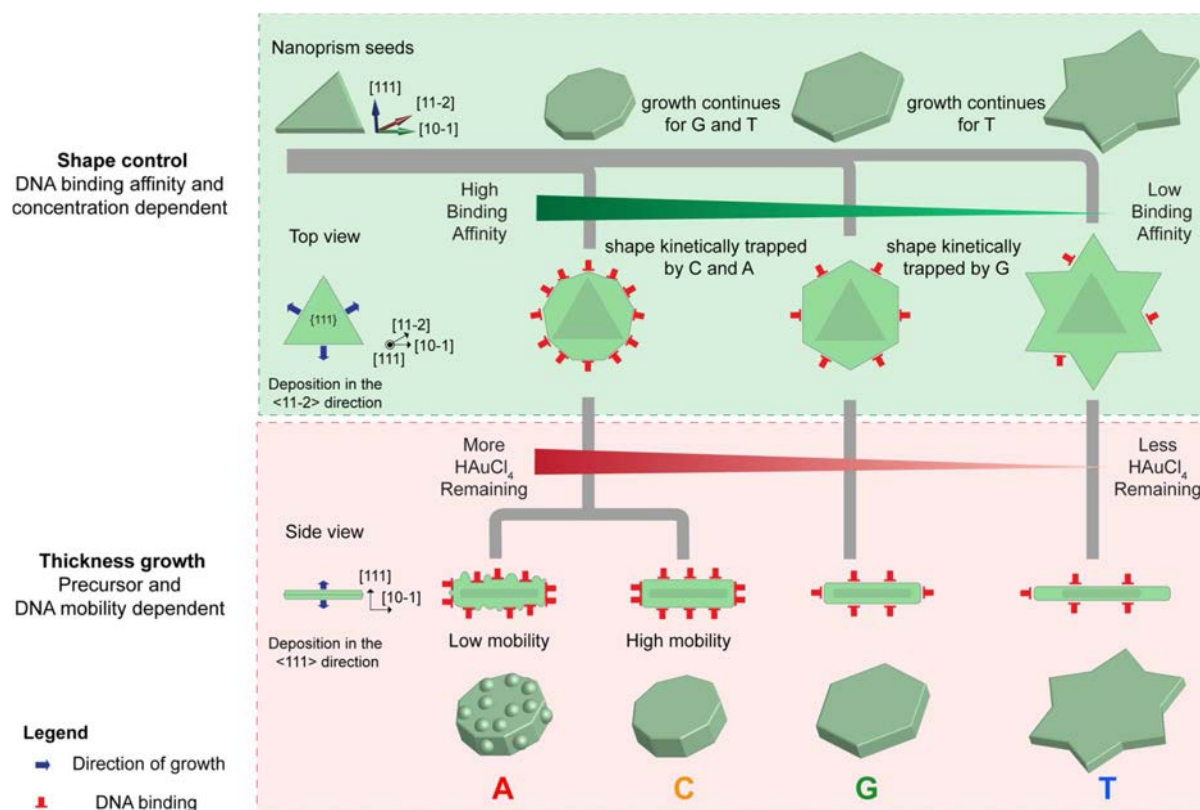


Fig. 9 Schematic representation of DNA mediated growth mechanism of Au Nanoprisms into different shapes in two Stages: Shape control followed by thickness growth. [156]

1.2.3.1.3 Protein mediated assembly

Among different biological molecules, the peptide is one of the most attractive materials because of its wide advantages including; tunable chemical properties, specification by adjusting primary amino acid sequence, chelation with various inorganic ions, reducing property and in particular the ability to self-assemble to form complex structures that results in the formation of different morphologies. Moreover, they are biocompatible and biodegradable and the nanobio-conjugate materials are highly used in medical applications such as drug delivery. [157] The synthesis method is based on two-step processes; first, the self-assembly of the peptide to form the templates, followed by the synthesis of nanoparticles. The peptide acts as a reducing agent to guide the nucleation and the growth of the GNPs and the size of the hybrid sphere structures can be easily tuned with temperature. It was explored that the assembly of the spheres was dependent on the primary amino acid sequence of the peptide and it was affected by the amino acids that contain aromatic functional groups. Kim et al. demonstrated the self-assembling ability of peptides as templates to be used in assembly of GNPs by *in situ* reaction. [158] In addition, engineered interaction between proteins and monolayer-protected NPs can be utilized to generate highly organized assemblies with structural diversity. These superstructures combine tunable NP features with the unique physical and chemical properties

of the proteins providing a way to form a wide array of materials and devices [109]. Mann and co-workers have investigated antibody-antigen recognition to self-assemble GNPs into macroscopic materials [159]. Streptavidin-biotin binding has been widely used for protein-substrate NP assembly due to its high stability and specificity [160],[161]. Biotinylated GNPs were engineered to assemble with the tetrameric protein streptavidin [162], by which the interaction of streptavidin with the GNPs can lead to the aggregation of the NPs (see Fig. 10). This was evidenced by a shift in the surface plasmon resonance peak, a broadening of the absorption spectrum, and the aggregates of NPs can reversibly switch into non aggregated state just by the addition of soluble biotin.

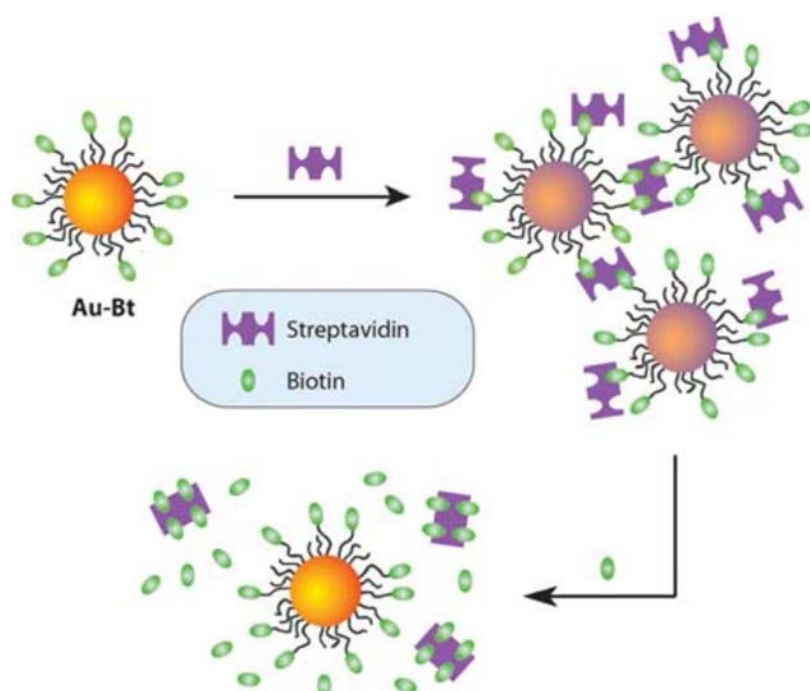


Fig. 10 Schematic representation of interactions of biotinylated GNPs with streptavidin: assembly and disassembly. [109]

1.3 Conclusion

According to the state of art about the usage of nanotechnologies to fabricate shape-controlled metallic nanoparticles, which was done in this chapter, it can be concluded that there is no general mechanism responsible for the formation of anisotropic nanostructures. It appears that particular issues for each reaction environment need to be considered. Moreover, the role of each reaction parameter in the formation of such nanostructure is not yet fully understood and it has been proposed that the final shape of a nanoparticle depends on the different factors operating synergistically. It seems that colloidal approaches are the most common ways investigated in the fabrication of non-spherical nanoparticles mainly due to their simplicity, low cost and high yield production. A common finding in many studies about colloidal synthesis is

the important role of surfactants and capping agent molecules as directing agents for achieving anisotropic growth. However, as discussed in this chapter, important considerations regarding the nucleation kinetics as well as the formation of twin planes that favor anisotropic structures should also be taken into account. Twins are readily formed during the nucleation of colloidal noble-metal nanocrystals. Hence, strategies to control the kinetics and the formation of particular nuclei should provide better ways for rational strategies to produce anisotropic noble metal nanocrystals. It should be pointed out that, in some cases, the surfactant stabilization seems to have a more important role. This question was, for us, a key question proposed in many studies. From there, we tried to develop substrate-strategy synthesis allowing to fabricate monodisperse gold nanoparticles with different shapes. To make it possible, the nanocrystals will be stabilized on the substrate surface and their kinetically growth will be directed, no surfactant is used (i.e. no stabilization of this one is necessary here). The synthesis approach that was used in this work is polymer self-assembly-based method and it will be described in details in the next chapter.

1.4 References

- [1] Feynman, R. P. (1960). There's plenty of room at the bottom. *Engineering and science*, 23(5), 22-36.
- [2] Huang, X., Jain, P. K., El-Sayed, I. H., & El-Sayed, M. A. (2007). Gold nanoparticles: interesting optical properties and recent applications in cancer diagnostics and therapy. *Nanomedicine*, 2(5), 681-693.
- [3] Eustis, S., & El-Sayed, M. A. (2006). Why gold nanoparticles are more precious than pretty gold: noble metal surface plasmon resonance and its enhancement of the radiative and nonradiative properties of nanocrystals of different shapes. *Chemical society reviews*, 35(3), 209-217.
- [4] Brust, M., & Kiely, C. J. (2002). Some recent advances in nanostructure preparation from gold and silver particles: a short topical review. *Colloids and Surfaces A: Physicochemical and Engineering Aspects*, 202(2), 175-186.
- [5] Saha, K., Agasti, S. S., Kim, C., Li, X., & Rotello, V. M. (2012). Gold nanoparticles in chemical and biological sensing. *Chemical reviews*, 112(5), 2739-2779.
- [6] Kelly, K. L., Coronado, E., Zhao, L. L., & Schatz, G. C. (2003). The optical properties of metal nanoparticles: the influence of size, shape, and dielectric environment. *J. Phys. Chem. B*, 107, 668-677.
- [7] Louis, C., & Pluchery, O. (2012). *Gold nanoparticles for physics, chemistry and biology*. World Scientific.171-173.
- [8] Johnson, C. J., Dujardin, E., Davis, S. A., Murphy, C. J., & Mann, S. (2002). Growth and form of gold nanorods prepared by seed-mediated, surfactant-directed synthesis. *Journal of Materials Chemistry*, 12(6), 1765-1770.

- [9] Manna, L., Milliron, D. J., Meisel, A., Scher, E. C., & Alivisatos, A. P. (2003). Controlled growth of tetrapod-branched inorganic nanocrystals. *Nature materials*, 2(6), 382-385.
- [10] Lee, S. M., Jun, Y. W., Cho, S. N., & Cheon, J. (2002). Single-crystalline star-shaped nanocrystals and their evolution: programming the geometry of nano-building blocks. *Journal of the American Chemical Society*, 124(38), 11244-11245.
- [11] Yacamán, M. J., Ascencio, J. A., Liu, H. B., & Gardea-Torresdey, J. (2001). Structure shape and stability of nanometric sized particles. *Journal of Vacuum Science & Technology B: Microelectronics and Nanometer Structures Processing, Measurement, and Phenomena*, 19(4), 1091-1103.
- [12] Lal, S., Clare, S. E., & Halas, N. J. (2008). Nanoshell-enabled photothermal cancer therapy: impending clinical impact. *Accounts of chemical research*, 41(12), 1842-1851.
- [13] Murphy, C. J., Gole, A. M., Stone, J. W., Sisco, P. N., Alkilany, A. M., Goldsmith, E. C., & Baxter, S. C. (2008). Gold nanoparticles in biology: beyond toxicity to cellular imaging. *Accounts of chemical research*, 41(12), 1721-1730.
- [14] Li, N., Zhao, P., & Astruc, D. (2014). Anisotropic gold nanoparticles: synthesis, properties, applications, and toxicity. *Angewandte Chemie International Edition*, 53(7), 1756-1789.
- [15] Gates, B. D., Xu, Q., Stewart, M., Ryan, D., Willson, C. G., & Whitesides, G. M. (2005). New approaches to nanofabrication: molding, printing, and other techniques. *Chemical reviews*, 105(4), 1171-1196.
- [16] Ando, Y., Miyake, K., Mizuno, A., Korenaga, A., Nakano, M., & Mano, H. (2010). Fabrication of nanostripe surface structure by multilayer film deposition combined with micropatterning. *Nanotechnology*, 21(9), 095304.
- [17] Huang, X., Neretina, S., & El-Sayed, M. A. (2009). Gold nanorods: from synthesis and properties to biological and biomedical applications. *Advanced Materials*, 21(48), 4880-4910.
- [18] Hu, M., Ou, F. S., Wu, W., Naumov, I., Li, X., Bratkovsky, A. M., ... & Li, Z. (2010). Gold nanofingers for molecule trapping and detection. *Journal of the American Chemical Society*, 132(37), 12820-12822.
- [19] Huang, W., Qian, W., & El-Sayed, M. A. (2006). Gold nanoparticles propulsion from surface fueled by absorption of femtosecond laser pulse at their surface plasmon resonance. *Journal of the American Chemical Society*, 128(41), 13330-13331.
- [20] Geissler, M., & Xia, Y. (2004). Patterning: principles and some new developments. *Advanced Materials*, 16(15), 1249-1269.
- [21] Hernandez, Carlos J., and Thomas G. Mason. "Colloidal alphabet soup: Monodisperse dispersions of shape-designed lithoparticles." *The Journal of Physical Chemistry C* 111.12 (2007): 4477-4480.
- [22] Jang, J. H., Ullal, C. K., Kooi, S. E., Koh, C., & Thomas, E. L. (2007). Shape control of multivalent 3D colloidal particles via interference lithography. *Nano letters*, 7(3), 647-651.
- [23] Ito, T., & Okazaki, S. (2000). Pushing the limits of lithography. *Nature*, 406(6799), 1027-1031.

- [24] Maily, D. (2009). Nanofabrication techniques. *the European Physical Journal-Special Topics*, 172(1), 333-342.
- [25] Badaire, S., Cottin-Bizonne, C., Woody, J. W., Yang, A., & Stroock, A. D. (2007). Shape selectivity in the assembly of lithographically designed colloidal particles. *Journal of the American Chemical Society*, 129(1), 40-41.
- [26] Merkel, T. J., Herlihy, K. P., Nunes, J., Orgel, R. M., Rolland, J. P., & DeSimone, J. M. (2009). Scalable, shape-specific, top-down fabrication methods for the synthesis of engineered colloidal particles. *Langmuir*, 26(16), 13086-13096.
- [27] Biswas, A., Bayer, I. S., Biris, A. S., Wang, T., Dervishi, E., & Faupel, F. (2012). Advances in top-down and bottom-up surface nanofabrication: Techniques, applications & future prospects. *Advances in colloid and interface science*, 170(1), 2-27.
- [28] Yu, H. D., Regulacio, M. D., Ye, E., & Han, M. Y. (2013). Chemical routes to top-down nanofabrication. *Chemical Society Reviews*, 42(14), 6006-6018.
- [29] Billot, L., de La Chapelle, M. L., Grimault, A. S., Vial, A., Barchiesi, D., Bijeon, J. L., ... & Royer, P. (2006). Surface enhanced Raman scattering on gold nanowire arrays: evidence of strong multipolar surface plasmon resonance enhancement. *Chemical physics letters*, 422(4), 303-307.
- [30] Smythe, E. J., Cubukcu, E., & Capasso, F. (2007). Optical properties of surface plasmon resonances of coupled metallic nanorods. *Optics Express*, 15(12), 7439-7447.
- [31] Boltasseva, A. (2009). Plasmonic components fabrication via nanoimprint. *Journal of Optics A: Pure and Applied Optics*, 11(11), 114001.
- [32] Broers, A. N. (1995). Fabrication limits of electron beam lithography and of UV, X-ray and ion-beam lithographies. *Philosophical Transactions of the Royal Society of London A: Mathematical, Physical and Engineering Sciences*, 353(1703), 291-311.
- [33] Petryayeva, E., & Krull, U. J. (2011). Localized surface plasmon resonance: nanostructures, bioassays and biosensing—a review. *Analytica chimica acta*, 706(1), 8-24.
- [34] Qiao, Y., Wang, D., & Buriak, J. M. (2007). Block copolymer templated etching on silicon. *Nano letters*, 7(2), 464-469.
- [35] Zacharatos, F., Gianneta, V., & Nassiopoulou, A. G. (2008). Highly ordered hexagonally arranged nanostructures on silicon through a self-assembled silicon-integrated porous anodic alumina masking layer. *Nanotechnology*, 19(49), 495306.
- [36] Zhang, Z., Wang, Y., Qi, Z., Zhang, W., Qin, J., & Frenzel, J. (2009). Generalized fabrication of nanoporous metals (Au, Pd, Pt, Ag, and Cu) through chemical dealloying. *The Journal of Physical Chemistry C*, 113(29), 12629-12636.
- [37] Erlebacher, J. (2004). An atomistic description of dealloying porosity evolution, the critical potential, and rate-limiting behavior. *Journal of the Electrochemical Society*, 151(10), C614-C626.
- [38] Yu, H. D., Yang, D., Wang, D., & Han, M. Y. (2010). Top-Down Fabrication of Calcite Nanoshoot Arrays by Crystal Dissolution. *Advanced Materials*, 22(29), 3181-3184.
- [39] Mulvihill, M. J., Ling, X. Y., Henzie, J., & Yang, P. (2009). Anisotropic etching of silver nanoparticles for plasmonic structures capable of single-particle SERS. *Journal of the American Chemical Society*, 132(1), 268-274.

- [40] Yu, H. D., Tee, S. Y., & Han, M. Y. (2013). Preparation of porosity-controlled calcium carbonate by thermal decomposition of volume content-variable calcium carboxylate derivatives. *Chemical Communications*, 49(39), 4229-4231.
- [41] Shang, Y., Sun, D., Shao, Y., Zhang, D., Guo, L., & Yang, S. (2012). A Facile Top-Down Etching To Create a Cu₂O Jagged Polyhedron Covered with Numerous {110} Edges and {111} Corners with Enhanced Photocatalytic Activity. *Chemistry-A European Journal*, 18(45), 14261-14266.
- [42] Zhang, X., Qiao, Y., Xu, L., & Buriak, J. M. (2011). Constructing metal-based structures on nanopatterned etched silicon. *ACS nano*, 5(6), 5015-5024.
- [43] Xu, C., Su, J., Xu, X., Liu, P., Zhao, H., Tian, F., & Ding, Y. (2007). Low temperature CO oxidation over unsupported nanoporous gold. *Journal of the American Chemical Society*, 129(1), 42-43.
- [44] Lou, X. W., Deng, D., Lee, J. Y., & Archer, L. A. (2008). Thermal formation of mesoporous single-crystal Co₃O₄ nano-needles and their lithium storage properties. *Journal of Materials Chemistry*, 18(37), 4397-4401.
- [45] Zeis, R., Mathur, A., Fritz, G., Lee, J., & Erlebacher, J. (2007). Platinum-plated nanoporous gold: An efficient, low Pt loading electrocatalyst for PEM fuel cells. *Journal of Power Sources*, 165(1), 65-72.
- [46] Guo, Z., Li, M., & Liu, J. (2008). Highly porous CdO nanowires: preparation based on hydroxy- and carbonate-containing cadmium compound precursor nanowires, gas sensing and optical properties. *Nanotechnology*, 19(24), 245611.
- [47] Hampden-Smith, M. J., & Kostas, T. T. (1995). Chemical vapor deposition of metals: Part 1. An overview of CVD processes. *Chemical Vapor Deposition*, 1(1), 8-23.
- [48] Zhukhovitskiy, A. V., Mavros, M. G., Van Voorhis, T., & Johnson, J. A. (2013). Addressable carbene anchors for gold surfaces. *Journal of the American Chemical Society*, 135(20), 7418-7421.
- [49] Ling, X., Roland, S., & Pileni, M. P. (2015). Supracrystals of N-Heterocyclic Carbene-Coated Au Nanocrystals. *Chemistry of Materials*, 27(2), 414-423.
- [50] Biswas, A., Eilers, H., Hidden Jr, F., Aktas, O. C., & Kiran, C. V. S. (2006). Large broadband visible to infrared plasmonic absorption from Ag nanoparticles with a fractal structure embedded in a Teflon AF® matrix. *Applied physics letters*, 88(1), 013103.
- [51] Griffiths, M. B., Koponen, S. E., Mandia, D. J., McLeod, J. F., Coyle, J. P., Sims, J. J., ... & Barry, S. T. (2015). Surfactant directed growth of gold metal nanoplates by chemical vapor deposition. *Chemistry of Materials*, 27(17), 6116-6124.
- [52] Niinistö, L., Nieminen, M., Päiväsaari, J., Niinistö, J., & Putkonen, M. (2004). Advanced electronic and optoelectronic materials by Atomic Layer Deposition: An overview with special emphasis on recent progress in processing of high-k dielectrics and other oxide materials. *physica status solidi (a)*, 201(7), 1443-1452.
- [53] Leskelä, M., Kemell, M., Kukli, K., Pore, V., Santala, E., Ritala, M., & Lu, J. (2007). Exploitation of atomic layer deposition for nanostructured materials. *Materials science and engineering: C*, 27(5), 1504-1508.
- [54] King, D. M., Johnson, S. I., Li, J., Du, X., Liang, X., & Weimer, A. W. (2009). Atomic layer deposition of quantum-confined ZnO nanostructures. *Nanotechnology*, 20(19), 195401.

- [55] George, S. M. (2009). Atomic layer deposition: an overview. *Chemical reviews*, 110(1), 111-131.
- [56] Ariga, K., Hill, J. P., Lee, M. V., Vinu, A., Charvet, R., & Acharya, S. (2008). Challenges and breakthroughs in recent research on self-assembly. *Science and Technology of Advanced Materials*, 9(1), 014109.
- [57] Gómez, D. E., Davis, T. J., & Funston, A. M. (2014). Plasmonics by design: design principles to structure–function relationships with assemblies of metal nanoparticles. *Journal of Materials Chemistry C*, 2(17), 3077-3087.
- [58] Okitsu, K., Ashokkumar, M., & Grieser, F. (2005). Sonochemical synthesis of gold nanoparticles: effects of ultrasound frequency. *The Journal of Physical Chemistry B*, 109(44), 20673-20675.
- [59] Hall, S. R., Shenton, W., Engelhardt, H., & Mann, S. (2001). Site-Specific Organization of Gold Nanoparticles by Biomolecular Templating. *ChemPhysChem*, 2(3), 184-186.
- [60] Magnusson, M. H., Deppert, K., Malm, J. O., Bovin, J. O., & Samuelson, L. (1999). Gold nanoparticles: production, reshaping, and thermal charging. *Journal of Nanoparticle Research*, 1(2), 243-251.
- [61] Kamat, P. V. (2002). Photophysical, photochemical and photocatalytic aspects of metal nanoparticles.
- [62] Hu, M., Chen, J., Li, Z. Y., Au, L., Hartland, G. V., Li, X., ... & Xia, Y. (2006). Gold nanostructures: engineering their plasmonic properties for biomedical applications. *Chemical Society Reviews*, 35(11), 1084-1094.
- [63] Stewart, M. E., Anderton, C. R., Thompson, L. B., Maria, J., Gray, S. K., Rogers, J. A., & Nuzzo, R. G. (2008). Nanostructured plasmonic sensors. *Chemical reviews*, 108(2), 494-521.
- [64] Burrows, N. D., Harvey, S., Idesis, F. A., & Murphy, C. J. (2017). Understanding the Seed-Mediated Growth of Gold Nanorods through a Fractional Factorial Design of Experiments. *Langmuir*, 33(8), 1891-1907.
- [65] Zhao, P., Li, N., & Astruc, D. (2013). State of the art in gold nanoparticle synthesis. *Coordination Chemistry Reviews*, 257(3), 638-665.
- [66] Jana, N. R., Gearheart, L., & Murphy, C. J. (2001). Wet chemical synthesis of high aspect ratio cylindrical gold nanorods. *The Journal of Physical Chemistry B*, 105(19), 4065-4067.
- [67] Jana, N. R., Gearheart, L., & Murphy, C. J. (2001). Seed-mediated growth approach for shape-controlled synthesis of spheroidal and rod-like gold nanoparticles using a surfactant template. *Advanced Materials*, 13(18), 1389.
- [68] Nikoobakht, B., & El-Sayed, M. A. (2003). Preparation and growth mechanism of gold nanorods (NRs) using seed-mediated growth method. *Chemistry of Materials*, 15(10), 1957-1962.
- [69] Zhou, Y., Wang, C. Y., Zhu, Y. R., & Chen, Z. Y. (1999). A novel ultraviolet irradiation technique for shape-controlled synthesis of gold nanoparticles at room temperature. *Chemistry of materials*, 11(9), 2310-2312.

- [70] Maye, M. M., Zheng, W., Leibowitz, F. L., Ly, N. K., & Zhong, C. J. (2000). Heating-induced evolution of thiolate-encapsulated gold nanoparticles: a strategy for size and shape manipulations. *Langmuir*, 16(2), 490-497.
- [71] Frens, G. (1973). Controlled nucleation for the regulation of the particle size in monodisperse gold suspensions. *Nature*, 241(105), 20-22.
- [72] Fendler, J. H., & Meldrum, F. C. (1995). The colloid chemical approach to nanostructured materials. *Advanced Materials*, 7(7), 607-632.
- [73] Zhao, M., Sun, L., & Crooks, R. M. (1998). Preparation of Cu nanoclusters within dendrimer templates. *Journal of the American Chemical Society*, 120(19), 4877-4878.
- [74] Teranishi, T., Hosoe, M., Tanaka, T., & Miyake, M. (1999). Size control of monodispersed Pt nanoparticles and their 2D organization by electrophoretic deposition. *The Journal of Physical Chemistry B*, 103(19), 3818-3827.
- [75] Henglein, A., & Meisel, D. (1998). Radiolytic control of the size of colloidal gold nanoparticles. *Langmuir*, 14(26), 7392-7396.
- [76] Brown, K. R., & Natan, M. J. (1998). Hydroxylamine seeding of colloidal Au nanoparticles in solution and on surfaces. *Langmuir*, 14(4), 726-728.
- [77] Sau, T. K., Pal, A., Jana, N. R., Wang, Z. L., & Pal, T. (2001). Size controlled synthesis of gold nanoparticles using photochemically prepared seed particles. *Journal of Nanoparticle Research*, 3(4), 257-261.
- [78] Sharma, V., Park, K., & Srinivasarao, M. (2009). Colloidal dispersion of gold nanorods: Historical background, optical properties, seed-mediated synthesis, shape separation and self-assembly. *Materials Science and Engineering: R: Reports*, 65(1), 1-38.
- [79] Turkevich, J., Stevenson, P. C., & Hillier, J. (1951). A study of the nucleation and growth processes in the synthesis of colloidal gold. *Discussions of the Faraday Society*, 11, 55-75.
- [80] Schmid, G., Bäuml, M., Geerkens, M., Heim, I., Osemann, C., & Sawitowski, T. (1999). Current and future applications of nanoclusters. *Chemical Society Reviews*, 28(3), 179-185.
- [81] Esumi, K., Suzuki, A., Yamahira, A., & Torigoe, K. (2000). Role of poly (amidoamine) dendrimers for preparing nanoparticles of gold, platinum, and silver. *Langmuir*, 16(6), 2604-2608.
- [82] Ung, T., Liz-Marzan, L. M., & Mulvaney, P. (1999). Redox catalysis using Ag@ SiO₂ colloids. *The Journal of Physical Chemistry B*, 103(32), 6770-6773.
- [83] Brown, K. R., Walter, D. G., & Natan, M. J. (2000). Seeding of colloidal Au nanoparticle solutions. 2. Improved control of particle size and shape. *Chemistry of Materials*, 12(2), 306-313.
- [84] Jana, N. R., Gearheart, L., & Murphy, C. J. (2001). Evidence for seed-mediated nucleation in the chemical reduction of gold salts to gold nanoparticles. *Chemistry of Materials*, 13(7), 2313-2322.
- [85] Watzky, M. A., & Finke, R. G. (1997). Nanocluster size-control and "Magic Number" investigations. experimental tests of the "Living-metal polymer" concept and of mechanism-based size-control predictions leading to the syntheses of iridium (0) nanoclus.

- [86] Wiesner, J., & Wokaun, A. (1989). Anisometric gold colloids. Preparation, characterization, and optical properties. *Chemical Physics Letters*, 157(6), 569-575.
- [87] Petroski, J. M., Wang, Z. L., Green, T. C., & El-Sayed, M. A. (1998). Kinetically controlled growth and shape formation mechanism of platinum nanoparticles. *The Journal of Physical Chemistry B*, 102(18), 3316-3320.
- [88] Goia, D. V., & Matijević, E. (1998). Preparation of monodispersed metal particles. *New Journal of Chemistry*, 22(11), 1203-1215.
- [89] Watzky, M. A., & Finke, R. G. (1997). Transition metal nanocluster formation kinetic and mechanistic studies. A new mechanism when hydrogen is the reductant: slow, continuous nucleation and fast autocatalytic surface growth. *Journal of the American Chemical Society*, 119(43), 10382-10400.
- [90] Gao, J., Bender, C. M., & Murphy, C. J. (2003). Dependence of the gold nanorod aspect ratio on the nature of the directing surfactant in aqueous solution. *Langmuir*, 19(21), 9065-9070.
- [91] Gole, A., & Murphy, C. J. (2004). Seed-mediated synthesis of gold nanorods: role of the size and nature of the seed. *Chemistry of Materials*, 16(19), 3633-3640.
- [92] Sau, T. K., & Murphy, C. J. (2004). Room temperature, high-yield synthesis of multiple shapes of gold nanoparticles in aqueous solution. *Journal of the American Chemical Society*, 126(28), 8648-8649.
- [93] Burda, C., Chen, X., Narayanan, R., & El-Sayed, M. A. (2005). Chemistry and properties of nanocrystals of different shapes. *Chemical reviews*, 105(4), 1025-1102.
- [94] Xie, J., Lee, J. Y., & Wang, D. I. (2007). Synthesis of single-crystalline gold nanoplates in aqueous solutions through biomineralization by serum albumin protein. *The Journal of Physical Chemistry C*, 111(28), 10226-10232.
- [95] Tian, N., Zhou, Z. Y., & Sun, S. G. (2008). Platinum metal catalysts of high-index surfaces: from single-crystal planes to electrochemically shape-controlled nanoparticles. *The Journal of Physical Chemistry C*, 112(50), 19801-19817.
- [96] Svedberg, T. (1921). The formation of colloids. J. & A. Churchill.
- [97] Chang, S. S., Shih, C. W., Chen, C. D., Lai, W. C., & Wang, C. C. (1999). The shape transition of gold nanorods. *Langmuir*, 15(3), 701-709.
- [98] Yu, Y. Y., Chang, S. S., Lee, C. L., & Wang, C. C. (1997). Gold nanorods: electrochemical synthesis and optical properties. *The Journal of Physical Chemistry B*, 101(34), 6661-6664.
- [99] Wang, Z. L., Gao, R. P., Nikoobakht, B., & El-Sayed, M. A. (2000). Surface reconstruction of the unstable {110} surface in gold nanorods. *The Journal of Physical Chemistry B*, 104(23), 5417-5420.
- [100] Ye, W., Yan, J., Ye, Q., & Zhou, F. (2010). Template-free and direct electrochemical deposition of hierarchical dendritic gold microstructures: growth and their multiple applications. *The Journal of Physical Chemistry C*, 114(37), 15617-15624.
- [101] Taleb, A., Mangeney, C., & Ivanova, V. (2011). Electrochemical synthesis using a self-assembled Au nanoparticle template of dendritic films with unusual wetting properties. *Nanotechnology*, 22(20), 205301.

- [102] Bishop, K. J., Wilmer, C. E., Soh, S., & Grzybowski, B. A. (2009). Nanoscale forces and their uses in self-assembly. *small*, 5(14), 1600-1630.
- [103] Barrow, S. J., Funston, A. M., Wei, X., & Mulvaney, P. (2013). DNA-directed self-assembly and optical properties of discrete 1D, 2D and 3D plasmonic structures. *Nano Today*, 8(2), 138-167.
- [104] Rycenga, M., McLellan, J. M., & Xia, Y. (2008). Controlling the assembly of silver nanocubes through selective functionalization of their faces. *Advanced Materials*, 20(12), 2416-2420.
- [105] Walker, D. A., & Gupta, V. K. (2008). Reversible end-to-end assembly of gold nanorods using a disulfide-modified polypeptide. *Nanotechnology*, 19(43), 435603.
- [106] Martin, C. R. (1996). Membrane-based synthesis of nanomaterials. *Chemistry of Materials*, 8(8), 1739-1746.
- [107] Fava, D., Nie, Z., Winnik, M. A., & Kumacheva, E. (2008). Evolution of Self-Assembled Structures of Polymer-Terminated Gold Nanorods in Selective Solvents. *Advanced Materials*, 20(22), 4318-4322.
- [108] Zhang, Z., Horsch, M. A., Lamm, M. H., & Glotzer, S. C. (2003). Tethered nano building blocks: Toward a conceptual framework for nanoparticle self-assembly. *Nano Letters*, 3(10), 1341-1346.
- [109] Ofir, Y., Samanta, B., & Rotello, V. M. (2008). Polymer and biopolymer mediated self-assembly of gold nanoparticles. *Chemical Society Reviews*, 37(9), 1814-1825.
- [110] Thacker, V. V., Herrmann, L. O., Sigle, D. O., Zhang, T., Liedl, T., Baumberg, J. J., & Keyser, U. F. (2014). DNA origami based assembly of gold nanoparticle dimers for surface-enhanced Raman scattering. *Nature communications*, 5, 3448.
- [111] Rogers, W. B., Shih, W. M., & Manoharan, V. N. (2016). Using DNA to program the self-assembly of colloidal nanoparticles and microparticles. *Nature Reviews Materials*, 1, 16008.
- [112] Shah, M., Badwaik, V., Kherde, Y., Waghvani, H. K., Modi, T., Aguilar, Z. P., ... & Lawrenz, M. B. (2014). Gold nanoparticles: various methods of synthesis and antibacterial applications. *Front. Biosci*, 19(1320), 10-2741.
- [113] Shah, M., Badwaik, V. D., & Dakshinamurthy, R. (2014). Biological applications of gold nanoparticles. *Journal of nanoscience and nanotechnology*, 14(1), 344-362.
- [114] Thorkelsson, K., Bai, P., & Xu, T. (2015). Self-assembly and applications of anisotropic nanomaterials: A review. *Nano Today*, 10(1), 48-66.
- [115] Murphy, C. J., & Orendorff, C. J. (2005). Alignment of gold nanorods in polymer composites and on polymer surfaces. *Advanced Materials*, 17(18), 2173-2177.
- [116] Wang, P., Zhang, L., Xia, Y., Tong, L., Xu, X., & Ying, Y. (2012). Polymer nanofibers embedded with aligned gold nanorods: a new platform for plasmonic studies and optical sensing. *Nano letters*, 12(6), 3145-3150.
- [117] Kao, J., Thorkelsson, K., Bai, P., Rancatore, B. J., & Xu, T. (2013). Toward functional nanocomposites: taking the best of nanoparticles, polymers, and small molecules. *Chemical Society Reviews*, 42(7), 2654-2678.
- [118] Hore, M. J., & Composto, R. J. (2013). Functional polymer nanocomposites enhanced by nanorods. *Macromolecules*, 47(3), 875-887.

- [119] Crespo-Biel, O., Dordi, B., Maury, P., Péter, M., Reinhoudt, D. N., & Huskens, J. (2006). Patterned, hybrid, multilayer nanostructures based on multivalent supramolecular interactions. *Chemistry of materials*, 18(10), 2545-2551.
- [120] Fahmi, A., Pietsch, T., Mendoza, C., & Cheval, N. (2009). Functional hybrid materials. *Materials Today*, 12(5), 44-50.
- [121] Förster, S., Zisenis, M., Wenz, E., & Antonietti, M. (1996). Micellization of strongly segregated block copolymers. *The Journal of chemical physics*, 104(24), 9956-9970.
- [122] Discher, D. E., & Eisenberg, A. (2002). Polymer vesicles. *Science*, 297(5583), 967-973.
- [123] Fahmi, A., Pietsch, T., & Gindy, N. (2007). Hierarchical Nanoporous Structures by Self-Assembled Hybrid Materials Based on Block Copolymers. *Macromolecular Rapid Communications*, 28(24), 2300-2305.
- [124] Pietsch, T., Gindy, N., & Fahmi, A. (2009). Nano- and micro-sized honeycomb patterns through hierarchical self-assembly of metal-loaded diblock copolymer vesicles. *Soft Matter*, 5(11), 2188-2197.
- [125] Guo, L. J. (2007). Nanoimprint lithography: methods and material requirements. *Advanced materials*, 19(4), 495-513.
- [126] Bockstaller, M. R., Mickiewicz, R. A., & Thomas, E. L. (2005). Block copolymer nanocomposites: perspectives for tailored functional materials. *Advanced Materials*, 17(11), 1331-1349.
- [127] Akasaka, S., Mori, H., Osaka, T., Mareau, V. H., & Hasegawa, H. (2009). Controlled introduction of metal nanoparticles into a microdomain structure. *Macromolecules*, 42(4), 1194-1202.
- [128] Simon, P. F., Ulrich, R., Spiess, H. W., & Wiesner, U. (2001). Block copolymer-ceramic hybrid materials from organically modified ceramic precursors. *Chemistry of Materials*, 13(10), 3464-3486.
- [129] Mendoza, C., Pietsch, T., Gutmann, J. S., Jehnichen, D., Gindy, N., & Fahmi, A. (2009). Block copolymers with gold nanoparticles: correlation between structural characteristics and mechanical properties. *Macromolecules*, 42(4), 1203-1211.
- [130] Seeman, N. C. (2010). Nanomaterials based on DNA. *Annual review of biochemistry*, 79, 65-87.
- [131] Rothmund, P. W. (2006). Folding DNA to create nanoscale shapes and patterns. *Nature*, 440(7082), 297-302.
- [132] Douglas, S. M., Dietz, H., Liedl, T., Högberg, B., Graf, F., & Shih, W. M. (2009). Self-assembly of DNA into nanoscale three-dimensional shapes. *Nature*, 459(7245), 414-418.
- [133] Dietz, H., Douglas, S. M., & Shih, W. M. (2009). Folding DNA into twisted and curved nanoscale shapes. *Science*, 325(5941), 725-730.
- [134] Douglas, S. M., Bachelet, I., & Church, G. M. (2012). A logic-gated nanorobot for targeted transport of molecular payloads. *Science*, 335(6070), 831-834.
- [135] Wickham, S. F., Bath, J., Katsuda, Y., Endo, M., Hidaka, K., Sugiyama, H., & Turberfield, A. J. (2012). A DNA-based molecular motor that can navigate a network of tracks. *Nature nanotechnology*, 7(3), 169-173.

- [136] Jiang, Q., Song, C., Nangreave, J., Liu, X., Lin, L., Qiu, D., ... & Ding, B. (2012). DNA origami as a carrier for circumvention of drug resistance. *Journal of the American Chemical Society*, 134(32), 13396-13403.
- [137] Burns, J. R., Göpfrich, K., Wood, J. W., Thacker, V. V., Stulz, E., Keyser, U. F., & Howorka, S. (2013). Lipid-Bilayer-Spanning DNA Nanopores with a Bifunctional Porphyrin Anchor. *Angewandte Chemie International Edition*, 52(46), 12069-12072.
- [138] Castro, C. E., Kilchherr, F., Kim, D. N., Shiao, E. L., Wauer, T., Wortmann, P., ... & Dietz, H. (2011). A primer to scaffolded DNA origami. *Nature methods*, 8(3), 221-229.
- [139] Ding, B., Deng, Z., Yan, H., Cabrini, S., Zuckermann, R. N., & Bokor, J. (2010). Gold nanoparticle self-similar chain structure organized by DNA origami. *Journal of the American Chemical Society*, 132(10), 3248-3249.
- [140] Bui, H., Onodera, C., Kidwell, C., Tan, Y., Graugnard, E., Kuang, W., ... & Hughes, W. L. (2010). Programmable periodicity of quantum dot arrays with DNA origami nanotubes. *Nano letters*, 10(9), 3367-3372.
- [141] Storhoff, J. J., Lazarides, A. A., Mucic, R. C., Mirkin, C. A., Letsinger, R. L., & Schatz, G. C. (2000). What controls the optical properties of DNA-linked gold nanoparticle assemblies?. *Journal of the American Chemical Society*, 122(19), 4640-4650.
- [142] Deng, Z., Tian, Y., Lee, S. H., Ribbe, A. E., & Mao, C. (2005). DNA-Encoded Self-Assembly of Gold Nanoparticles into One-Dimensional Arrays. *Angewandte Chemie*, 117(23), 3648-3651.
- [143] Sun, W., Boulais, E., Hakobyan, Y., Wang, W. L., Guan, A., Bathe, M., & Yin, P. (2014). Casting inorganic structures with DNA molds. *Science*, 346(6210), 1258361.
- [144] Berti, L., & Burley, G. A. (2008). Nucleic acid and nucleotide-mediated synthesis of inorganic nanoparticles. *Nature nanotechnology*, 3(2), 81-87.
- [145] Jones, M. R., Seeman, N. C., & Mirkin, C. A. (2015). Programmable materials and the nature of the DNA bond. *Science*, 347(6224), 1260901.
- [146] Tan, L. H., Xing, H., Chen, H., & Lu, Y. (2013). Facile and efficient preparation of anisotropic DNA-functionalized gold nanoparticles and their regioselective assembly. *Journal of the American Chemical Society*, 135(47), 17675-17678.
- [147] Wang, G., & Murray, R. W. (2004). Controlled assembly of monolayer-protected gold clusters by dissolved DNA. *Nano Letters*, 4(1), 95-101.
- [148] Mirkin, C. A., Letsinger, R. L., Mucic, R. C., & Storhoff, J. J. (1996). A DNA-based method for rationally assembling nanoparticles into macroscopic materials. *Nature*, 382(6592), 607-609.
- [149] Hurst, S. J., Lytton-Jean, A. K., & Mirkin, C. A. (2006). Maximizing DNA loading on a range of gold nanoparticle sizes. *Analytical chemistry*, 78(24), 8313-8318.
- [150] Valignat, M. P., Theodoly, O., Crocker, J. C., Russel, W. B., & Chaikin, P. M. (2005). Reversible self-assembly and directed assembly of DNA-linked micrometer-sized colloids. *Proceedings of the National Academy of Sciences of the United States of America*, 102(12), 4225-4229.
- [151] Nykypanchuk, D., Maye, M. M., Van Der Lelie, D., & Gang, O. (2008). DNA-guided crystallization of colloidal nanoparticles. *Nature*, 451(7178), 549-552.

- [152] Biancaniello, P. L., Kim, A. J., & Crocker, J. C. (2005). Colloidal interactions and self-assembly using DNA hybridization. *Physical Review Letters*, 94(5), 058302.
- [153] Xiong, H., van der Lelie, D., & Gang, O. (2008). DNA linker-mediated crystallization of nanocolloids. *Journal of the American Chemical Society*, 130(8), 2442-2443.
- [154] Ganguli, M., Babu, J. V., & Maiti, S. (2004). Complex formation between cationically modified gold nanoparticles and DNA: An atomic force microscopic study. *Langmuir*, 20(13), 5165-5170.
- [155] Nakao, H., Shiigi, H., Yamamoto, Y., Tokonami, S., Nagaoka, T., Sugiyama, S., & Ohtani, T. (2003). Highly ordered assemblies of Au nanoparticles organized on DNA. *Nano letters*, 3(10), 1391-1394.
- [156] Tan, L. H., Yue, Y., Satyavolu, N. S. R., Ali, A. S., Wang, Z., Wu, Y., & Lu, Y. (2015). Mechanistic insight into DNA-guided control of nanoparticle morphologies. *Journal of the American Chemical Society*, 137(45), 14456-14464.
- [157] Alex, S., & Tiwari, A. (2015). Functionalized gold nanoparticles: Synthesis, properties and applications—A review. *Journal of nanoscience and nanotechnology*, 15(3), 1869-1894.
- [158] Kim, J., Sadowsky, M. J., & Hur, H. G. (2011). Simultaneous synthesis of temperature-tunable peptide and gold nanoparticle hybrid spheres. *Biomacromolecules*, 12(7), 2518-2523.
- [159] Shenton, W., Davis, S. A., & Mann, S. (1999). Directed Self-Assembly of Nanoparticles into Macroscopic Materials Using Antibody–Antigen Recognition. *Advanced Materials*, 11(6), 449-452.
- [160] Li, H., Park, S. H., Reif, J. H., LaBean, T. H., & Yan, H. (2004). DNA-templated self-assembly of protein and nanoparticle linear arrays. *Journal of the American Chemical Society*, 126(2), 418-419.
- [161] Connolly, S., & Fitzmaurice, D. (1999). Programmed assembly of gold nanocrystals in aqueous solution. *Advanced Materials*, 11(14), 1202-1205.
- [162] Aslan, K., Luhrs, C. C., & Pérez-Luna, V. H. (2004). Controlled and reversible AstrucPhysical Chemistry B, 108(40), 15631-15639.

2 Shape-controlled synthesis of gold nanoparticles

2.1 Introduction

The shape-controlled synthesis of metallic nanoparticles (MNPs) has attracted attention particularly in sensing and catalysis, which mainly depend on MNPs morphology and surface characteristics. [1]

The investigation of metallic nanocubes, such as Ag nanocubes, [2] Pd nanocubes [3] and Au nanocubes [4], has been amplified during the last decade. In particular, gold nanocubes (GNCs) exhibit an interesting plasmonic features with their great potential applications in many fields such as biomedical drug delivery, biosensing, biomedical therapeutic applications, photohermal-therapy, and biochemical sensing. [5-13]

Therefore, considerable efforts have been devoted toward controlling the MNPs shape. In this context, the most cited studies in the literature rely on the development of seed-mediated growth and electrochemical methods. [14-16]

In this chapter, we describe our synthesis way of GNCs through a fast and one-step nanofabrication method based on PMMA self-assembly. First, we introduce the influence of the parameters that allowed us to obtain the cubic morphology. We also emphasize the possibility to control the size of GNCs. Then, a SERS study was performed on these GNCs to evaluate them as nanosensors. The pyridine molecule was used as a probe molecule mainly because of a wide number of SERS studies that nowadays don't allow to detect a low concentration of pyridine. Thus, we estimated the SERS enhancement factor and the detection threshold of bipyridine for the obtained substrates.

2.2 Synthesis method of gold nanocubes

GNCs can be synthesized using the most common fabrication process which is seed mediated growth (SMG) through which all the spherical crystalline seeds may grow into GNCs in solution at room temperature upon adjusting the experimental parameters such as the surfactant chain length, pH, metallic precursor concentration, etc. [17]

In addition to SMG, we cite here the most used methods of fabrication based on the relevant following works:

Skrabalak et al. have evolved Au nanocages and Au nanoframes from Ag nanocubes by a simple galvanic replacement reaction between solutions containing metal precursor salts and Ag nanostructures. [18] Huang et al. have also introduced the synthesis of uniform gold nanocubes

using an electrochemical method with cationic surfactant and the addition of acetone solvent. [4],[14]

Chiu et al. have reported the synthesis of gold nanocubes by seed mediated method to examine their comparative catalytic activity toward Sodium borohydride (NaBH_4) upon reducing of p-nitro aniline to p-phenylenediamine at variable temperatures. [15]

Jin et al. have used a thermal synthesis in which Au nanocolloids are converted into atomic Au cluster under high temperature reflux conditions, where these clusters serve as building blocks for the synthesis of Au Nanocubes. [16]

Sohn et al. launched a morphological engineering approach for NPs by constructing an evolutionary tree consisting of independent growth pathways of nanorods leading to the formation of square colloidal AuNPs by the enlargement of Au nanorods in all directions. [19]

Sun and Xia. have synthesized a large number of monodispersed silver nanocubes by reducing silver nitrate with ethylene glycol in the presence of polyvinyl pyrrolidone (pvp) where these Ag nanocubes can serve as template to generate single crystalline GNCs. [2]

Lin et al. have developed recently a new approach for the assembly of gold nanocubes onto order arrays via DNA Hybridization events onto a gold film substrates, using electron beam lithography, so that a strong coupling between plasmonic gap modes and a photonic lattice mode in two dimensional lattices can occur. [20]

Moreover, Zhang et al. manufactured monodispersed concave gold nanocubes by changing the counter ion of the surfactant in the seed-mediated synthetic method that is used by Murphy et al. before, where Cl^- counter ion in the surfactant plays an essential role in controlling the concave morphology of the final product of these gold nanocubes. [13],[17],[21]

Sun and Xia have reported the formation of Au-Ag nanoboxes with a combination of silver nanostructure (silver nanocubes) and aqueous HAuCl_4 , where the silver nanostructure acts as a template for the generation of GNCs and formation of Ag-Au nanoboxes. [22]

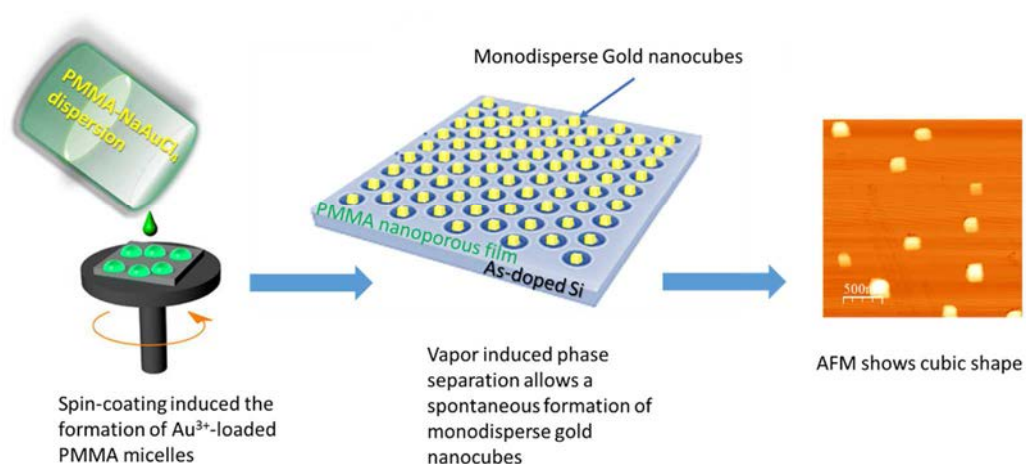
In addition, stable Gold nanocubes were synthesized by the reduction of aqueous AuCl_4 using *Bacillus licheniformis* at room temperature over a single-step process without the need of any toxic chemicals and strict conditions. [23]

According to all these works, we can conclude that no method is currently permitted to produce by a chemical process the monodispersed GNCs in a single step.

2.3 Development of polymer-self-assembly based synthesis of GNCs

The synthesis method of gold nanoparticles has been carried out by a modification of the one previously reported by our group [24],[25]. The fabrication procedure is illustrated in **Scheme 1**. Gold nanocubes are spontaneously formed upon the spincoating of gold precursor-PMMA dispersion on N-doped silicon wafer due to a rapid evaporation of the volatile solvents from PMMA. Precisely, the spincoating leads first to a self-assembly of PMMA into micelles containing Au^{3+} , and then the solvents' evaporation leads to the formation of nanoporous PMMA film, where GNPs are localized in the holes.

According to our previous works, the substrate conductivity plays a major role in the synthesis mechanism since it allows a spontaneous reduction of the gold precursor into gold nanoparticles. [24-26] Consequently, we demonstrated that the N-doped silicon substrate provides the transfer of electrons to the Au^{3+} by a reduction reaction as well described by Kalcan et al. [27] for silver nanoparticles that are produced on surface. Therefore, the GNPs are formed only on the surface of silicon, where one cannot predict their formation in solution due to the absence of a reducing agent. Moreover, the color of the Au- PMMA remains yellow until the spincoating. At this moment, the color of silicon turns into dark violet by the presence of GNPs. As discussed in a previous study, tailoring the repulsive interaction force between the couple (hydrophilic gold phase/hydrophobic PMMA phase) and the silicon wafer allows us to control the final morphology of GNPs. [26]



Scheme 1 Schematic representation of the fabrication method used in this chapter. It is observed that in the AFM image monodisperse gold nanocubes are approximately well dispersed on a silicon substrate.

On the other hand, in all our previous works on this method, we were not able to control the shape of metallic nanoparticles. In addition, the other research groups working on vapor induced phase separation (VIPS) to fabricate metallic nanoparticles did not show remarkable result on shape control using this way. [28] In this context, our major aim was to go further in the development of the VIPS to tune the nanostructures morphologies using PMMA and not a polymer block in order to simplify more the process. Knowing that Au^{3+} concentration ($[\text{Au}^{3+}]$), solvents evaporation rate and PMMA solvents are the three main components ruling the synthesis results. Here, we fixed the mixture and the spin-coating parameters which allowed us to obtain a cubic morphology. Also, tuning the precursor concentration led to control the size of the nanocubes. Consequently, we outlined the synthesis of monodispersed gold nanocubes using a method that couples self-assembly to seed mediated growth.

In our previous works using the same method, [24],[25] we obtained a high number of silver nanoparticles separated by small gaps, in relation with ultrasensitivity in SERS. Theoretical studies of closely spaced metal nanostructures have also identified the size, shape, crystal face, surface roughness, interparticle gap, the wavelength and polarization of the incident light as key factors that govern the particle-particle plasmonic coupling and then the SERS enhancement factor [17-22],[24] Consequently, we aimed to validate the synthesis process of gold nanoparticles due to the stability of gold in comparison with silver. Moreover, the synthesis of gold nanoparticles with a strong and broad SERS response is very important in a wide variety of applications including air, soil and water pollution detection, diagnosis of diseases, etc. [24],[25]

2.4 Experimental section

2.4.1 Synthesis process

First, a mixture of polymer/Gold dispersion (PMMA/Au^+) was obtained by mixing a solution of gold precursor/ethanol with a solution of Poly-methyl methacrylate (PMMA)/acetone. The Gold solution (e.g 100 mM) was prepared by the dissolution of 100 mg of Gold precursor ($\text{NaAuCl}_4 \cdot 2\text{H}_2\text{O}$) in 1ml of ethanol (called non-solvent because it's not suitable for PMMA dispersion) and stirred for 30 min at 250 rpm, followed by the addition of 0.5 ml acetone (a co-solvent acetone is a good solvent for PMMA and miscible in both solvents) in order to have a one phase mixture and stirred again for 5 min. The polymer solution (30 g/l) was prepared by dissolving 0.75 g of PMMA in 25 ml acetone (called solvent in relation with PMMA dissolving), heated for 24 hours at 40 °C with stirring at 300 rpm. After preparing the gold

solution, 1.5 g of PMMA solution is added to the gold solution and is stirred for half an hour at 250 rpm. By mixing these two solutions, gold salt-loaded polymer vesicles are produced. The formed solution (gold salt-loaded polymer vesicles) will be deposited by spincoating on a conducting substrate (N-doped silicon) that induces the reduction of Au⁺ into Au⁰ to obtain a uniform shape of GNPs which are then characterized by AFM and SEM. All the samples were prepared by the same spin coating parameters: speed 5000 rpm, acceleration 3000 rpm and 30 sec.

2.4.2 Substrate cleaning process

Arsenic-doped silicon substrates (As-Si) purchased from Silicon materials society (100 orientation, ~525 ohm resistivity) were used for coating the gold-loaded polymer dispersions. These substrates were cleaned in ultrasonic bath during 5 minutes for each step: first by soap, then by water followed by acetone and finally rinsed with 2-propanol so that they are ready for spin coating.

2.4.3 Characterization of GNCs

Atomic Force Microscopy (AFM): The AFM images were obtained using the **Nano-R2TM AFM** “high performance atomic microscope”. Contact mode and standard silicon cantilevers (APP NANO, USA), 450 μm in length and 49 μm in width were employed for imaging and the tip has the following parameters; radius: <10 nm, H: 14-16 μm, f: 11-19 kHz, k: 0.1-0.6 N/m. The scanning directly followed the topography of the surface while a constant force was maintained. As a default setting the cantilever oscillation frequency was tuned to the resonance frequency of approximately 256 kHz and the set point voltage was adjusted for optimum image quality. Both the depth and the width were recorded at a scan rate of 1Hz in 512 × 512 pixel format. It was selected for scanning the surface imaging features of the GNPs. AFM images are color-balanced using the **WSXM** program and the Pacific Nanotechnology **Nanorule+**.

Scanning Electron Microscopy (SEM), the SEM images were obtained by a Zeiss Supra 55VP operating in secondary electron imaging mode with an accelerating voltage of 2 kV and 2.7 mm working distance.

The spectroscopic Ellipsometry measurements were performed in air at room temperature using a photoelastic modulator ellipsometer (**HORIBA JOBIN YVON**) at incident angles of 60° and 70°. The measured values are the Ψ (psi) and Δ (delta) ellipsometric angles. They are related to the ratio of the Fresnel amplitude reflection coefficients of the sample. Ellipsometry

experiments followed by modeling were used to obtain the surface plasmon resonance (SPR) mode by giving the absorbance coefficient of composite layer. The physical (thickness of PMMA film) and optical properties of the layers were also determined. This technique and its optical properties will be discussed in details in chapter 4.

Dark-field images were taken by a μ -extinction setup combining a straight BX51 Olympus optical microscope and a compact spectrometer (bluewave, STE-BW-UVNb, resolution of 0.8 nm) using a Halogen source. This combined setup allows us to observe the GNPs by dark field mode and to study their optical properties through the measurement of their μ -reflection spectra.

Raman and SERS Measurements were performed using: **Dilor Jobin-Yvon Spex** instrument from HORIBA operated with laser (632.8 nm) and a CCD camera. Both excitation and collection were through a long distance (50-x objective). All the SERS spectra measurements were performed at 10 mW laser power during 10 sec of acquisition time in 1 cycle and at 985 cm^{-1} . For SERS measurements, 10 μl drop of Pyridine was deposited on substrates and kept until dried. For Raman measurements, 10 μl drop of Pyridine was deposited on silicon (As-doped substrates) surface or on PMMA film and the spectra was measured directly before drying of the drop at same SERS parameters but at 10-x objective.

2.5 Results and Discussions: experimental approach to synthesize gold nanocubes

2.5.1 Adjustment of the concentration of gold precursor

As mentioned in the introduction of this chapter, we focus on the role of the precursor concentration to achieve shape control. In bottom up synthesis, the precursor amount is generally adjusted to tune the MNPs size. Here, we expect that both the amount and the precursor molecular weight play a major role in the shape and size control. We have chosen NaAuCl_4 instead of HAuCl_4 that is widely used in the fabrication of GNPs because of its higher molecular weight and pH, which could allow faster reduction of Au^{3+} and then rapid growth of the GNPs. As mentioned before, nanocube morphology requires fast kinetics of reaction in comparison with hexagonal, rod and triangular ones. [4],[29] Therefore, we selected experimental conditions (solution composition), Silicon (weak resistivity) and spin-coating parameters (small duration, high speed) to get gold nanocubes.

First, we varied Au^{3+} concentration in order to change the size according to several studies. [24-26] **Fig. 11** shows AFM images of GNPs obtained with different $[\text{Au}^{3+}]$. There is a noticeable increase in the number of GNPs on the surface with increasing $[\text{Au}^{3+}]$. We also observe cube

like shape above a $[\text{Au}^{3+}]$ of 50 mM. The scale bar is 500 nm. Since AFM cannot give a clear idea about the shape and an accurate measurement of the GNPs size, we completed these results by SEM observation.

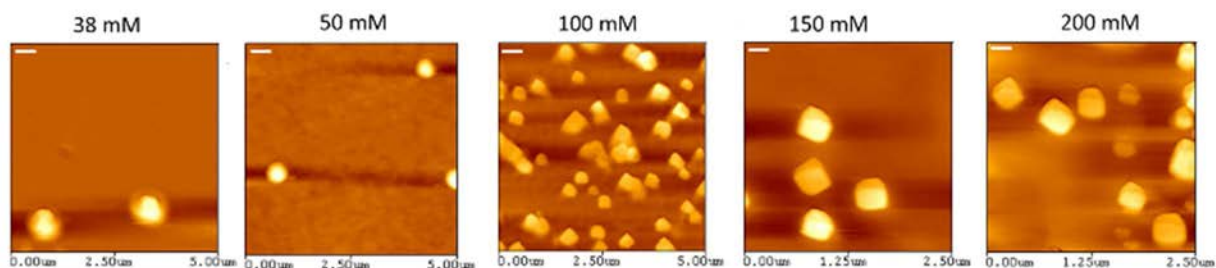


Fig. 11 AFM images of GNPs obtained with different concentrations of gold precursor (40, 50, 60, 80 and 100 mM). The scale bar is 500 nm.

SEM micrographs in Fig. 12 show the presence of two shapes and two sizes at low concentrations (40 and 50 mM) as in AFM images. The increase in concentration of gold precursor leads to the increase in the number of the GNPs progressively and the formation of a single shape of nanoparticle which is cubic.

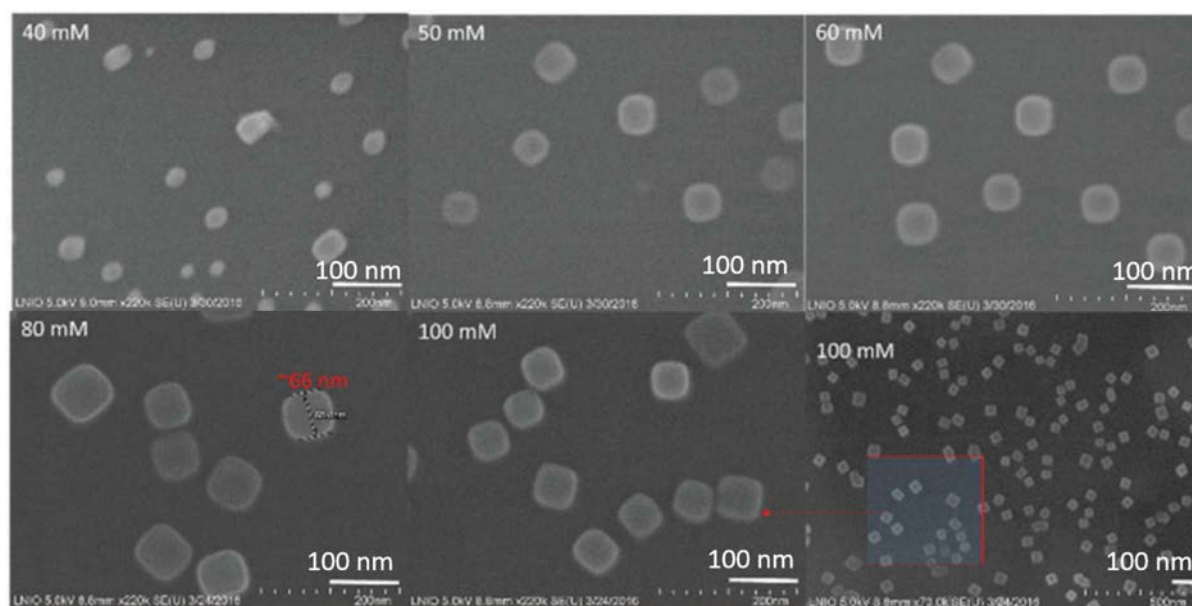


Fig. 12 SEM micrographs of GNPs obtained with different gold precursor concentrations (40, 50, 60, 80 and 100 mM). This scale bar is 100 nm.

More precisely, the size distribution decreases until 80 mM. For this reason, we determined using image-J the nanoparticle size distribution at this precursor concentration value as seen in Fig. 13. One can see that a narrow distribution is centered at ~60 nm in agreement with SEM images, which showed a ~65 nm diameter value for

80 mM. The size diameter average was then calculated from the size distribution histogram for all $[\text{Au}^{3+}]$ values. The results are listed in **Table 1**. In correlation with SEM images, the size does not change above 80 mM. Similarly, the shape distribution decreases until it becomes null at 100 mM.

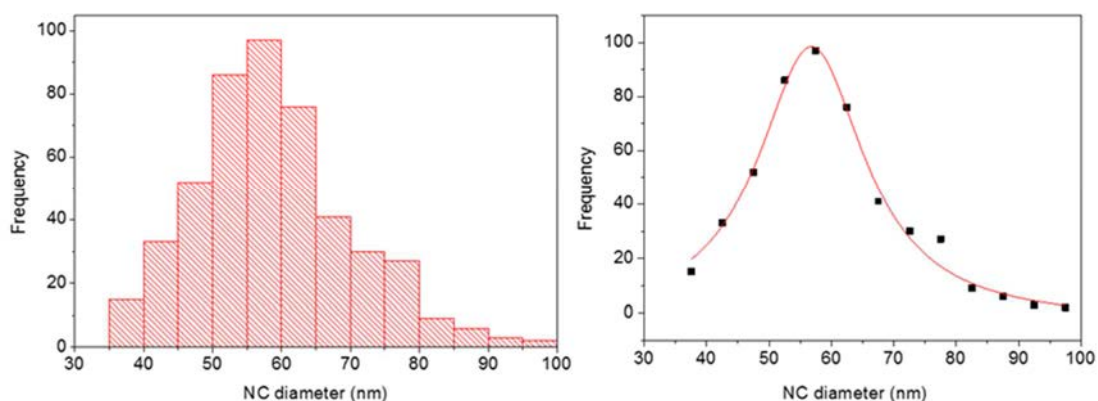


Fig. 13 Histogram of nanocubes size distribution and its corresponding Gaussian fit for the 80 mM Au^{3+} substrate.

Consequently, a 100 mM of Au^{3+} represents a critical concentration to fabricate only cubic shape of GNPs having the same size, in relation with a well-fine monodispersity. We can attribute the formation of the cubic morphology to the speed of the nucleation and growth mechanism that occurs on the surface spontaneously upon a fast evaporation of solvents. Many works have demonstrated that cube nanostructures are in principle formed through a faster rate of reaction in comparison with other morphologies. [2],[4],[29],[30]

Table 1 Average diameter of gold nanoparticles obtained with different concentration of gold precursor.

Gold precursor concentration (mM)	Average nanoparticle diameter (nm)
40	20
50	32
60	35
80	65
100	65

In order to clarify the size and shape distributions at low Au^{3+} concentrations, we observed the samples in reflection mode by dark field (DF) optical microscopy. The DF

images in Fig. 14 displayed two regimes in the color change. A first regime appears at low concentrations until 80 mM. At this stage, we observe in each image at least 2 colors, which might be attributed to the size and shape distributions. This polydispersity in color decreases with the increase of the Au³⁺ concentration from dominantly red (at 60 and 80 mM) to blue at 100 mM, in relation with the presence of uniform NPs scattering the same color at this stage. This behavior of evolution of the scattered colors from GNPs can be correlated to that observed in the above SEM micrographs. It is worthy to note that attributing a LSPR mode i.e. a surface plasmon resonance (SPR) band position for each substrate basing on the colors present on each image seems very difficult in this case because of the PMMA film that round the NPs taking into account the presence of air distance between GNPs and PMMA, which is randomly dispersed on a given substrate. This result didn't allow us to determine a refractive index around the NPs, which complicated the explanation of colors signification.

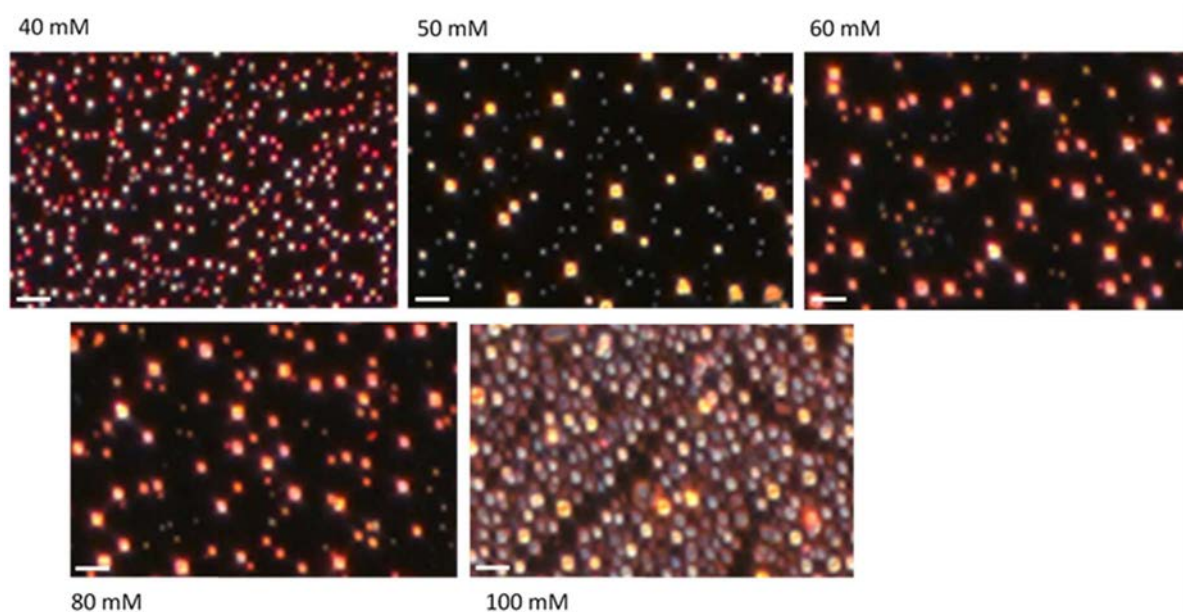


Fig. 14 Dark-field light scattering images of GNPs obtained with different gold precursor concentrations (40, 50, 60, 80 and 100 mM). Scale bar corresponds to 1 μ m.

For better understanding of these optical features, we have studied the influence of the gap between GNCs by Boundary Elementary Method (BEM).

Simulations are performed on two systems. The first system is composed of a single gold nanocube of rounded edges. Since nanocubes are located within the PMMA pores, air is used as matrix. The nanocube size is 65 nm.

The nanocube is excited by an external electric field parallel to the cube edge. The second system considered here is similar to the first one, except that we introduce another gold nanocube. The nanocubes are separated by 10 nm. This system is excited by an external electric field parallel to nanocube alignment. The refractive index of gold is given by Palik et al. [31]

The extinction cross sections of both systems are simulated in the 500-800 nm spectral range. This is achieved by solving the full Maxwell's equations according to the boundary conditions at the surface of nanocubes. The computation is performed with the MNPBEM toolbox by discretizing the surface of nanocubes in the system 1 and 2 into 2340 and 2920 elements, respectively. [32]

In Fig. 15, BEM simulations reveal that gold nanocube exhibits a single SPR band at 540 nm. Whereas, the interaction of Au-Au nanocube dimer being separated by 10 nm led to a redshift of the SPR band from 540 nm to 620 nm.

It is clearly shown in SEM micrographs the small gaps between GNPs (<10 nm) in Fig. 12 and especially above 80 nm.

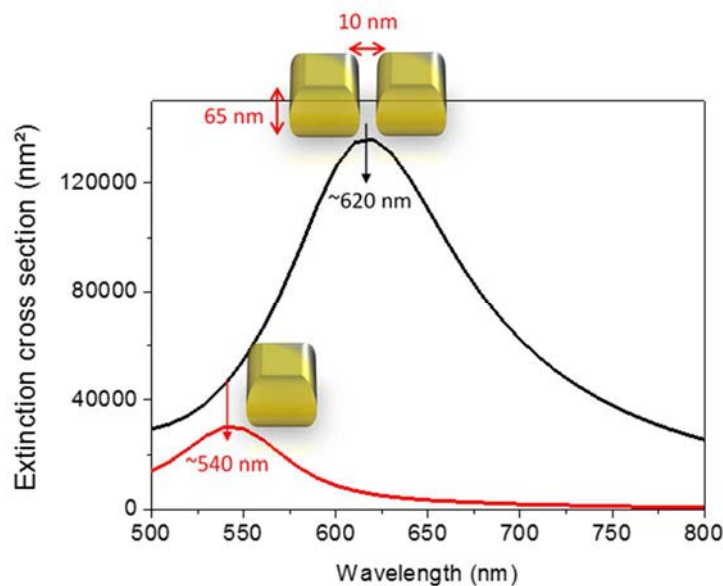
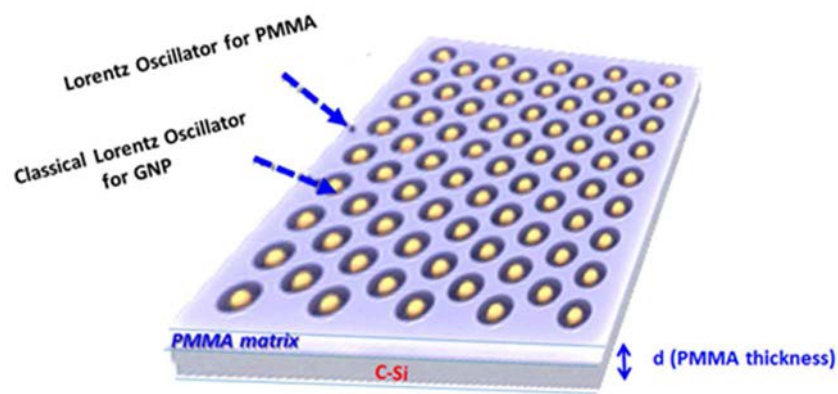


Fig. 15 Extinction cross section spectra for single and dimer of GNC calculated by BEM. Nanocube size is 65 nm and the gap between the dimer is 10 nm.

The effect of size and gap distance on the plasmonic response of paired nanocubes was also investigated through BEM simulation by Hohenester et al. [32] The authors revealed a redshift of the plasmon band by increasing the NP size, the surrounding refractive index and decreasing the gap distance. This behavior is in good agreement with our results about the gap effect.

Since it is not possible to perform absorption or extinction measurements on opaque silicon substrate and because of the complexity to deduce a plasmon response as SPR band from a reflection spectrum, we performed ellipsometry measurements to get different optical properties using the following model showed in the [Scheme 2](#). More details about theoretical model and optical method are given in chapter 4. The measured ellipsometric angles of all samples are reported in [Fig. 16](#).



Scheme 2 Schematic representation of the physical model used for ellipsometric data analysis.

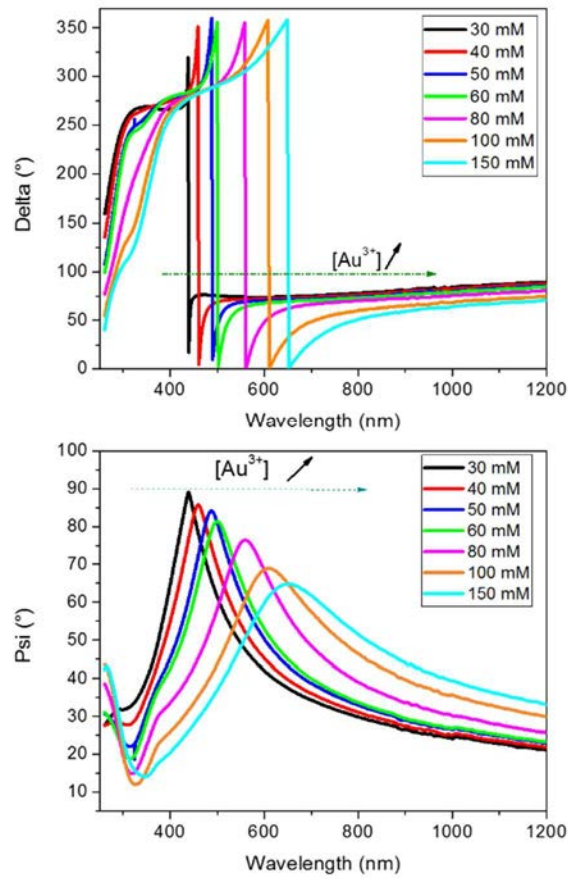


Fig. 16 Ellipsometric angles (Δ and ψ) values over increasing Au^{3+} concentration measured at incident angle of 70° .

The variations of these parameters are related to the optical properties of composite layer and sample structure, and particularly to film thickness. Indeed, these two parameters show a direct shift in the wavelength upon increasing the concentration of Au^{3+} , due to an increase of PMMA thickness as we show in Fig. 17.

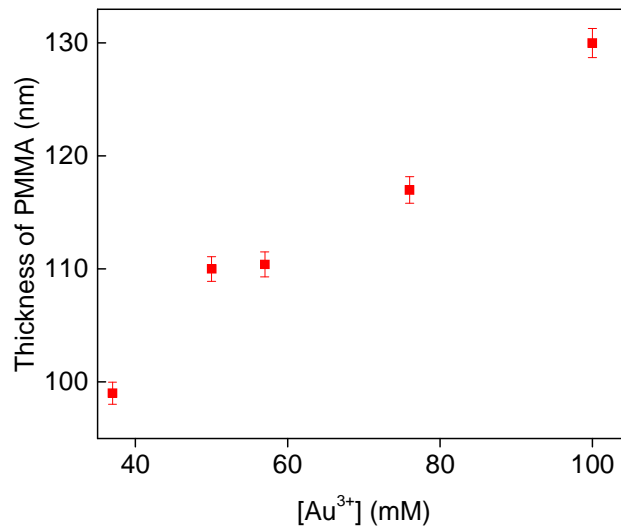


Fig. 17 Thickness of PMMA thin layer as determined by experimental ellipsometric measurements.

A continuous increase of PMMA thickness as a function of Au^{3+} concentration is observed, which may be explained by an increase of the repulsive interaction between PMMA solution and Au^{3+} one. Therefore, PMMA micelles formed on silicon surface (as described above) tend to assemble into larger ones leading to a slower evaporation rate of solvents and then to higher film thickness. Knowing the dependence of Ψ and Δ on the thickness, we might attribute their red shift to the thickness increase. [33],[34]

In order to extract the optical responses of the embedded GNPs in the PMMA layer, a correct physical model should be established to analyze the Ψ and Δ experimental data.

Thus, PMMA layer with embedded GNPs was modeled as a homogenous medium according to the two Lorentz oscillators, one in order to take into account the optical properties of PMMA film and the other is for GNPs ones. Thus, a Lorentz equation was used as the dispersion law for the dielectric function of GNPs and PMMA layer (see chapter 4). [35],[36] The known optical constants of the silicon substrate and the determined thickness values were also considered in this model (see Scheme 2).

The unknown fitting of dielectric function parameters of Lorentz oscillators was carried out simultaneously on incident angles 60° and 70° to improve the quality of the data fit. An example of the comparison between the measured spectroscopic ellipsometric spectra and the calculated ones from the proposed model is given in Fig. 18.

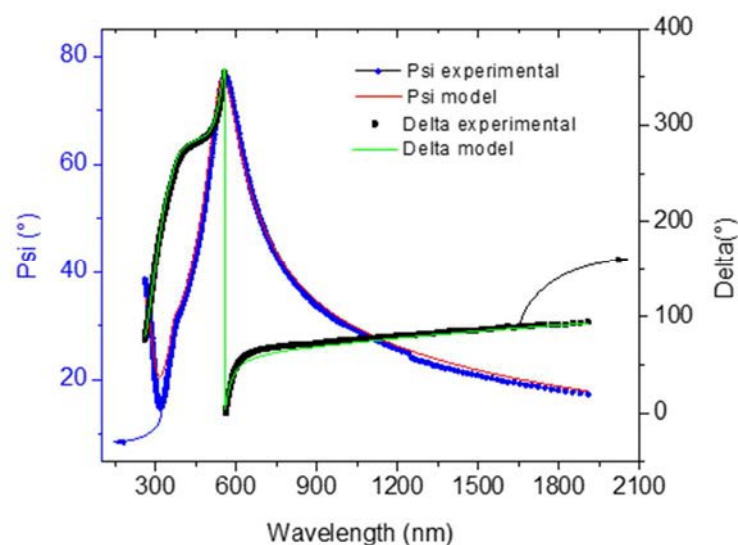


Fig. 18 Comparison between measured and calculated ellipsometric angles (Ψ and Δ) of a sample prepared with 80 mM of Au^{3+} .

A good agreement was obtained between the experimental spectra and the calculated ones by the model. This agreement highlights the homogeneity of the surface of our samples in terms of thickness. The root mean square error between the experimental and the simulated data does not exceed 1% for all films, confirming the validity of this model. The physical results obtained by this model are the dielectric function and the coefficient of absorption of composite layer (PMMA and GNPs) which allow getting the SPR band. Here we mainly discuss the results about the coefficient of absorption spectra.

Fig. 19 shows the characteristic optical absorption spectra of GNPs as a function of $[\text{Au}^{3+}]$. A continuous red shift in the SPR band is observed by the increase of Au^{3+} concentration from 30 to 150 mM. From 30 to 60 mM, the size distribution decreases in relation to the formation of a higher number of bigger nanoparticles. Thus, mainly the size increases in this region and leads to a redshift of the plasmon band. Then, above 60mM, the size remains constant against an increase of the density of nanoparticles on the substrate. According to these observations and to BEM results about the gap effect, this redshift may arise from the coupling between the closely separated nanocubes, which increases with gold precursor concentration in relation to a decrease of the gap between the GNCs.

Moreover, the increase of PMMA thickness as seen in **Fig. 17** could increase the effective refractive index of the layers, which results into a further redshift of the SPR band. As shown in **Fig. 19**, the spectral features are linked to the increase in the gold precursor concentration. A band is observed at 530 nm for the lowest Au^{3+} concentration (30 mM).

According to [Table 1](#), an average size diameter of ~ 20 nm is observed at 40 mM. Thus, smaller size of nanoparticles must be obtained at 30 mM.

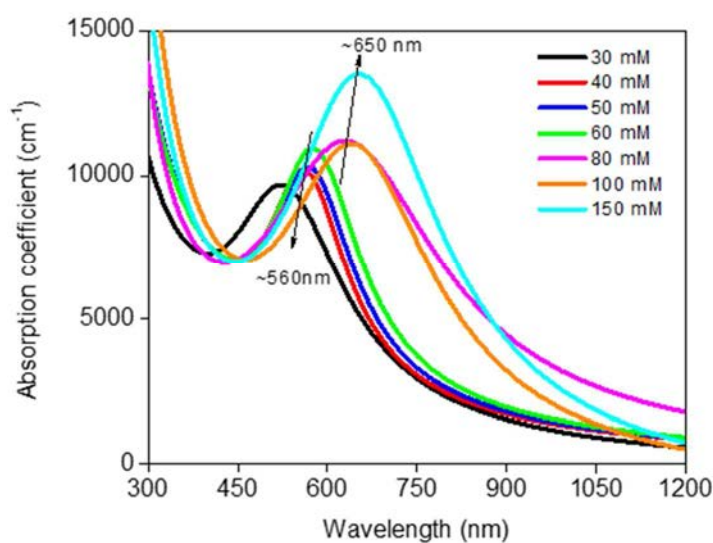


Fig. 19 Absorption coefficient of GNPs obtained with different gold precursor concentrations (40, 50, 60, 80 and 100 mM). The spectra were extracted from the analysis of ellipsometry data.

Therefore, we attribute the 530 nm band to the plasmonic response of gold nanospheres because the SEM micrographs in [Fig. 12](#) showed a major proportion of gold nanospheres with an average diameter of 20 nm. Gold nanospheres of 20 nm exhibit single SPR mode centered at 520 nm according to a wide number of studies. [37] The redshift to 530 nm observed at 30 mM Au^{3+} concentration might be due to the high refractive index of PMMA surrounding the GNPs. As observed in SEM and DF images, two regimes can be distinguished also in the absorption results. The first regime displays the same maximum SPR band at 530 nm accompanied by an increase of its intensity through an increase of $[\text{Au}^{3+}]$ at low concentrations until 60 mM.

The second regime is characterized by the presence of uniform GNCs. Thus, a continuous redshift of the SPR band until 650 nm with increasing Au^{3+} concentration is observed, which relies on the increase of the nanoparticles density on the surface at the same size of NPs (65 nm). [38] The 540 nm corresponds to the SPR band of one GNC in air by the boundary element method (BEM) simulations ([Fig. 15](#)). Moreover, some works revealed that GNCs of edge length ~ 50 nm in air have only one plasmon band at ~ 545 nm. [37],[39-41] With respect to all these points, the peak at 560 nm of low Au^{3+} concentrations corresponds to single cube SPR band influenced by the high PMMA refractive index as mentioned above. Similarly, BEM results showed that dimer of GNCs of same size

positioned along the axis (polarization 0°) has a plasmon peak at 625 nm in air. Thus, the gold nanocubes (65 nm) show a single wide peak without the appearance of any multipolar modes. On the other hand, large cube exhibits two peaks in the optical range where the long-wavelength corresponds to the dipolar plasmonic resonance and the short-wavelength peaks corresponds to the quadrupolar plasmonic resonance. [42] According to the points discussed before, the red-shift in the SPR peak as a function of gold precursor concentration is a result of an increase of the density of GNPs on silicon surface.

SERS experiments

In order to evaluate the synthesized GNCs as SERS sensors, we performed SERS measurements with 100 mM of Au^{3+} for two reasons. The first is due to the SPR band that is centered at 635 nm as obtained by ellipsometry (see Fig. 19), which is the suitable for RAMAN experiments done with a laser wavelength of 632.8 nm. It is worthy to note that the difference between the maximum SPR band and the excitation wavelength must be very low to favor a better Raman enhancement. The other reason is for using 100 mM of Au^{3+} which is the highest number of nanoparticles available to the pyridine target molecules in this sample.

Moreover, we checked the reproducibility of SERS measurements at this gold precursor concentration. For being possible, an average of 5 measured spectra were obtained on each spot, then for the 5 different spots of each substrate were calculated using 10 μl of 10^{-5} M of pyridine during an acquisition time of 10 sec. After, we compared this average of the three different substrates prepared independently with the same experimental conditions (100 mM of Au^{3+} and same spin-coating parameters). Approximately, 5 similar pyridine signatures were observed (intensity and vibration modes positions) on a given substrate (Fig. 20 a) and for the repeated same samples (Fig. 20 b). Reproducible sensors were thus prepared according to SERS results.

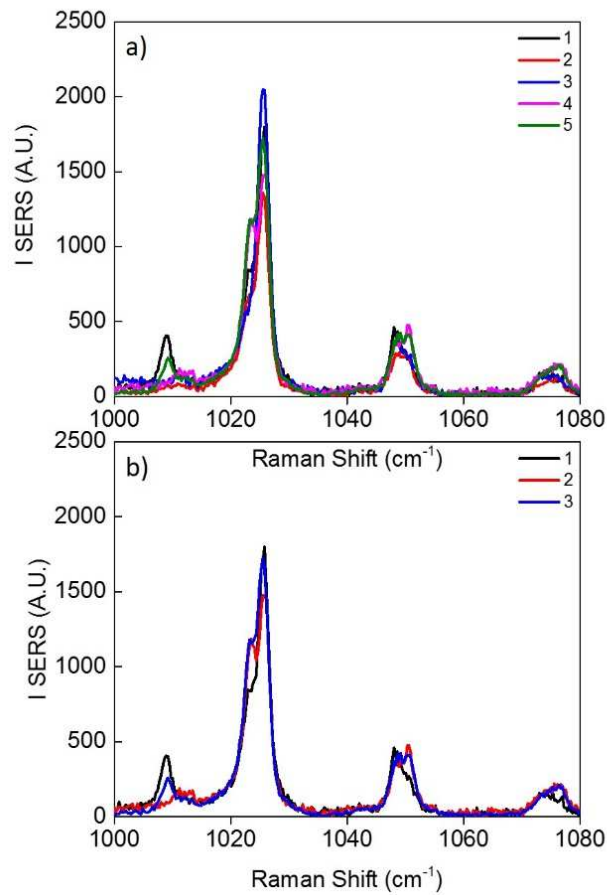


Fig. 20 SERS spectra of pyridine 10^{-5} M obtained during 10 sec for: (a) 5 different drops deposited on the surface of the 100mM substrate and (b) 3 independently repeated same samples.

In **Fig. 21 a**, we observed for the same substrate prepared with 100 mM a high enhancement of the pyridine Raman spectrum especially for both the 1023 and 1050 cm^{-1} bands. A redshift of the SERS spectra is clearly appeared as compared to the Raman one. The vibrational frequency shifts of the pyridine molecule adsorbed on metallic surfaces have been investigated even more extensively.

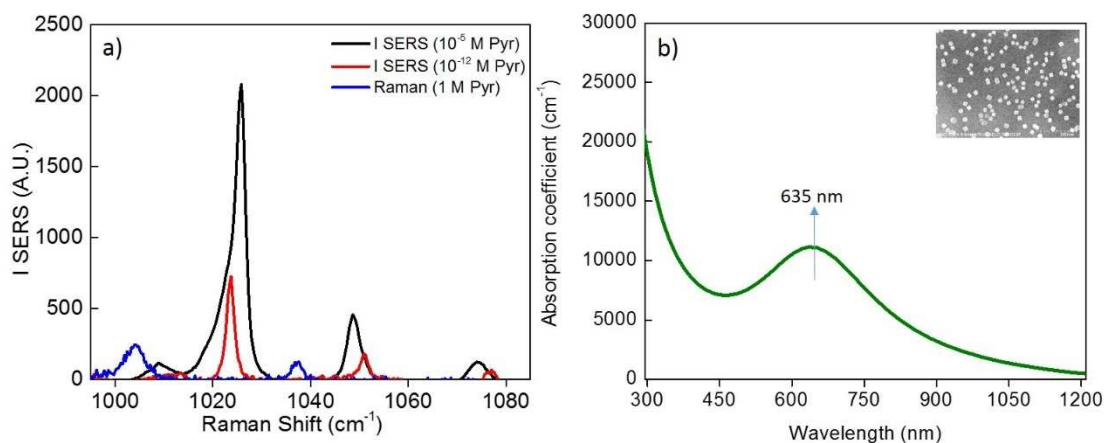


Fig. 21 (a) Average Raman spectra of pyridine 1 M and SERS ones of pyridine 10^{-5} and 10^{-12} M obtained with 100 mM of Au^{3+} , the inset shows the pyridine molecule. (b) SPR band of the corresponding substrate as obtained by ellipsometry, the inset show the SEM micrograph of the corresponding substrate.

Many studies reveal that pyridine adsorption on a metallic surface results into charge transfer complexation and might shift its frequency bands. [43] Some works showed change in the position of these frequency bands upon absorbing the pyridine on different metals. [44] So, we decreased the pyridine concentration starting from 1M until 10^{-12} M in order to determine both the detection threshold and saturation point of the produced nanosensors. Since the 100 mM substrate could be highly sensitive as described above, we determined these information for the substrate prepared with 50 mM gold concentration. A less of nanoparticles are present on the substrate surface at this value which could prevent an overestimation of the sensitivity of the obtained sensors. Thus, we plotted in Fig. 22 the SERS intensity for the 1023 and 1050 cm^{-1} bands vs the pyridine concentration. A detection limit of 10^{-12} M was measured during an acquisition time of 10 sec. The SERS intensity increases until reaching a maximum value at 10^{-5} M and then remains constant. This value may correspond to the saturation concentration of the substrate by the pyridine.

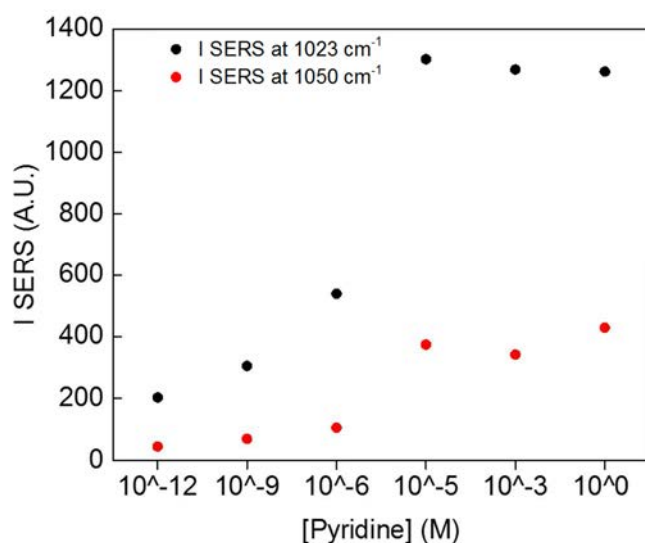


Fig. 22 SERS intensity of the 1023 and 1050 cm^{-1} bands as a function of pyridine concentration obtained for the 50 mM substrate during 10 sec.

To estimate the exact threshold of detection, we calculated the number of molecules detected in SERS for the lowest concentration of pyridine (10^{-12} mol/L) which were detected, so we obtained 4.96 molecules. The deposited pyridine aliquots (10^{-12} M) covered an area of approximately 5.106 nm^2 . In the laser spot (objective x50), we determined the surface coverage of AuNPs by pyridine and then the number of pyridine molecules excited by the laser spot, based on the substrate SEM micrograph. This calculation was done considering each NPs as a nanocube of 25350 nm^2 surface area (the cube size is 65 nm). This raw result allows to detect few molecules that lead to the single molecule detection. Also it emphasizes the ultra-sensitivity of the GNCs used since the SERS detection limit of pyridine determined in the literature nowadays is $\sim 10^{-9}$ M. [45],[46]

On the other hand, we investigated by SERS the role of gold precursor concentration to complete the study described in the previous parts. We illustrated the SERS intensity for the 1023 cm^{-1} band as a function of Au^{3+} concentration with 10^{-5} M of pyridine during 10 sec. Fig. 23 shows the relatively constant SERS intensity below 80 mM. Then, the intensity increases continuously until 100 mM. Above this value, the SERS intensity decreases. For better understanding of these results, we compared the precursor effect to the SPR wavelength one. It is noted that the maximum of SERS intensity reached at 100 mM corresponds to a SPR position of $\sim 635 \text{ nm}$. We attribute this maximum sensitivity at 100 mM to the close values of the excitation and the SPR wavelengths. According to our previous works about the sensitivity of metallic nanoparticles obtained by the present

synthesis method, we deduce that the main parameter controlling the SERS features of GNCs is the hydrophobic property of PMMA layer that allows a SERS nanofocusing. [24]

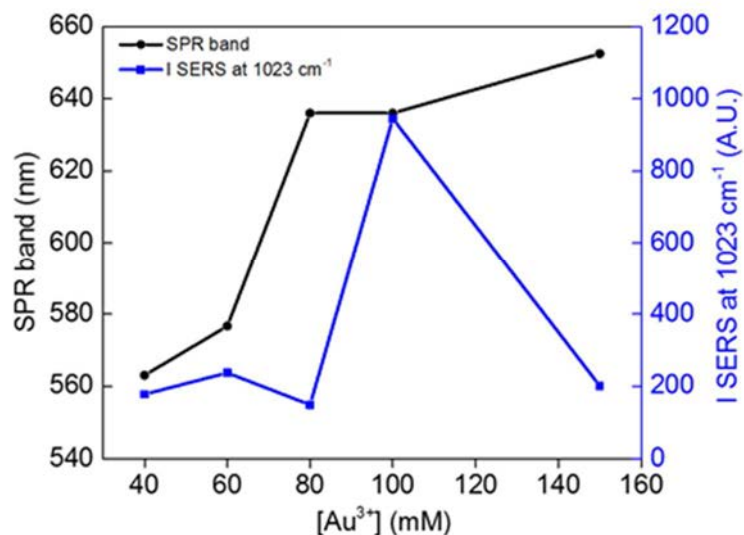
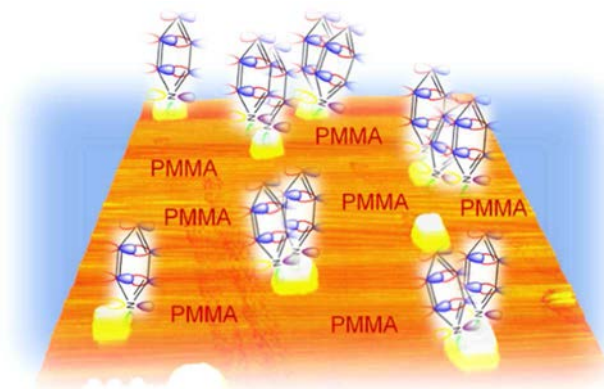


Fig. 23 SERS intensity of the 1023 cm^{-1} band and SPR plasmon band as a function of gold precursor concentration obtained with 10^{-5} M pyridine during 10 sec.

The repulsive interaction between PMMA and GNCs drives the pyridine to be adsorbed on the metal surface, which concentrates the target molecules in the SERS focal volume and highly increases the SERS intensity as shown in [Scheme 3](#).



Scheme 3 3D illustration of AFM image for gold nanocubes showing a strong adsorption of pyridine on their surface due to repulsive interaction forces with PMMA.

Moreover, the presence of high number of hot spots in the gaps between the GNPs due to the high density of GNCs on the surface could also explain the low concentration of pyridine detected. Chemical enhancement of Raman could also be expected because of the

vibrational frequency shifts as assessed above. As reported by many groups, the shifts of the pyridine internal modes is due to the charge transfer complexes by the N-end interaction between metal and pyridine. [42],[43]

As perspective, we aim to fabricate other morphologies using the method described here. We also need to go further in SERS experiments i.e. we will try to detect few number of bacteria using our substrates.

Since we weren't able to calculate the SERS enhancement factor (SEF) of the pyridine because it hasn't the same vibration modes in Raman and SERS as assessed above, we performed SERS on 4,4'-Bipyridine (4,4-BP).

Fig. 24 shows the Raman spectrum of 10^{-2} M of 4,4-BP and SERS spectrum of 10^{-5} M of 4,4-BP at the same excitation wavelength of 633 nm used for the pyridine. As described in our previous work [25], the SERS band intensities of the 4,4-BP are related to an adsorption through the N atoms of the pyridine ring on the metallic nanoparticles. This adsorption corresponds particularly to the band centered at 1450 cm^{-1} as shown in Fig. 24. Whereas, due to its high intensity, the 1640 cm^{-1} band for both SERS and Raman spectra, was considered to calculate the SEF using the following equation:

$$\text{SEF} = \left(\frac{I_{\text{SERS}}}{I_{\text{R}}} \right) \times \left(\frac{N_{\text{R}}}{N_{\text{SERS}}} \right). \quad (1)$$

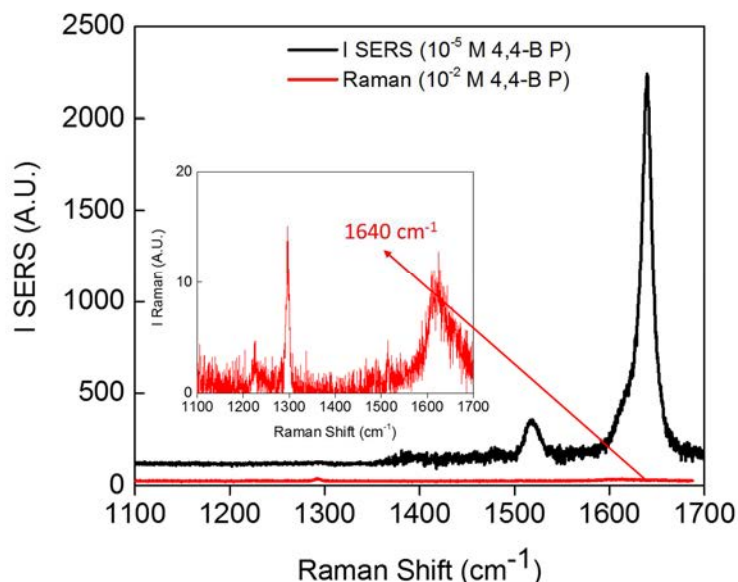


Fig. 24 Average Raman spectra of 4,4-bipyridine 10^{-2} M and SERS of 4,4-bipyridine 10^{-5} M obtained with 100 mM of Au^{3+} , the inset shows a zoom in the 4,4-BP Raman spectrum.

A focal volume of ~ 0.62 fl was obtained in the laser spot, which is given by the numerical aperture (NA) of the microscope objective (x50) and the height of the focusing scope. We determined a N_R of 4×10^6 molecules in this volume. N_{SERS} is about 30 molecules. These values give rise to an SEF of $\sim 3 \times 10^9$. This enhancement could be better with lower concentration of 4,4-BP. It is interesting to note that the highest SEF obtained nowadays is 10^{14} , [26] which reveals the high sensitivity of the GNCs observed in preliminary SERS study. This SEF could be also higher for pyridine due its better chemical adsorption on the GNCs as compared to 4,4-BP if it was possible to calculate it. Indeed, the 1450 cm^{-1} band of 4,4 BP corresponding to the chemical adsorption exhibits low intensity. However, mainly all the Raman bands of pyridine are shifted in SERS. For this reason, we were particularly interested in the detection limit of the SERS substrates, which gives a good idea about the sensitivity. Moreover, the calculation of the SEF is accompanied with many approximations and sometimes it's determined for comparison with sensors existing in the literature.

2.5.2 Role of the solvents evaporation rate in GNCs synthesis

As described before, we conclude that GNCs were formed upon evaporation of solvents from PMMA micelles and silicon after spin-coating of PMMA/NaAuCl₄ on its surface. This mechanism is called vapor-induced phase separation as mentioned in chapter 1 and it is directly dependent on the evaporation rate of solvents. This rate is proportional to the spin coating speed that controls the thickness and the size of the PMMA nanopores. For this reason, we investigated the role of the evaporation rate on the synthesis process. The aim of this study is to control in a better way the density of GNCs on the silicon surface in order to decrease further the gaps between them, which is crucial for SERS substrates. [Fig. 25](#) shows the formation of gold nanocubes whatever the evaporation rate is.

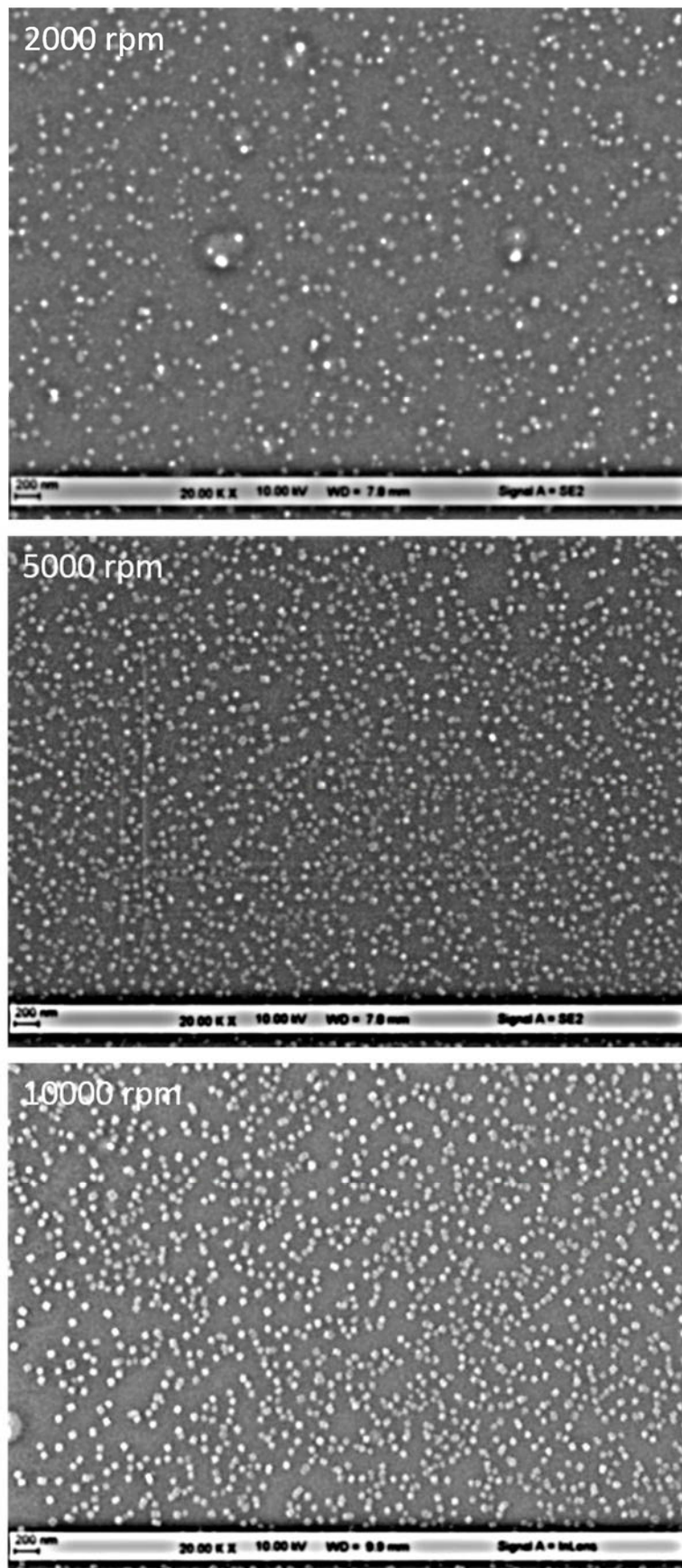


Fig. 25 SEM images showing the influence of the evaporation rate on the size distribution of the gold nanoparticles (40 mM gold precursor).

As assessed before, the high volatility of acetone and non-solvent (ethanol) was adapted to accelerate the nucleation and growth mechanism of GNPs in order to obtain the cubic morphology that is generally obtained upon rapid synthesis process. According to Fig. 25, our expectation was validated for this morphology. We see also that the increase in the evaporation rate of the solvent leads to the increase in the density of the GNPs and decrease in the gap distance separating the NPs. Referring to Fig. 26, which is a zoom view of Fig. 25, we don't observe major difference in GNCs size between the 3 SEM images. We conclude then that the size distribution decreases when the solvents evaporate rapidly, in relation with higher density of GNCs obtained on the silicon surface. Thus, to obtain monodisperse gold nanocubes, it's suitable to work with high speed of spin coating i.e. higher than 5000 rpm.

For that, we selected for the next studies the 5000 rpm as a standard speed value in order to obtain monodisperse GNPs, where the density of GNPs is very high, the size distribution is lower, the size and the shape of the of these GNPs is homogeneous on the whole substrate.

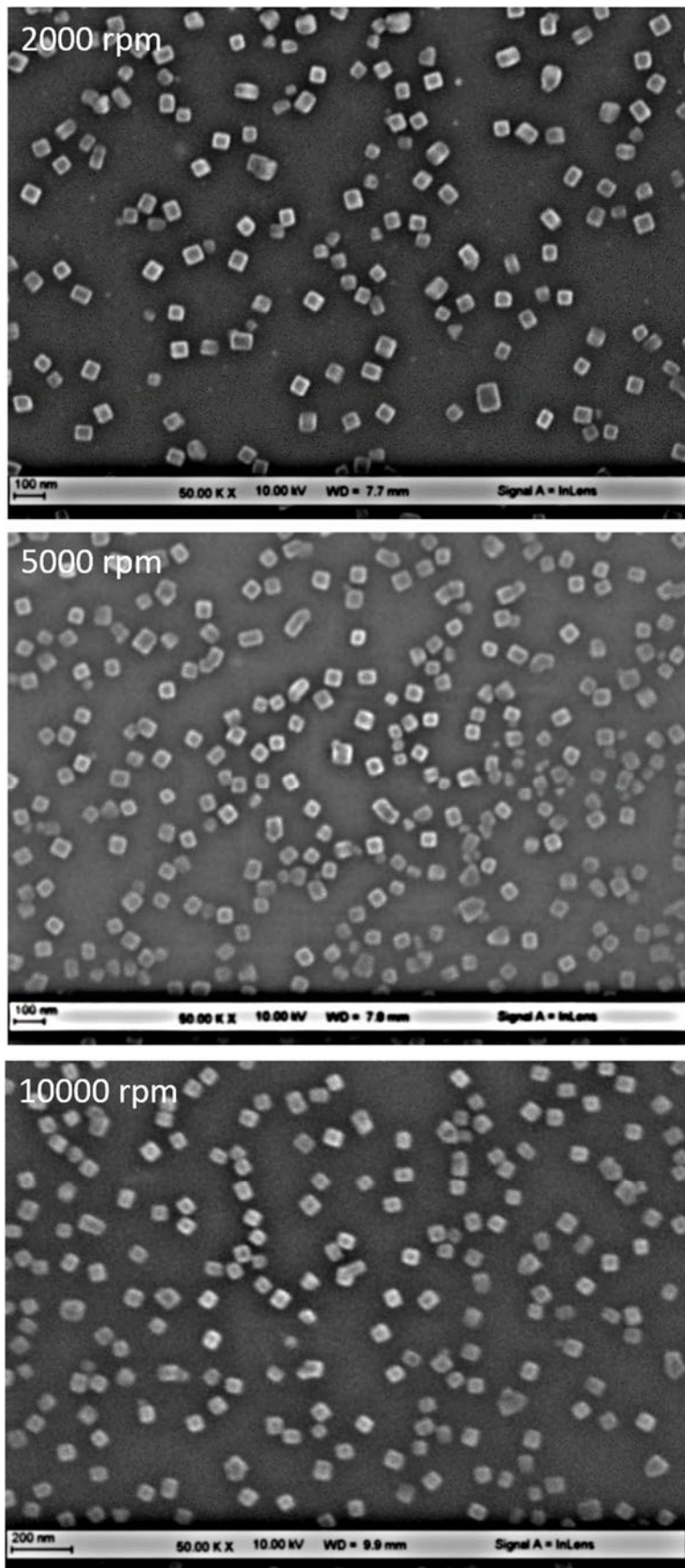


Fig. 26 SEM images showing the influence of increasing the evaporation rate on the size distribution of the gold nanoparticles (40 mM gold precursor).

2.6 Conclusion

In summary, we synthesized mono-dispersed gold nanocubes using a simple one-step method without using any surfactant or reducing agent. We reported an important red shift in the plasmonic band from 540 to 650 nm by using ellipsometry. We have also found a red shift from 540 nm to 620 nm by BEM simulations. The red shift was linked to the strong interaction between the nanoparticles separated by small interparticle distances. The good agreement between experimental ellipsometry measurements and the model ones is promising for future work on other morphologies. Gold nanocubes have been evaluated as ultrasensitive SERS sensors showing high chemical enhancement. SERS results could be promising for biosensing applications especially diseases diagnosis that require such a sensitivity (10^{-12} M as threshold of detection) and selectivity since PMMA allowed a preferential adsorption of target molecule on MNPs with any functionalizing or labelling reactions. 5 pyridine molecules were detected using the optimal sample of 100 mM characterized by a high number of nanocubes on the substrate, in relation with high density of hotspots-induced high SERS enhancement factor. A chemical enhancement was displayed for pyridine due to the shift of its Raman vibrations modes in SERS spectra for all substrates. A SERS enhancement factor of 10^9 was determined for the 4,4-bipyridine, which matches with the values of the ultrasensitive SERS substrates reported in the literature.

2.7 References

- [1] Scholl, J. A., Koh, A. L., & Dionne, J. A. (2012). Quantum plasmon resonances of individual metallic nanoparticles. *Nature*, 483(7390), 421-429.
- [2] Sun, Y., & Xia, Y. (2002). Shape-controlled synthesis of gold and silver nanoparticles. *Science*, 298(5601), 2176-2179.
- [3] Zhang, F., Zhu, J., An, H. Q., Li, J. J., & Zhao, J. W. (2016). A two-step approach to realize size-and shape-selective separation of crude gold nanotriangles with high purification. *Journal of Materials Chemistry C*, 4(3), 568-580.
- [4] Huang, C. J., Chiu, P. H., Wang, Y. H., Chen, W. R., & Meen, T. H. (2006). Synthesis of the gold nanocubes by electrochemical technique. *Journal of The Electrochemical Society*, 153(8), D129-D133.
- [5] Kang, B., Afifi, M. M., Austin, L. A., & El-Sayed, M. A. (2013). Exploiting the nanoparticle plasmon effect: observing drug delivery dynamics in single cells via Raman/fluorescence imaging spectroscopy. *ACS nano*, 7(8), 7420-7427.
- [6] Wagstaff, A. J., Brown, S. D., Holden, M. R., Craig, G. E., Plumb, J. A., Brown, R. E., ... & Wheate, N. J. (2012). Cisplatin drug delivery using gold-coated iron oxide

- nanoparticles for enhanced tumour targeting with external magnetic fields. *Inorganica Chimica Acta*, 393, 328-333.
- [7] Miranda, O. R., Li, X., Garcia-Gonzalez, L., Zhu, Z. J., Yan, B., Bunz, U. H., & Rotello, V. M. (2011). Colorimetric bacteria sensing using a supramolecular enzyme–nanoparticle biosensor. *Journal of the American Chemical Society*, 133(25), 9650-9653.
- [8] Huang, X., El-Sayed, I. H., Qian, W., & El-Sayed, M. A. (2006). Cancer cell imaging and photothermal therapy in the near-infrared region by using gold nanorods. *Journal of the American Chemical Society*, 128(6), 2115-2120.
- [9] Jain, P. K., Huang, X., El-Sayed, I. H., & El-Sayed, M. A. (2008). Noble metals on the nanoscale: optical and photothermal properties and some applications in imaging, sensing, biology, and medicine. *Accounts of chemical research*, 41(12), 1578-1586.
- [10] O'Neal, D. P., Hirsch, L. R., Halas, N. J., Payne, J. D., & West, J. L. (2004). Photo-thermal tumor ablation in mice using near infrared-absorbing nanoparticles. *Cancer letters*, 209(2), 171-176.
- [11] Huang, X., Jain, P. K., El-Sayed, I. H., & El-Sayed, M. A. (2008). Plasmonic photothermal therapy (PPTT) using gold nanoparticles. *Lasers in medical science*, 23(3), 217-228.
- [12] El-Sayed, I. H., Huang, X., & El-Sayed, M. A. (2006). Selective laser photo-thermal therapy of epithelial carcinoma using anti-EGFR antibody conjugated gold nanoparticles. *Cancer letters*, 239(1), 129-135.
- [13] Stuart, D. A., Haes, A. J., Yonzon, C. R., Hicks, E. M., & Van Duyne, R. P. (2005, February). Biological applications of localised surface plasmonic phenomena. In *IEE Proceedings-Nanobiotechnology* (Vol. 152, No. 1, pp. 13-32). IET.
- [14] Ahn, H. Y., Lee, H. E., Jin, K., & Nam, K. T. (2013). Extended gold nano-morphology diagram: synthesis of rhombic dodecahedra using CTAB and ascorbic acid. *Journal of Materials Chemistry C*, 1(41), 6861-6868.
- [15] Chiu, C. Y., Chung, P. J., Lao, K. U., Liao, C. W., & Huang, M. H. (2012). Facet-dependent catalytic activity of gold nanocubes, octahedra, and rhombic dodecahedra toward 4-nitroaniline reduction. *The Journal of Physical Chemistry C*, 116(44), 23757-23763.
- [16] Jin, R., Egusa, S., & Scherer, N. F. (2004). Thermally-induced formation of atomic Au clusters and conversion into nanocubes. *Journal of the American Chemical Society*, 126(32), 9900-9901.
- [17] Sau, T. K., & Murphy, C. J. (2004). Room temperature, high-yield synthesis of multiple shapes of gold nanoparticles in aqueous solution. *Journal of the American Chemical Society*, 126(28), 8648-8649.
- [18] Skrabalak, S. E., Chen, J., Sun, Y., Lu, X., Au, L., Copley, C. M., & Xia, Y. (2008). Gold nanocages: synthesis, properties, and applications. *Accounts of chemical research*, 41(12), 1587-1595.
- [19] Sohn, K., Kim, F., Pradel, K. C., Wu, J., Peng, Y., Zhou, F., & Huang, J. (2009). Construction of evolutionary tree for morphological engineering of nanoparticles. *ACS nano*, 3(8), 2191-2198.

- [20] Lin, Q. Y., Li, Z., Brown, K. A., O'Brien, M. N., Ross, M. B., Zhou, Y., ... & Aydin, K. (2015). Strong coupling between plasmonic gap modes and photonic lattice modes in DNA-assembled gold nanocube arrays. *Nano letters*, 15(7), 4699-4703.
- [21] Zhang, J., Langille, M. R., Personick, M. L., Zhang, K., Li, S., & Mirkin, C. A. (2010). Concave cubic gold nanocrystals with high-index facets. *Journal of the American Chemical Society*, 132(40), 14012-14014.
- [22] Sun, Y., & Xia, Y. (2004). Mechanistic study on the replacement reaction between silver nanostructures and chloroauric acid in aqueous medium. *Journal of the American Chemical Society*, 126(12), 3892-3901.
- [23] Kalishwaralal, K., Deepak, V., Pandian, S. R. K., & Gurunathan, S. (2009). Biological synthesis of gold nanocubes from *Bacillus licheniformis*. *Bioresource technology*, 100(21), 5356-5358.
- [24] Akil-Jradi, S., Jradi, S., Plain, J., Adam, P. M., Bijeon, J. L., Royer, P., & Bachelot, R. (2012). Micro/nanoporous polymer chips as templates for highly sensitive SERS sensors. *RSC Advances*, 2(20), 7837-7842.
- [25] Khanafer, M., Izquierdo-Lorenzo, I., Akil, S., Louarn, G., Toufaily, J., Hamieh, T., ... & Jradi, S. (2016). Silver Nanoparticle Rings of Controllable Size: Multi-Wavelength SERS Response and High Enhancement of Three Pyridine Derivatives. *ChemistrySelect*, 1(16), 1201-1206.
- [26] Khanafer, M., Issa, A., Akil, S., Hamieh, T., Adam, P. M., & Jradi, S. (2016). A general strategy to incorporate a wide range of metallic salts into ring-like organized nanostructures via polymer self-assembly. *RSC Advances*, 6(105), 102843-102852.
- [27] Kalkan, A. K., & Fonash, S. J. (2005). Electroless synthesis of Ag nanoparticles on deposited nanostructured Si films. *The Journal of Physical Chemistry B*, 109(44), 20779-20785.
- [28] Fahmi, A., Pietsch, T., Mendoza, C., & Cheval, N. (2009). Functional hybrid materials. *Materials Today*, 12(5), 44-50.
- [29] Khodashenas, B., & Ghorbani, H. R. (2015). Synthesis of silver nanoparticles with different shapes. *Arabian Journal of Chemistry*.
- [30] Sriram, M., Zong, K., Vivekchand, S. R. C., & Gooding, J. J. (2015). Single nanoparticle plasmonic sensors. *Sensors*, 15(10), 25774-25792.
- [31] E. D. Palik, *Handbook of Optical Constants of Solids*, Academic press handbook series, New York, 1985.
- [32] Hohenester, U., & Trügler, A. (2012). MNPBEM—A Matlab toolbox for the simulation of plasmonic nanoparticles. *Computer Physics Communications*, 183(2), 370-381.
- [33] Battie, Y., Izquierdo-Lorenzo, I., Resano-Garcia, A., Naciri, A. E., Akil, S., Adam, P. M., & Jradi, S. (2016). How to determine the morphology of plasmonic nanocrystals without transmission electron microscopy?. *Journal of Nanoparticle Research*, 18(8), 2.
- [34] Moughames, J., Jradi, S., Chan, T. M., Akil, S., Battie, Y., Naciri, A. E., ... & Cousin, J. (2016). Wavelength-scale light concentrator made by direct 3D laser writing of polymer metamaterials. *Scientific reports*, 6.

- [35] Voué, M., Dahmouchene, N., & De Coninck, J. (2011). Annealing of polymer films with embedded silver nanoparticles: Effect on optical properties. *Thin Solid Films*, 519(9), 2963-2967.
- [36] Guyot, C., & Voué, M. (2007). Optical behavior of poly-(vinyl) alcohol films embedding silver nanoparticles: a statistical analysis of the film thickness effect. *J. Nanosci. Nanotechnol*, 7, 1.
- [37] Alsawafra, M., Wahbeh, M., & Truong, V. V. (2012). Simulated optical properties of gold nanocubes and nanobars by discrete dipole approximation. *Journal of Nanomaterials*, 2012, 2.
- [38] Jeon, J. W., Ledin, P. A., Geldmeier, J. A., Ponder Jr, J. F., Mahmoud, M. A., El-Sayed, M., ... & Tsukruk, V. V. (2016). Electrically Controlled Plasmonic Behavior of Gold Nanocube@ Polyaniline Nanostructures: Transparent Plasmonic Aggregates. *Chemistry of Materials*, 28(8), 2868-2881.
- [39] Hohenester, U., & Krenn, J. (2005). Surface plasmon resonances of single and coupled metallic nanoparticles: A boundary integral method approach. *Physical Review B*, 72(19), 195429.
- [40] Link, S., & El-Sayed, M. A. (1999). Size and temperature dependence of the plasmon absorption of colloidal gold nanoparticles. *The Journal of Physical Chemistry B*, 103(21), 4212-4217.
- [41] Jin, R., Cao, Y., Mirkin, C. A., Kelly, K. L., Schatz, G. C., & Zheng, J. G. (2001). Photoinduced conversion of silver nanospheres to nanoprisms. *Science*, 294(5548), 1901-1903.
- [42] Hu, M., Chen, J., Li, Z. Y., Au, L., Hartland, G. V., Li, X., ... & Xia, Y. (2006). Gold nanostructures: engineering their plasmonic properties for biomedical applications. *Chemical Society Reviews*, 35(11), 1084-1094.
- [43] Elsayed, M. Y., Gouda, A. M., Ismail, Y., & Swillam, M. A. (2017, February). Silver-decorated silicon nanowires array as surface-enhanced Raman scattering (SERS) substrate. In *Proc. of SPIE Vol* (Vol. 10112, pp. 1011224-1).
- [44] Wu, D. Y., Liu, X. M., Duan, S., Xu, X., Ren, B., Lin, S. H., & Tian, Z. Q. (2008). Chemical enhancement effects in SERS spectra: A quantum chemical study of pyridine interacting with copper, silver, gold and platinum metals. *The Journal of Physical Chemistry C*, 112(11).
- [45] Yang, Z., Li, Y., Li, Z., Wu, D., Kang, J., Xu, H., & Sun, M. (2009). Surface enhanced Raman scattering of pyridine adsorbed on Au@ Pd core/shell nanoparticles. *The Journal of chemical physics*, 130(23), 234705.
- [46] Elsayed, M. Y., Gouda, A. M., Ismail, Y., & Swillam, M. A. (2017). Silicon-based SERS substrates fabricated by Electroless etching. *Journal of Lightwave Technology*.

3 Synthesis strategy of gold nanoparticles with different shapes

3.1 Introduction

The shape is one of the most important factors in determining the structural, physical, and chemical properties of a nanoparticle. [1] Shape-controlled synthesis of nanoparticles has become a recent focus as different shapes of the particles can introduce electronic, optical, and magnetic properties that are different from those observed in their spherical counterparts. [2] As the restoring force on the conduction electrons is extraordinarily sensitive to particle curvature, nonspherical metallic nanoparticles, produced via various approaches, [3] have been found to shift their surface plasmon frequency drastically, making them useful as multicolor diagnostic labels and for other optical devices. [4]

By means of versatile, colloidal synthesis ways, a variety of shapes have also been reported so far, including the conventional 3D shapes (cube, tetrahedron, octahedron, decahedron, and icosahedrons), and 1- or 2D shapes (rod, wire, plate, disc, triangle, hexagon, tetrapods, bi-pyramid, and highly branched structures). [5] Nanoparticles with high surface areas can provide more active sites to lower the activation energy for catalytic reactions, and unique surface structures—such as steps, kinks, and terraces to influence the reaction pathways leading to product selectivity. Recent studies show that turnover rates and selectivity of catalytic reactions can be influenced strongly by the size and the shape of the nanoparticles, as their surface structures and active sites can be tailored at the molecular level. [6] The formation of different shapes is generally achieved by changing the reducing and stabilizing factors upon colloidal synthesis. In parallel, many studies have investigated the role of ligands (e.g., halides or small molecules such as citrate and cetyltrimethylammonium bromide) in controlling NP morphologies. [7] In addition to colloidal approaches, in recent years, new methods have been proposed to synthesize non-spherical nanoparticles. Abid et al. showed that by using various irradiation methods, silver nanoparticles could be synthesized. Laser irradiation of aqueous solution of a silver salt and surfactant could synthesize silver nanoparticles with suitable shape and size. [8] This corresponds to the photochemical reduction process that enables the shape evolution depending on the photonic parameters (light power, exposure time, etc.). Recently, a study reported that the DNA-mediated morphological evolution of gold nanoprisms seeds into different shapes. [9] This work was developed in chapter 1. In [Table 2](#), we cite several methods used to control the shape of silver nanoparticles. These approaches have also been used for the synthesis of other metallic nanoparticles (Au, Pt, Cu, Al, etc.).

Table 2 Summary of the most known biological, chemical and physical methods used to synthesize metallic nanoparticles with different shapes. The table is adapted from ref. [10]

Method	Reducing agent or solvent	Stabilizer or surfactant	Particle size	Shape	Ref.
Chemical method	Trisodium citrate	Trisodium citrate	30–60 nm	Spherical	Rivas and Garc (2001)
Chemical method	NaBH ₄	Dodecanoic acid (DDA)	~7 nm	Spherical	Lee et al. (2006)
Chemical method	Ethylene glycol	PVP	17 ± 2 nm	Spherical	Kim et al. (2006)
Chemical method	Paraffin	Oleylamine	10–14 nm	Spherical	Sato-Berfu et al. (2009)
Chemical reduction	Hydrazine hydrate	Bis(2-ethylhexyl) (sulfosuccinate AOT)	2–5 nm	Spherical	Zhang et al. (2007)
Photo chemical reduction (X-ray radiolysis)	X-ray	–	28 nm	Spherical	Remita et al. (2007)
Electrochemical (polyol process)	Electrolysis cathode: titanium anode: Pt	Polyvinyl pyrrolidone (PVP)	11	Spherical	Lim et al. (2006)
Physical synthesis	Electrical arc discharge	Sodium citrate	14–27 nm	Spherical	Ashkarran (2010)
Physical synthesis	TX-100, UV	TX-100	30 nm	Spherical	Ghosh et al. (2003)
Biological synthesis	Bacillus sp.	Bacillus sp.	5–15 nm	Spherical	Pugazhenthiran et al. (2009)
Biological synthesis	Lactobacillus	Lactobacillus Proteins	6–15.7 nm	Spherical	Sintubin et al. (2009)
Biological synthesis	<i>Shewanella oneidensis</i>	<i>Shewanella oneidensis</i>	2–11 nm	Spherical	Suresh et al. (2010)
Biological synthesis	Fungus <i>T. viride</i>	<i>Trichoderma viride</i>	5–40 nm	Spherical	Fayaz et al. (2010)
Biological synthesis	<i>Cassia angustifolia</i>	<i>Cassia angustifolia</i>	9–31 nm	Spherical	Amaladhas et al. (2012)
Biological synthesis	<i>Daucus carota</i>	<i>Daucus carota</i>	20 nm	Spherical	Umadevi et al. (2012)
Biological synthesis	Bacillus strain CS 11	Bacillus strain CS 11	42–92 nm	Spherical	Das et al. (2013)
Biological synthesis	<i>Aspergillus niger</i>	<i>Aspergillus niger</i>	1–20 nm	Spherical	Sagar and Ashok (2012)
Biological synthesis	<i>Arbutus unedo</i> leaf extract	<i>Arbutus unedo</i> leaf extract	3–20 nm	Spherical	Kouvaris et al. (2012)
Chemical method	Ethylene glycol	PVP	–	Cubic	Sun and Xia (2002a)
Chemical method	Pentenediol (H-1.5 PDO)	PVP	–	Cubic	Tao et al. (2006)
Chemical method	Ethylene glycol	PVP	30–50 nm	Cubic	Young et al. (2007)
Photochemical	Carboxymethylated chitosan (CMCTS)	Carboxymethylated chitosan (CMCTS)	2–8 nm	Cubic	Huang et al. (2008)
Biological synthesis	Leaf extracts from <i>Eucalyptus macrocarpa</i>	Leaf extracts from <i>Eucalyptus macrocarpa</i>	10–50 nm (mean crystallite size = 38 ± 2 nm)	Cubic	Poinern et al. (2013)
Wet-chemical	Sodium borohydride in the presence of sodium citrate	–	4 ± 2 nm	Nanorods	Aslan et al. (2005)
Chemical method	Potassium tartaric	PVP	–	Nanorods	Gu et al. (2006)
Chemical method (soft, solution-phase)	Ethylene glycol	–	Diameters of 30–40 nm	Nanowires	Sun et al. (2002a)
Wet chemical	Ascorbic acid	–	In diameter 30–40 nm	Nanowires	Zhang et al. (2004a)
Microwave technique	Ethylene glycol	PVP	–	Nanowires	Nghia et al. (2012)
Chemical method (polyol)	Ethylene glycol	PVP	–	Nanobars	Wiley et al. (2007)
Chemical reduction	Hydrazine hydrate	PVP	50–200 nm	Triangular	Kai et al. (2012)
Microwave-assisted	Ethylene glycol monoalkyl ethers	PVP	–	Nanoprisms	Darmanin et al. (2012)

Despite the progress in the above mentioned methods, it is still difficult to achieve systematic and predictive tuning of the NP morphologies because of the limited fundamental understanding of the formation of NP morphologies and the mechanistic roles of the molecules used especially in the ligands. [11] To meet the challenge of shape-controlled synthesis, this chapter is an attempt to fabricate gold nanoparticles with different shapes using our method that was described in chapter 2. Thus, we aim to show the evolution of the cubic shape into another morphology by changing the major process components.

3.2 Shape-controlled nanotechnologies of metallic nanoparticles

Among recent methods, the most versatile way of fabricating metal nanoparticles with well-defined structure is colloid approach. Although the most well-known and stable morphology of metallic nanoparticles is cubic close packing, various shapes can be obtained by changing the experimental parameters by means of the colloidal mechanisms. In the following section, we hope to provide a better understanding of colloidal synthesis strategies investigated until now in shape control.

3.2.1 Overview of colloidal synthesis of monodispersed metal nanoparticles

Spherical nanoparticles are generally produced by Turkevich method (first 1951), i.e. citrates are used to reduce metal ions in an aqueous solution. Consequently, a special morphology is prepared by adding polyvinylpyrrolidone (PVP) into an ethylene glycol solution of silver nitrate in controlled proportions to induce the anisotropic propagation. [12]

A metal precursor, a surfactant, a solvent, and a reducing agent are the four ingredients needed for the colloidal synthesis of metal nanoparticles. Generally, a precursor, in the form of ionic salts (metal nitrate, sulfate, chloride, acetate, etc.) is selected and dissolved into the solvent in the presence of surfactants.

Then, the reduction process then proceeds, at room temperature, to generate metallic nanoparticles by introducing a reducing agent. A surfactant endows colloidal stability of nanoparticles to prevent aggregation and precipitation in the solution. Many kinds of surfactants are selected, and their concentration and relative ratio to the precursors control the particle size and shape. Indeed, surfactants play an important role in directing particle growth, and restricting particle size by interacting with metal surfaces during the reaction. As the binding affinity of a surfactant varies from one crystal facet to another, a preferential binding to one certain facet, attached to the surfactant, results in hindering its growth. Therefore, another surfactant as a structure-directing agent is added for the shape control. Adjusting these main components allows to control the final size and shape of the metal nanoparticles. [Fig. 27](#) illustrates this general mechanism (nucleation and growth mechanism) allowing the size and shape control of the metallic nanoparticles.

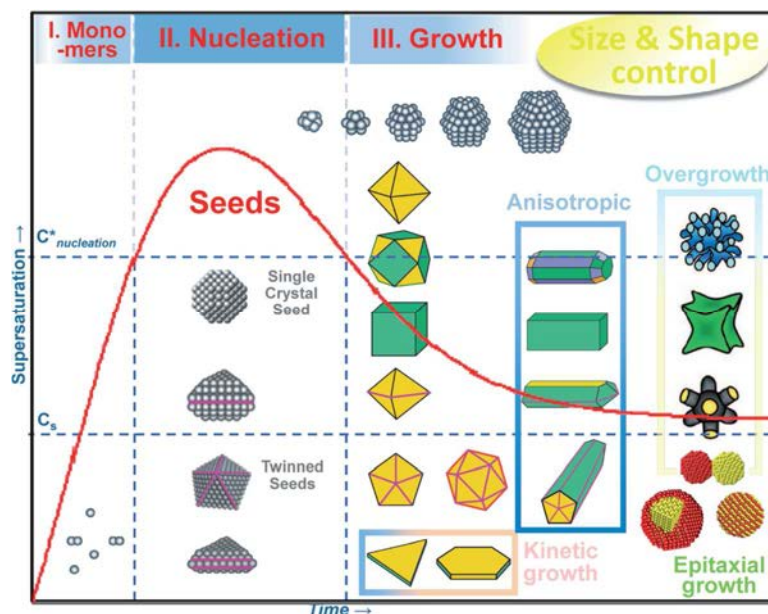


Fig. 27 Schematic representation of general synthesis approaches for size and shape control of metal nanoparticles combining with the LaMer diagram. Adapted from ref. [13]

Among colloidal synthetic strategies, Seed-mediated growth (SMG) is the most used one to fabricate metallic nanoparticles of diverse shapes. SMG is carried out via the preparation of two solutions (see Fig. 28). In the first solution; metal ions are reduced in water at room temperature, with strong reducing agent (sodium borohydride, NaBH_4) to form spherical nanoparticles seeds of 3-4 nm in diameter. In the second one, the seeds are introduced into a growth solution containing the reducing agent, surfactant and metal precursor. Reducing agents such as ascorbic acid are involved in the growth solution in order to reduce M^{n+} into M^0 . Therefore, the surface binding of such metal ions or surfactant into preferable crystal facets of the seeds is favored. As a result, the NPs are formed through the formation of positively charged bilayer as described in chapter 1 for the synthesis of gold nanorods.

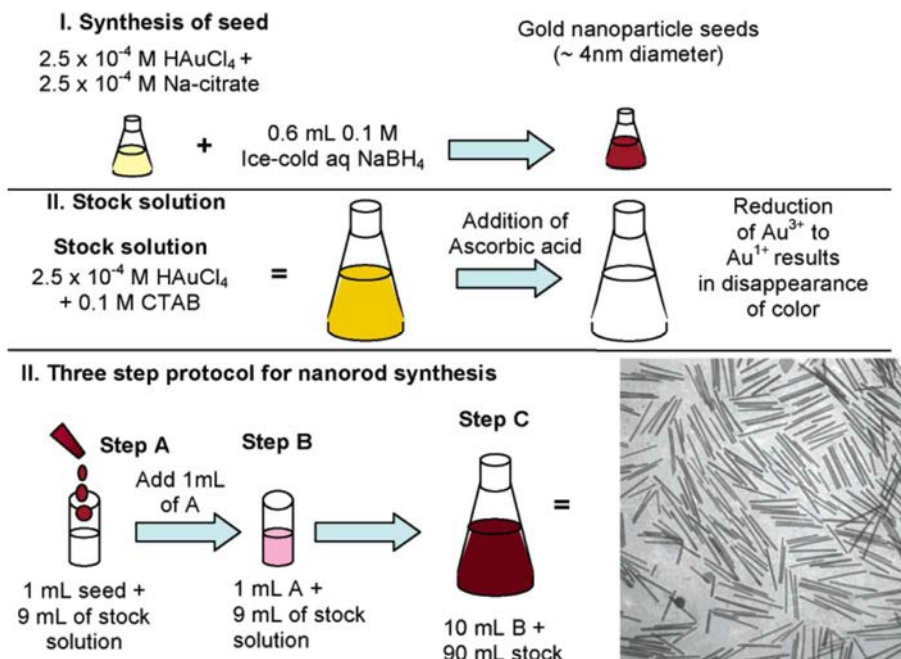


Fig. 28 Illustration of the seed-mediated growth process to produce gold nanorods with different aspect ratios. Adapted from ref. [14]

In this context, the growth mechanism of different morphologies of metallic nanoparticles can be achieved through modifying the reaction conditions such as the surfactant chain length and concentration (see Fig. 29), the metal salt concentration and the reduction kinetics (reducing agents and acid concentration), allowing the nanorods formation (as seen in Fig. 28). [15-17]

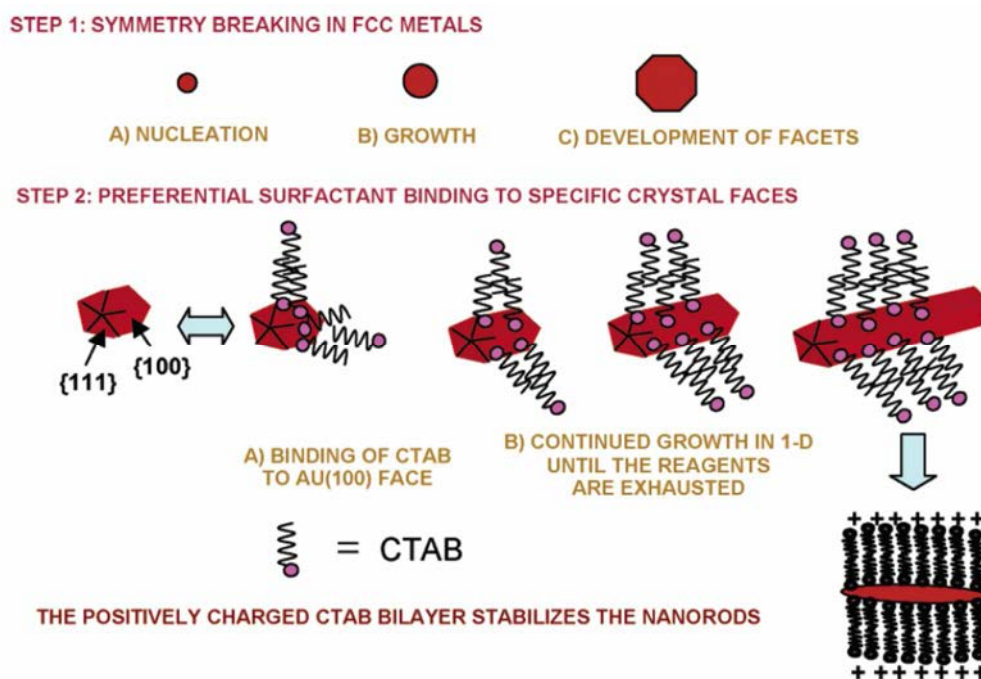


Fig. 29 Illustration of seed-mediated growth mechanism allowing the synthesis of metal nanorods of different aspect ratios through adjusting the surfactant amount (adapted from ref. 14).

According to SMG mechanism, the rate of the reaction (kinetics) is a clever combination of the four components cited above and could be the crucial factor that controls the final shape.

Fig. 30 shows that slower rates of the reaction yield lower-energy surface facets using lower amount of reducing agents (ascorbic acid) or by introducing halides (bromide or iodide). In contrast, the increase in the concentration of ascorbic acid accelerates both the rate of metal ions reduction and the growth kinetics of nanoparticles. Consequently, kinetically nanoparticles with higher-energy surface facets are favored. [18],[19]

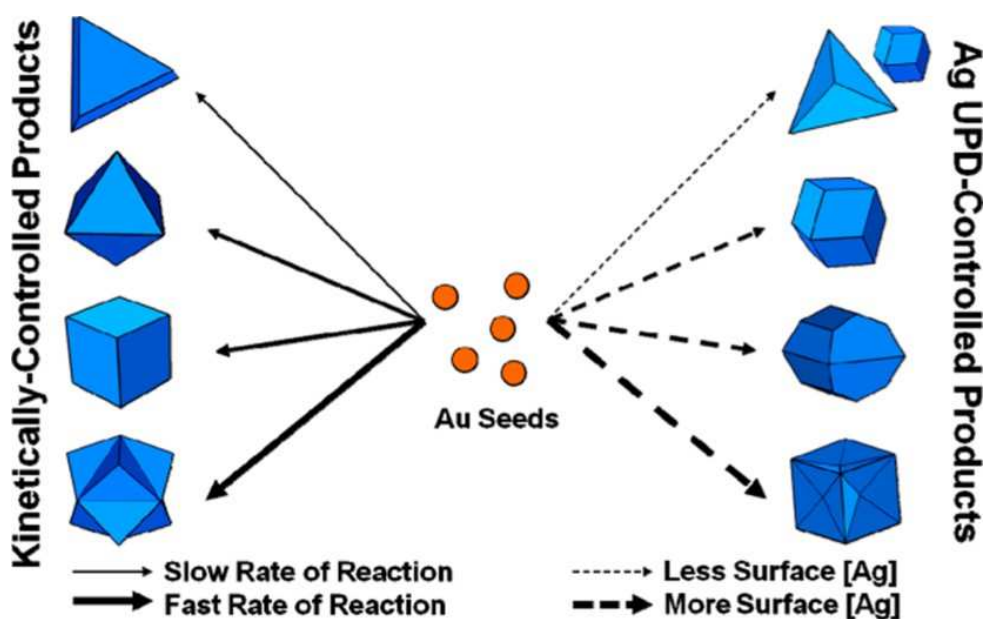


Fig. 30 General rules of shape-control in silver-assisted seed-mediated gold nanoparticles synthesis, where the shape of nanoparticles can be controlled simply by altering the reaction rate or the silver concentration. Ref. [18]

In addition to the four main components cited above, several additives could also play a major role determining the shape of nanoparticles in colloidal synthesis. Thus, the shape of the nanoparticle with additives corresponds to surface factor rather the kinetic effects allowed by adjusting the solution composition. Indeed, introducing additives results into a surface change of the nanoparticles upon growth, which favors selective growth. There are various structure directing agents including complexes ($W(CO)_6$), reactive gas molecules (O_2 , H_2 , NO , etc.) and metal ions (Ag^+ , Cu^{2+} , Fe^{3+} , Co^+). Metal ions addition was largely investigated in SMG process. As an example, by adding Ag^+ ions, the shapes of Platine nanoparticles changes from cube, cuboctahedron, and octahedron with increased Ag^+ concentration (**Fig. 31**). Indeed, higher-index surfaces are obtained in the presence of Ag^+ ions. Then, a stabilization of these high-index facets succeeds by increasing Ag^+ amount in the growth solution.[18] Then, a preferential

deposition of Ag^+ occurs on the sites with higher coordination number with respect to Pt, such as kinks and step edges. [19]

Precisely, Ag^+ ions directed a crystal growth rate along the $\langle 100 \rangle$ direction by preferentially adsorbing on more active $\{100\}$ surfaces of Pt nanoparticles. [20]

Consequently, as the seeded growth is combined with kinetically controlled overgrowth and selective etching, various morphologies can be produced such as cubes, hexagons, triangles, multi-pods, and highly-branched dendrites. [21],[22]

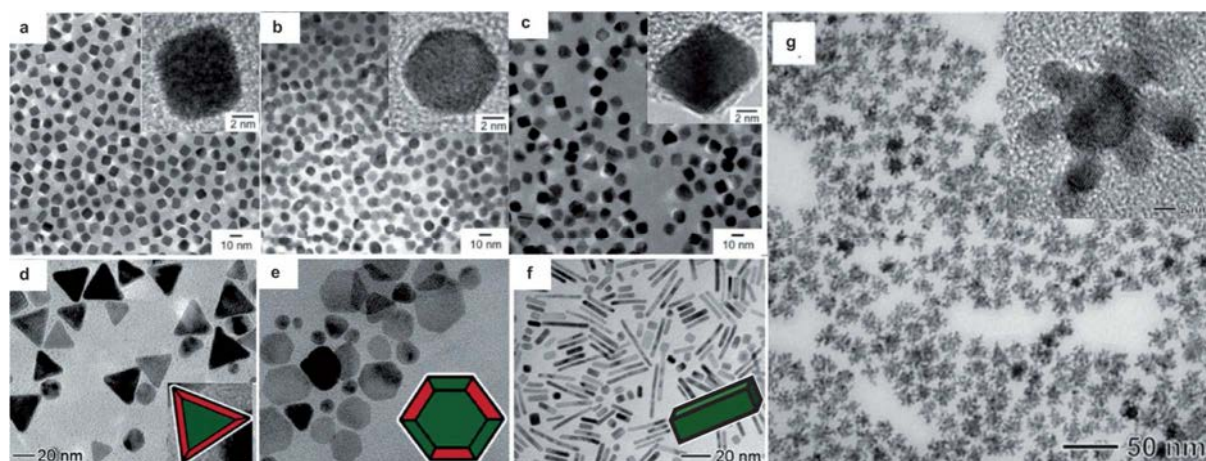


Fig. 31 TEM images of shape controlled Pt nanoparticles: a) Pt cubes, b) Pt cuboctahedra, c) Pt octahedra, d) Pd triangular plates, e) Pd hexagonal plates, f) Pd nanobars, and g) Pd-Pt bimetallic nanodendrites. Adapted from ref. 21.

3.3 Development of shape-controlled synthesis of gold nanoparticles

Since the El-Sayed group has demonstrated shape controlling of Pt nanoparticles toward various shapes (cube, tetrahedron, octahedron, etc.), many studies investigated the role of surfactants in shape-controlled synthesis of metallic nanoparticles. [23] The idea is to control the surface energy of crystal facets of metal nanocrystals to produce a specific shape by adjusting the interactions of metal surfaces and capping agents. Therefore, the selection of the capping agent is crucial and its metal and solution composition dependent. As an example, PVP can interact strongly to the $\{100\}$ direction of metal atoms, which changes both the surface free energies of crystal facets and the relative growth rates. This bounding of PVP to $\{100\}$ facets of metal atoms leads to a slower growth rate and then to the formation of triangles, tetrahedron and octahedron shapes.

Nevertheless, the bounding of PVP of random chains to $\{100\}$ facets results in a faster kinetics of the reaction, which leads to a higher growth rate and giving rise to the formation of nanocubes

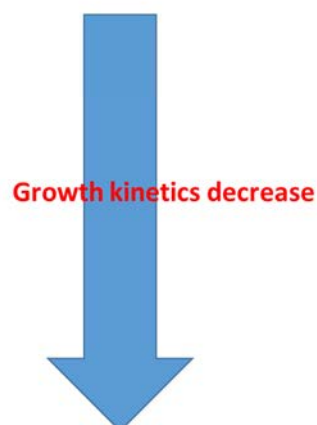
Based on the SMG strategy given in details in the last section and according to the role of capping agent highlighted by the example of PVP, we demonstrate here the possibility to transform the cube shape synthesized in chapter 2 into other morphologies. It was emphasized in chapter 2 that we used experimental conditions which yielded gold nanocubes meaning that we selected factors that allow fast nucleation and growth mechanism. This condition is necessary to elaborate the cubic nanostructure as seen in [Fig. 30](#). In particular, the synthesis of monodisperse gold nanocubes has been achieved by the combination of the five components including acetone as solvent for PMMA, ethanol as solvent of gold precursor, NaAuCl₄ as metal precursor, high concentration of gold precursor, and high evaporation rate of solvents. In order to control the morphology of gold nanostructures generated after the seed formation, we tried to kinetically change the synthesis growth rate.

Thus, the same synthesis method used in chapter 2 [24], is also followed in the present chapter to achieve shape control. However, we selected 100 mM of gold precursor and 5000 rpm of spin-coating speed and silicon wafer is still Arsenic-doped for next experiments. Thus, these parameters are fixed and the change of the solution composition will be our approach to change the final shape of GNP. Herein, we did several combinations of the PMMA/gold precursor dispersion in order to vary the growth rate of GNPs. These combinations are summarized in [Table 3](#) to provide an evidence that the three main parameters including the precursor molecule, the solvents of PMMA and gold precursor, rule the strategy used.

Table 3 Combinations of the three solution components (solvent, non-solvent and precursor) for controlling the shape of GNPs.

Gold precursor molecule	PMMA solvent	Precursor solvent
NaAuCl ₄ KAuCl ₄ HAuCl ₄	Acetone MIBK	Ethanol Isopropanol

NaAuCl₄/acetone/ethanol
 NaAuCl₄/acetone/isopropanol
 NaAuCl₄/MIBK/ethanol
 NaAuCl₄/MIBK/isopropanol
 HAuCl₄/acetone/ethanol
 HAuCl₄/acetone/isopropanol
 HAuCl₄/MIBK/ethanol
 HAuCl₄/MIBK/isopropanol
 KAuCl₄/acetone/ethanol
 KAuCl₄/acetone/isopropanol
 KAuCl₄/MIBK/ethanol
 KAuCl₄/MIBK/isopropanol



Each dispersion has its own volatility, which corresponds the sum of both volatility values of solvents of PMMA and gold precursor. From there, it can be expected that faster reduction and growth rate for dispersions having higher volatility, due to the reduction of Au³⁺, will occur faster if the solvents evaporate faster. To elucidate the effect of the volatility and validate our expectation about the growth rate and its effect on shape control, we will separately study the role of the three components cited in [Table 3](#).

3.3.1 Understanding the role of PMMA solvent (polymer solvent)

In chapter 2, it was explained based on previous studies of our groups that PMMA solvent plays a crucial role in the synthesis mechanism. Using acetone it allowed us to generate nanocubes. Thus, acetone evaporates rapidly and accelerates the growth rate as established earlier. Therefore, to obtain another morphology, we need to replace the acetone by a less hydrophilic and less volatile solvent to kinetically decrease the formation rate of GNPs. Starting from this point, we replaced acetone by MIBK.

[Fig. 32](#) shows samples prepared using the following conditions: same spin-coating parameters (speed 5000 rpm), same gold precursor (NaAuCl₄) and same solvent for gold precursor. As a result of changing the PMMA solvent, we obtained GNC and gold nanorectangles (GNRs). To consolidate the findings further, we completed this study with SEM as shown in [Fig. 33](#).

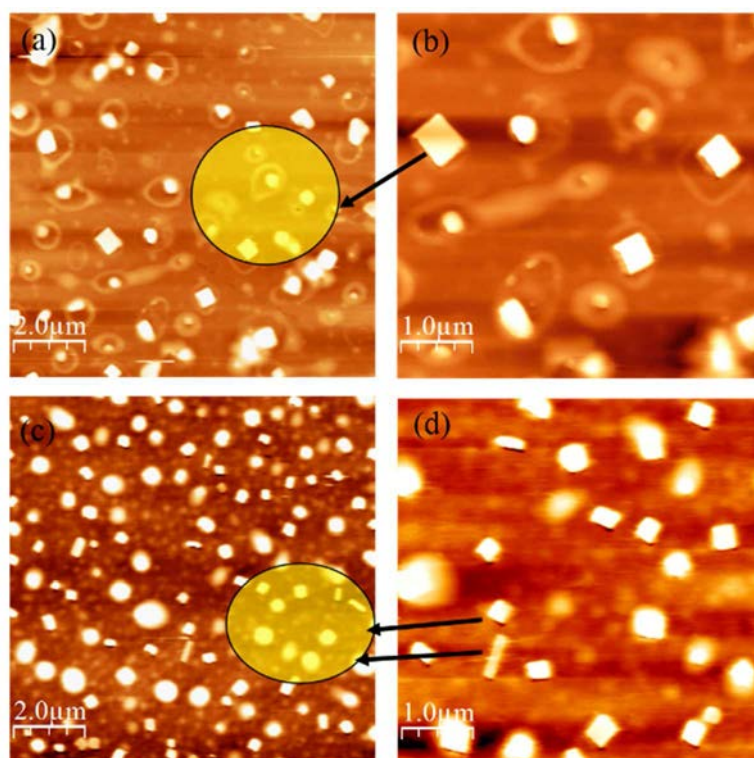


Fig. 32 AFM images of 100 mM gold precursor ($\text{NaAuCl}_4 \cdot 2\text{H}_2\text{O}$) in different PMMA solvents; in acetone (a, b) and in MIBK (c, d). Images taken in contact mode at same spin coating parameters and different scan sizes. (5 and 10 μm).

Referring to SEM images in Fig. 33 (a & b), we can see that sample prepared with MIBK solvent produces GNCs and GNRs as shown in the AFM images in Fig. 32 (c & d). Moreover, we obtained uniform GNCs as seen in Fig. 33 c. Following this solvent adjustment, we found that for the dispersion of NaAuCl_4 dissolved in ethanol, acetone is the suitable solvent to get single shape, which is cubic in this case. In order to obtain monodisperse GNCs (Fig. 33 d), acetone is used as PMMA solvent and ethanol as a solvent for sodium gold precursor. The formation of rectangular shapes might be attributed to the formation of PMMA micelles of different sizes because of the slow evaporation rate of MIBK that leads to the aggregation of some micelles on silicon surface. An excess of Au^{3+} ions in these micelles could provide further growth of gold nanocrystals in one direction, which results in GNRs formation. [25] Therefore it is established that the concentration of gold precursor is not enough to form so many rectangles. Further works on tuning Au^{3+} concentration and using a third solvent for PMMA are necessary to control the formation of monodispersed GNRs. One can see the formation of larger size of GNPs in the case of MIBK, in relation to the formation of bigger micelles of PMMA is due to slower evaporation rate of MIBK as described above. MIBK also allowed obtaining sharp nanocubes in comparison to the ones formed with acetone. This result can be

attributed to the slower rate of nucleation and growth of the nanocubes resulting from the slower evaporation of MIBK, which could generate more crystallized nanostructures.

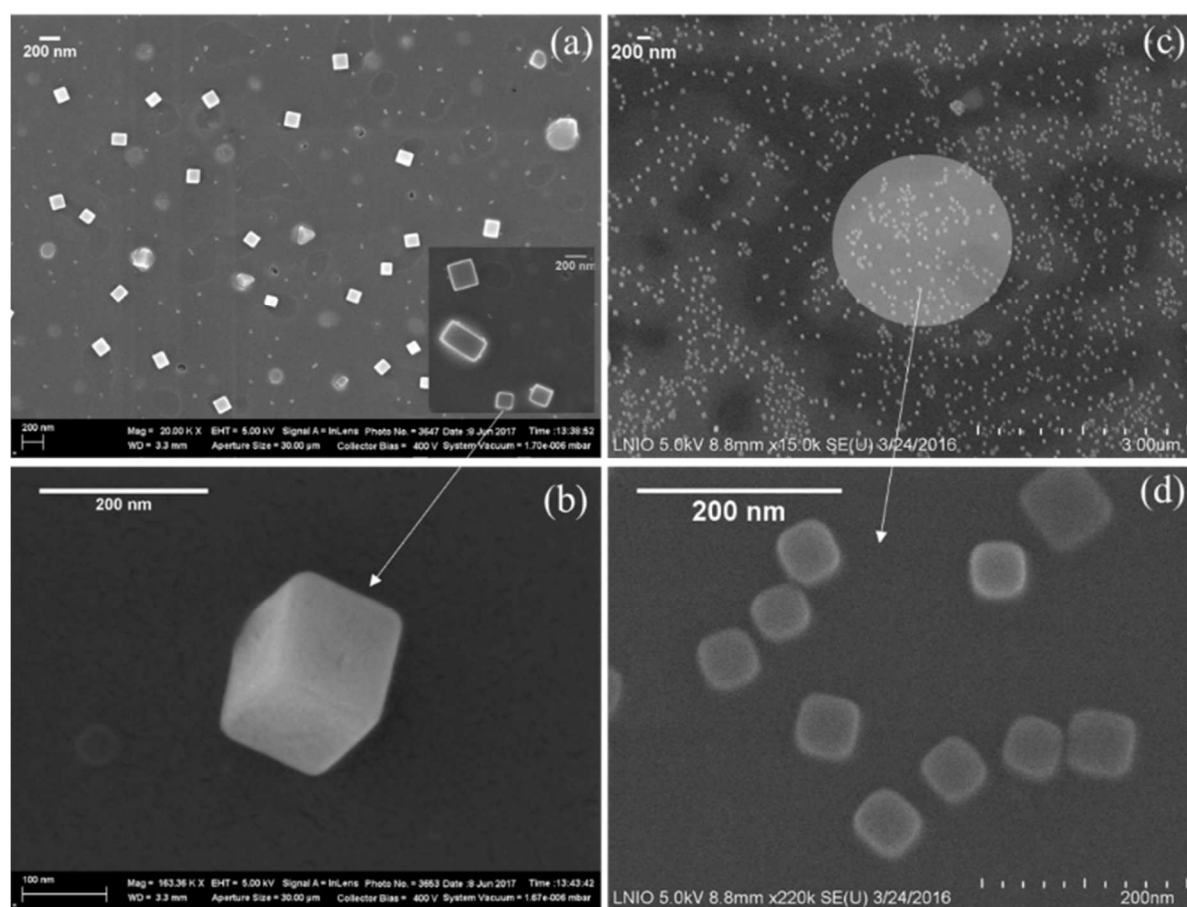


Fig. 33 SEM images for 100 mM gold precursor ($\text{NaAuCl}_4 \cdot 2\text{H}_2\text{O}$ /ethanol dispersion) in different PMMA solvents; (a) & (b) sample prepared with MIBK. The insert in (a) corresponds to small scan size images of the same sample and (b) corresponds also to the same sample observed with high magnification in order to observe a single nanocube. (c) and (d) samples prepared with acetone.

Then the role of PMMA solvent was studied using another precursor molecule (HAuCl_4). One can see in Fig. 34 the same behavior as in Fig. 33. Mainly, hexagonal gold nanoparticles (HGNs) were obtained when NaAuCl_4 is replaced by HAuCl_4 . This last molecule should decrease the pH of the PMMA/precursor dispersion and allow upon spin-coating, the reduction of lower number of Au^{3+} leading to slower nucleation and growth mechanism. This kinetically slower mechanism led to the formation of HGNs instead of GNCs since the hexagonal morphology requires slower reaction rate. Smaller size and sharp GNPs were obtained with MIBK due to the lower evaporation rate of MIBK that induces as described for Fig. 33. It is worthy to note that some nanotriangles are observed with MIBK solvents in Fig. 34 b, which can be related to an excess of Au^{3+} ions in some PMMA micelles on the surface of silicon. Seed mediated growth method showed the possibility to transform hexagons or octahedrons to

nanotriangles by increasing the gold precursor concentration until a specific value. [26] From this section, we can conclude that $\text{NaAuCl}_4/\text{acetone}/\text{ethanol}$ combination generates monodisperse nanocubes. However, $\text{HAuCl}_4/\text{acetone}/\text{ethanol}$ combination generates nanohexagons. Indeed, changing the PMMA solvent wasn't crucial for shape control. Nevertheless, it is helpful for controlling the size, number and crystallinity of the nanoparticles.

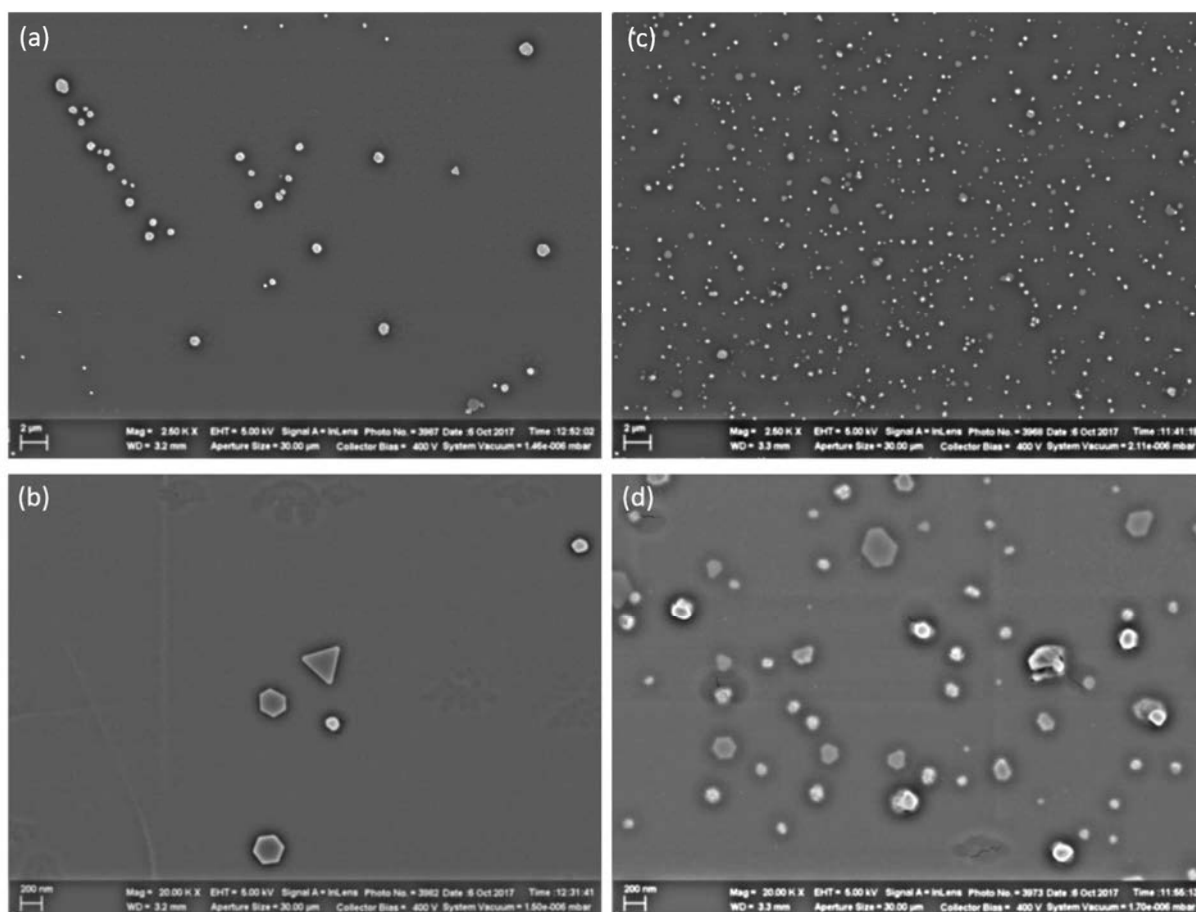


Fig. 34 SEM images for 100 mM gold precursor ($\text{HAuCl}_4 \cdot 2\text{H}_2\text{O}/\text{ethanol}$) in different PMMA solvents; (a) & (b) sample prepared with MIBK observed by two different magnifications. (c) and (d) sample prepared with acetone.

3.3.2 Understanding the role of gold precursor solvent (polymer non-solvent)

Changing the molecule precursor in Fig. 34 allowed us to better understand the role of PMMA solvent in determining the final size, shape and density of GNPs on the surface of the sample. Therefore, further experiments were done to understand the role of the precursor solvent, for both of the two precursor molecules used before (NaAuCl_4 and HAuCl_4), on the synthesis process. To make it possible, we fixed the spin-coating parameters, the PMMA solvent and molecule precursor and we only changed the precursor solvent. In Fig. 35, using NaAuCl_4 as

precursor led to the formation of nanocubes as shown in Fig. 33. On the other hand, isopropanol that evaporates slower than ethanol generated larger nanocubes and nanorectangles. As expected, isopropanol should retardate the growth of GNCs which must be formed by NaAuCl₄/acetone combination. This slowness in the growth rate resulted in the formation of polydispersed nanoparticles divided into nanocubes and mainly nanorectangles. When isopropanol remains a long time inside PMMA micelles, they tend to attach and aggregate into larger ones containing higher Au³⁺ concentration. Consequently, the combination of a high amount of Au³⁺ ions with the slow rate of growth gives rise to the formation of bigger nanoparticles and a morphology that requires slow reaction rate, which is rectangular in this case.

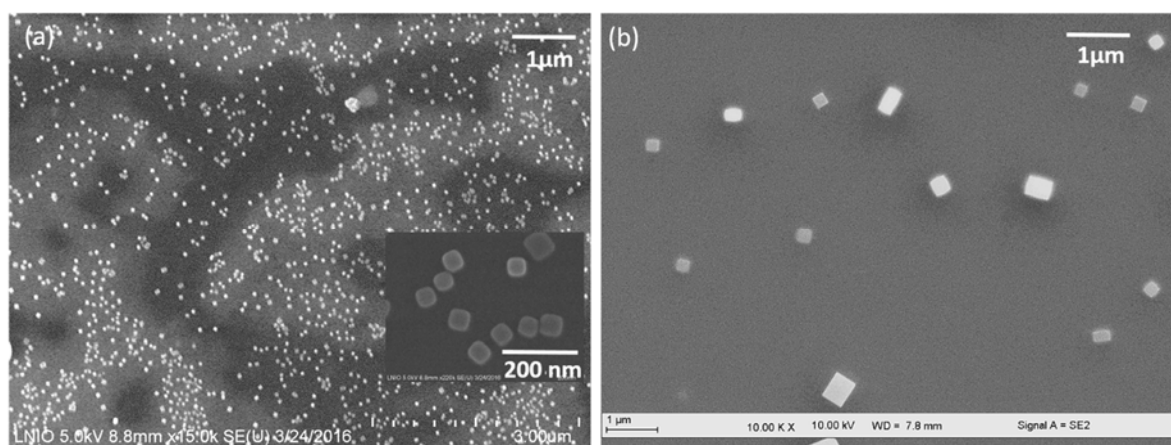


Fig. 35 SEM images for 100 mM gold precursor (NaAuCl₄.2H₂O/acetone) in two different precursor solvents; (a) sample prepared with ethanol. (b) sample prepared with isopropanol.

Similarly, the same experiments were repeated using HAuCl₄ as molecule in order to slow further the reaction rate. Fig. 36 shows mainly nanohexagons for the sample prepared with isopropanol. However, nanohexagons and polygons are observed using ethanol. For both solvents, we don't see a particular control of shape and size even a major nanostructure is observed for a given sample which is hexagonal. However, Isopropanol is suitable to obtain monodisperse nanohexagons. Once again changing the precursor molecule seems crucial.

To conclude about PMMA solvent effect, the precursor solvent could be a mean to change the size and number of nanoparticles. It is interesting to note that PMMA solvent didn't affect strongly the shape in comparison with precursor solvent. We suggest that isopropanol-PMMA interaction is weaker than that of ethanol-PMMA in solution and after spin-coating. Therefore, a higher polydispersity for PMMA micelles and then gold nanostructures could be generated by isopropanol or another solvent of higher molecular weight.

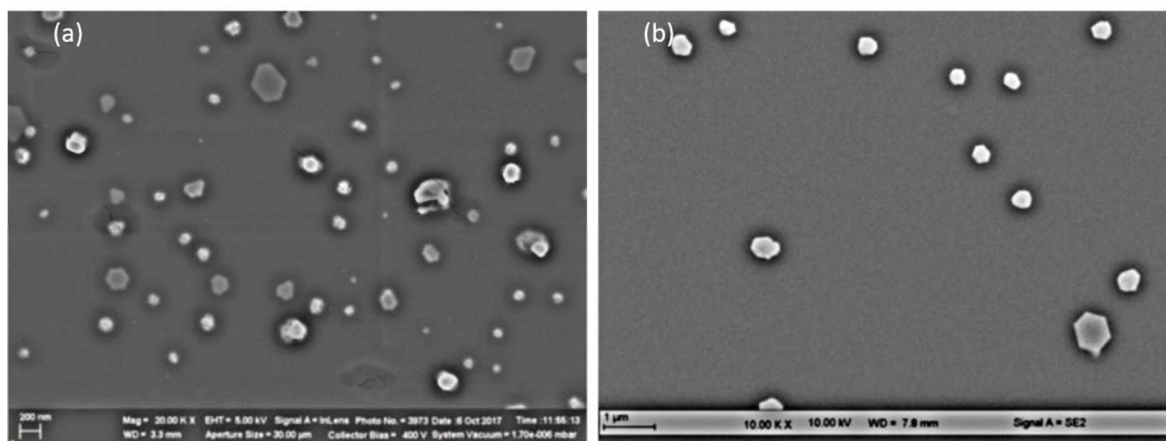


Fig. 36 SEM images for 100 mM gold precursor ($\text{HAuCl}_4 \cdot 2\text{H}_2\text{O}$ /acetone) in two different precursor solvents; (a) sample prepared with ethanol. (b) sample prepared with isopropanol.

3.3.3 Role of the gold precursor molecule

We clearly demonstrated the interest to change the precursor type on the shape of GNPs. Whatever the solvent/non-solvent combination, the precursor molecule was the component that defined the shape. It was shown that NaAuCl_4 generates nanocubes and HAuCl_4 generates mainly hexagons (or octahedrons). Until now, we achieved the control of nanocubes fabrication (size and shape). Chapter 2 was reserved for this nanostructure morphology. Still, further studies are required to achieve the formation of monodispersed nanohexagons. We also need to explore the possibility to produce other morphologies. Herein, we investigate the role of the precursor (pH, molecular weight, counter-ion, etc.) on the synthesis results. As done before, we changed the precursor keeping the same all the other components (solvent, non-solvent, spin-coating parameters, silicon type). Aiming to fabricate nanotriangular shape, we selected the acetone/isopropanol combination for two reasons. First, acetone is suitable for low polydispersity and isopropanol generated more of triangles than ethanol as seen in Fig. 36. Fig. 37 reveals the formation of nanoprisms when HAuCl_4 is replaced by KAuCl_4 . This result confirms that the precursor molecule plays the major role in controlling the shape. The three precursors used differ by the molecular weight and the counter- ion of AuCl_4^- . We suggest that this counter-ion plays an important role in the synthesis mechanism. It could be compared to the additive effect usually used in seed mediated growth methods to control the NPs shape. As reported in the introduction section, adding Ag^+ ions to the synthesis reaction medium allows to fabricate different morphologies of Pt nanoparticles, as seen in Fig. 31. Accordingly, Na^+ and K^+ could deposit on Au seeds and drive the growth. Since K^+ ion is larger Na^+ (Na^+ is more electropositive), the interaction between Na^+ and Au seeds will be stronger, which could result

in a faster growth rate in comparison to K^+ . The presence of larger ions on the surface of Au nanoparticles could limit the growth kinetics. Therefore, the nanocubic shape was obtained with $NaAuCl_4$. However, the nanoprism structure, that requires both a slow reduction of Au^{3+} and growth rate of nanoparticles, was produced using $KAuCl_4$. This ion-assisted seed-mediated growth allows for the average edge length of the octahedral (hexagonal or prism) to be independently controlled. For example, Ag^+ has been used in seed-mediated methods to stabilize high-index facets through an under potential deposition mechanism (UPD). [27] Thus, it is suggested that a high concentration of Na^+ or K^+ stabilizes the $\{111\}$ facets of the nanocrystals through UPD, while the rate of Au^{3+} reduction controls the dimensions of the nanostructures. On this basis, different combinations of dispersions have been done to change the synthesis reaction rate in order to produce monodispersed nanohexagons and nanotriangles.

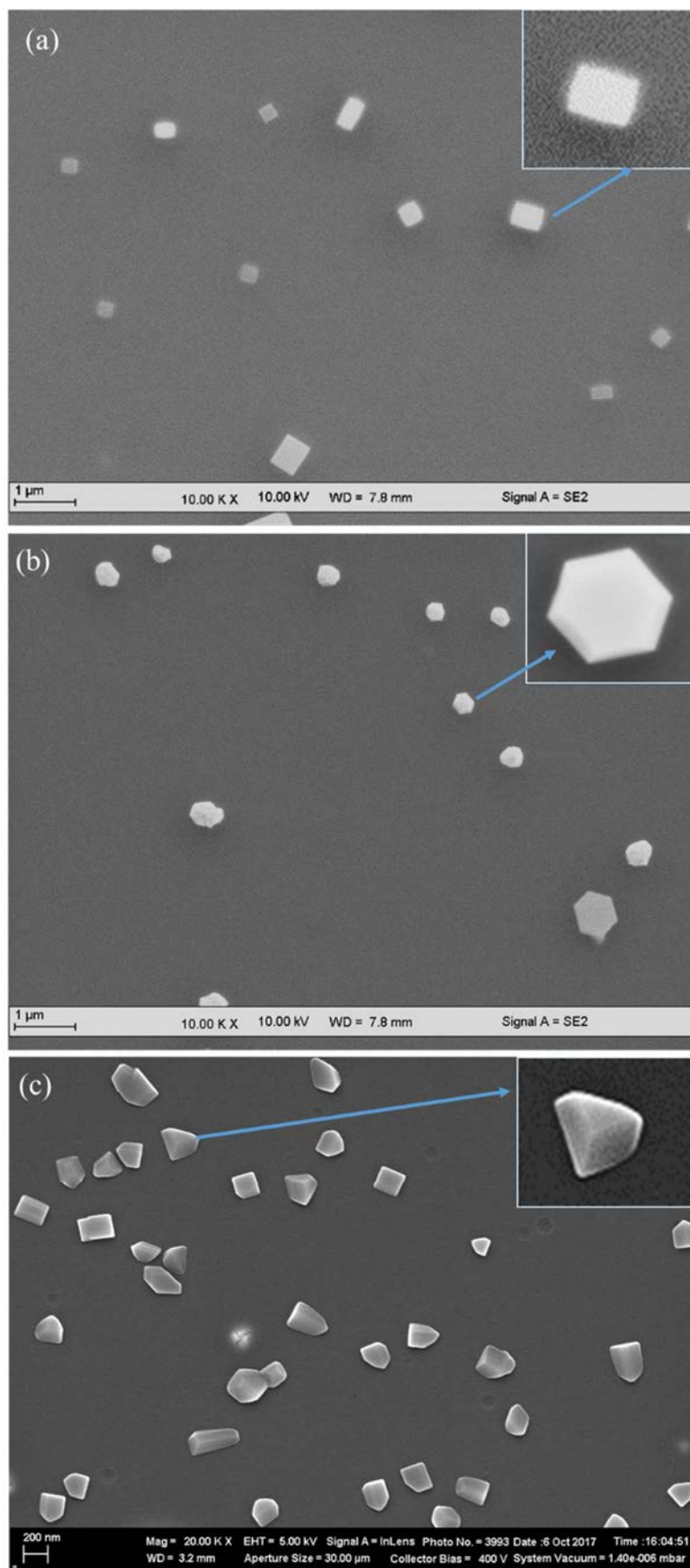
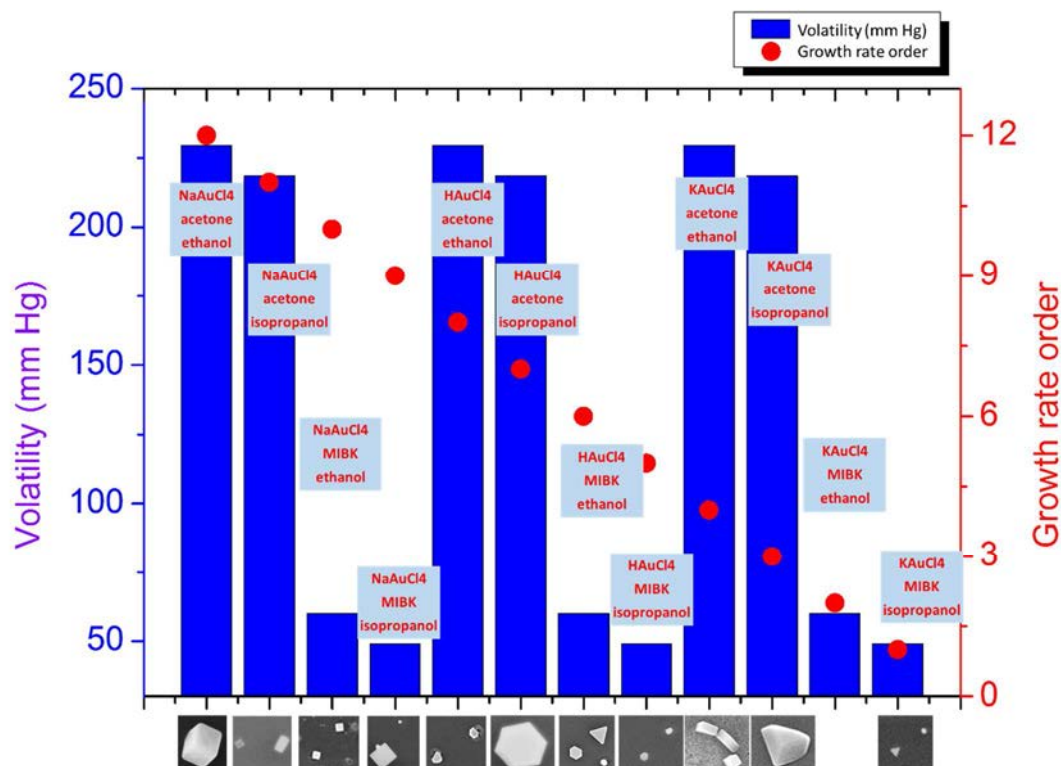


Fig. 37 SEM images for samples prepared with acetone (PMMA solvent)/isopropanol (precursor solvent) combination with three different precursor molecules; (a) NaAuCl_4 , (b) HAuCl_4 and (c) KAuCl_4 .

In **Scheme 4**, we sum-up all the studies done in this chapter to vary the synthesis conditions.



Scheme 4 Combinations of the three solution components (solvent, non-solvent and precursor) in order to vary the growth rate through changing the volatility of solutions (effect of solvents) and pH (effect of precursor molecule type).

In comparison to the conventional surfactant-based protocols which change the product of the synthesis by varying the reaction rate, the obtained nanostructures cannot be explained in terms of those proposed for surfactant-based growth modes where surfactants, surface diffusion, and/or collision patterns are used to transform the reaction product. However, we propose a nucleation and growth pathway that relies on the formation of a space charge region around each seed consisting of a layer of ions (Na^+ or K^+), where the whole layer is dependent on the facets expressed by the seed, the rate at which the reduced ions are being deposited, and the pH of the solution. This chapter reveals the rich nature of surfactant-free synthesis as well as the utility of the substrate-based platform in defining growth strategies.

3.4 Improving the SERS enhancement through shape control

In order to evaluate the different gold nanostructures as sensors, we performed SERS measurements with 10^{-5} M of pyridine on four samples showing different morphologies of

nanoparticles. The SEM images of these samples and their corresponding absorption spectra are illustrated in Fig. 38.

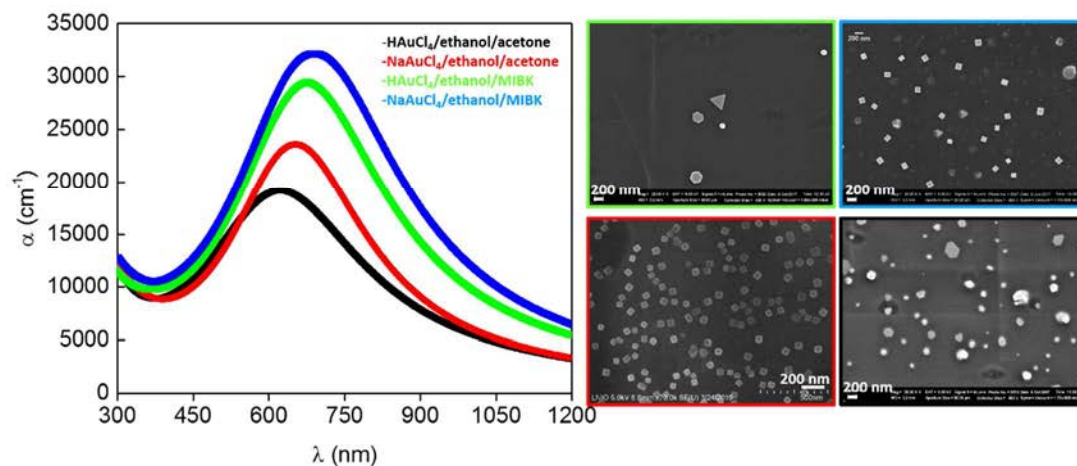


Fig. 38 Absorption spectra of gold nanoparticles prepared with different experimental conditions. (Black spectrum) polydispersed nanohexagons, (red spectrum) monodispersed nanocubes, (green spectrum) nanohexagons and nanotriangles and (blue spectrum) monodispersed sharp nanocubes.

Polydispersed nanohexagons (black curve) exhibit the most blue shifted absorption peak and the closest to the excitation wavelength (633 nm). The red shift observed for the other samples is due to the high density of nanoparticles for the sample of monodispersed nanocubes (red curve) and because of the increase in the size and the decrease in the density of nanoparticles for the samples of nanohexagons, nanotriangles and monodispersed sharp nanocubes (green and blue curves).

Fig. 39 shows the best Raman enhancement with gold nanocubes. We can explain this higher sensitivity by both the high density of nanocubes on the substrate and the SPR band close to the laser excitation wavelength. The SERS intensity for the other samples decreases continuously with decreasing the number of nanoparticles. Therefore, the sample of the sharp nanocubes (blue curve) exhibits higher enhancement than that of nanohexagons (green curve) even its SPR band is the most shifted to the laser wavelength. Because of the difference in size and density of NPs in the samples, we can just compare between the two samples having the same cubic shape (blue and red curves). As reported before, the higher sensitivity of monodispersed GNCs (red curve) in comparison to sharp ones (blue curve) is due to the higher number of GNCs on the surface, which results in the presence of hotspots relevant for SERS. To be able to study the effect of shape on the sensitivity of the obtained samples, it's necessary, for the future, to compare the substrates having the same density of nanoparticles on the surface. According to

all results described above, each experimental combination allowing a particular shape has its own size and density of NPs. Therefore, further experiments are required to control the interparticles gap. We propose to change the spin coating speed in order to determine for each sample the critical speed value that allows to obtain a gap distance comparable with the other samples. In a previous study [28] and in chapter 2, we showed that increasing the spin coating speed led to a decrease in the size distribution and the gap between nanoparticles. Thus, we need to investigate this effect on the shape control as a perspective work.

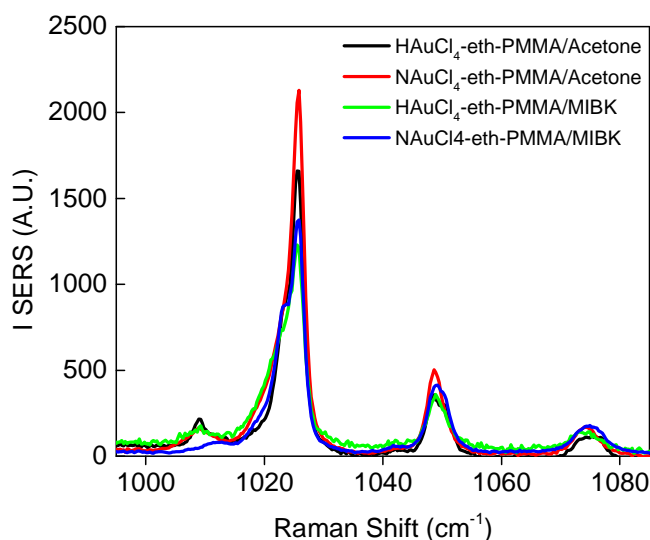


Fig. 39 SERS and Raman spectra of Pyridine for samples shown in Fig. 38. All these samples have the same coating parameters and same gold precursor concentration (100 mM). 10 μ l drop of pyridine (10^{-5} M for SERS and 1 M for Raman)

As assessed in chapter 2, chemical Raman enhancement can also be expected for the four studied substrates because of the SERS vibrational frequency shifted from Raman ones. These shifts in the pyridine internal modes is due to the charge transfer complexes through the N-end interaction between the metal and pyridine. [29],[30]

3.5 Conclusion

We have demonstrated shape-controlled growth of gold nanocrystals by a substrate-strategy. We found that varying the reaction kinetics allowed different growth modes of gold nanoparticles. In this route, the silicon electrons bounded to the counter ions (H^+ , Na^+ and K^+) of the gold precursor molecule used, serve as heterogeneous nucleation for gold nanocrystals. These anisotropies on the surface of silicon results in anisotropies in the kinetic growth associated with (i) Au atoms arriving preferentially to the base of nucleation site from an adjacent collection area, (ii) higher atom diffusion rates on $\{111\}$ facets than on $\{100\}$ facets,

and (iii) the various Ehrlich–Schwoebel barriers [31] which inhibit the atom motion between facets. These anisotropies lead to the non-equilibrium steady state strongly dependent on whether the reaction is carried out in a regime of slow, moderate, or fast kinetics. Slow kinetics was achieved by KAuCl_4 combination and gave rise to triangular gold nanoprism generated through epitaxial deposition on just a small portion of a single $\{100\}$ Au facet followed by the propagation of a rapid growth front away from the seed. Moderate kinetics allowed by HAuCl_4 resulted in hexagonal geometry realized through layer-by-layer deposition of Au on all $\{100\}$ equivalent seed facets followed by the overgrowth of all remaining facets. Fast kinetics allowed by NaAuCl_4 produced cubic and rectangular morphologies, where the overgrowth more closely follows the topography of the underlying seed. Further experimental studies are necessary in the future to better control the monodispersity of the obtained geometries as done in chapter 2 for gold nanocubes. Produced in high yield from a simple process, the so-formed nanohexagons and nanoprisms present the opportunity to form photonic surfaces for catalytic, sensing and photovoltaic applications. The optical properties and the sensing of pyridine covered different shapes of gold nanostructures through SERS were also reported.

3.6 References

- [1] Wang, Z. L. (1998). Structural analysis of self-assembling nanocrystal superlattices. *Advanced Materials*, 10(1), 13-30.
- [2] Peng, X., Manna, L., Yang, W., Wickham, J., Scher, E., Kadavanich, A., & Alivisatos, A. P. (2000). Shape control of CdSe nanocrystals. *Nature*, 404(6773), 59-61.
- [3] Nikoobakht, B., Wang, Z. L., & El-Sayed, M. A. (2000). Self-assembly of gold nanorods. *The Journal of Physical Chemistry B*, 104(36), 8635-8640.
- [4] Yu, Y. Y., Chang, S. S., Lee, C. L., & Wang, C. C. (1997). Gold nanorods: electrochemical synthesis and optical properties. *The Journal of Physical Chemistry B*, 101(34), 6661-6664.
- [5] Xia, Y., Xiong, Y., Lim, B., & Skrabalak, S. E. (2009). Shape-controlled synthesis of metal nanocrystals: Simple chemistry meets complex physics?. *Angewandte Chemie International Edition*, 48(1), 60-103.
- [6] Somorjai, G. A., & Park, J. Y. (2008). Molecular factors of catalytic selectivity. *Angewandte Chemie International Edition*, 47(48), 9212-9228.
- [7] Lohse, S. E., & Murphy, C. J. (2013). The quest for shape control: a history of gold nanorod synthesis. *Chem. Mater*, 25(8), 1250-1261.
- [8] Abid, J. P., Wark, A. W., Brevet, P. F., & Girault, H. H. (2002). Preparation of silver nanoparticles in solution from a silver salt by laser irradiation. *Chemical Communications*, (7), 792-793.

- [9] Tan, L. H., Yue, Y., Satyavolu, N. S. R., Ali, A. S., Wang, Z., Wu, Y., & Lu, Y. (2015). Mechanistic insight into DNA-guided control of nanoparticle morphologies. *Journal of the American Chemical Society*, 137(45), 14456-14464.
- [10] Khodashenas, B., & Ghorbani, H. R. (2014). Synthesis of copper nanoparticles: an overview of the various methods. *Korean Journal of Chemical Engineering*, 31(7), 1105-1109.
- [11] Nikoobakht, B., & El-Sayed, M. A. (2001). Evidence for bilayer assembly of cationic surfactants on the surface of gold nanorods. *Langmuir*, 17(20), 6368-6374.
- [12] Daniel, M. C., & Astruc, D. (2004). Gold nanoparticles: assembly, supramolecular chemistry, quantum-size-related properties, and applications toward biology, catalysis, and nanotechnology. *Chemical reviews*, 104(1), 293-346.
- [13] An, K., & Somorjai, G. A. (2012). Size and shape control of metal nanoparticles for reaction selectivity in catalysis. *ChemCatChem*, 4(10), 1512-1524.
- [14] Gu, H., Yang, Z., Gao, J., Chang, C. K., & Xu, B. (2005). Heterodimers of nanoparticles: formation at a liquid– liquid interface and particle-specific surface modification by functional molecules. *Journal of the American Chemical Society*, 127(1), 34-35.
- [15] Sriram, M., Zong, K., Vivekchand, S. R. C., & Gooding, J. J. (2015). Single nanoparticle plasmonic sensors. *Sensors*, 15(10), 25774-25792.
- [16] Bullen, C., Zijlstra, P., Bakker, E., Gu, M., & Raston, C. (2011). Chemical kinetics of gold nanorod growth in aqueous CTAB solutions. *Crystal Growth & Design*, 11(8), 3375-3380.
- [17] Xu, X., Zhao, Y., Xue, X., Huo, S., Chen, F., Zou, G., & Liang, X. J. (2014). Seedless synthesis of high aspect ratio gold nanorods with high yield. *Journal of Materials Chemistry A*, 2(10), 3528-3535.
- [18] Langille, M. R., Personick, M. L., Zhang, J., & Mirkin, C. A. (2012). Defining rules for the shape evolution of gold nanoparticles. *Journal of the American Chemical Society*, 134(35), 14542-14554.
- [19] Personick, M. L., Langille, M. R., Zhang, J., & Mirkin, C. A. (2011). Shape control of gold nanoparticles by silver underpotential deposition. *Nano letters*, 11(8), 3394-3398.
- [20] Song, H., Kim, F., Connor, S., Somorjai, G. A., & Yang, P. (2005). Pt nanocrystals: shape control and langmuir– blodgett monolayer formation. *The Journal of Physical Chemistry B*, 109(1), 188-193.
- [21] Lim, B., Jiang, M., Camargo, P. H., Cho, E. C., Tao, J., Lu, X., ... & Xia, Y. (2009). Pd-Pt bimetallic nanodendrites with high activity for oxygen reduction. *science*, 324(5932), 1302-1305.
- [22] Herricks, T., Chen, J., & Xia, Y. (2004). Polyol synthesis of platinum nanoparticles: control of morphology with sodium nitrate. *Nano Letters*, 4(12), 2367-2371.
- [23] Ahmadi, T. S., Wang, Z. L., Green, T. C., Henglein, A., & El-Sayed, M. A. (1996). Shape-controlled synthesis of colloidal platinum nanoparticles. *SCIENCE-NEW YORK THEN WASHINGTON-*, 1924-1925.
- [24] Omar, R., Naciri, A. E., Jradi, S., Battie, Y., Toufaily, J., Mortada, H., & Akil, S. (2017). One-step synthesis of a monolayer of monodisperse gold nanocubes for SERS substrates. *Journal of Materials Chemistry C*.

- [25] Sau, T. K., & Murphy, C. J. (2004). Room temperature, high-yield synthesis of multiple shapes of gold nanoparticles in aqueous solution. *Journal of the American Chemical Society*, 126(28), 8648-8649.
- [26] Personick, M. L., Langille, M. R., Zhang, J., & Mirkin, C. A. (2011). Shape control of gold nanoparticles by silver underpotential deposition. *Nano letters*, 11(8), 3394-3398.
- [27] Liu, M., & Guyot-Sionnest, P. (2005). Mechanism of silver (I)-assisted growth of gold nanorods and bipyramids. *The Journal of Physical Chemistry B*, 109(47), 22192-22200.
- [28] Akil-Jradi, S., Jradi, S., Plain, J., Adam, P. M., Bijeon, J. L., Royer, P., & Bachelot, R. (2012). Micro/nanoporous polymer chips as templates for highly sensitive SERS sensors. *RSC Advances*, 2(20), 7837-7842.
- [29] Seo, D., Yoo, C. I., Park, J. C., Park, S. M., Ryu, S., & Song, H. (2008). Directed surface overgrowth and morphology control of polyhedral gold nanocrystals. *Angewandte Chemie*, 120(4), 775-779.
- [30] Elsayed, M. Y., Gouda, A. M., Ismaila, Y., & Swillam, M. A. (2017, February). Silver-decorated silicon nanowires array as surface-enhanced Raman scattering (SERS) substrate. In *Proc. of SPIE Vol* (Vol. 10112, pp. 1011224-1).
- [31] Gilroy, K. D., Hughes, R. A., & Neretina, S. (2014). Kinetically controlled nucleation of silver on surfactant-free gold seeds. *Journal of the American Chemical Society*, 136(43), 15337-15345.

4 Optical properties of self-assembled gold nanoparticles

4.1 Introduction

It is well known that the optical properties, such as the dielectric functions and the absorption coefficient of the metal nanoparticles (MNPs) and the surrounding material, play an important role in designing new applications in photonics, optoelectronics, and non-linear optics. [1]

Therefore, the knowledge of the effective dielectric function of nano-composite film is a crucial issue to design the optical devices. The optical properties of these MNPs are usually characterized by UV-VIS absorption spectroscopy, such as the surface plasmon resonance (SPR) of NPs which provides various information on the NP load, size, shape, and distribution. However, the optical characterization of the material is limited upon using this technique and it is blind to the elucidation of its refractive index.

In this chapter, we show that spectroscopic ellipsometry (SE) is a valuable tool to determine the complete optical properties of these composite layers. Ellipsometry is an indirect optical characterization tool which is based on the change of the polarization state of light after the reflection on the sample. [2] The stronger the interaction between the light and the material, the better measurements are obtained. [2-5]

Ellipsometry requires an appropriate modeling to determine simultaneously the film thickness and the dielectric constants. Recent works suggest that ellipsometry can be used to characterize nanomaterials [6-8]. Ellipsometry was previously used to monitor the growth of silver NPs on the surface [9], in polymer [10],[11], or in mesoporous silica matrices [12]. However, the classical effective medium theories, used to exploit ellipsometric data consider only the spheroidal NPs. [4]

This chapter describes a complete ellipsometric characterization of gold nanoparticles (GNPs) that were embedded in PMMA film. The thickness of the polymer film (PMMA) and the dielectric functions (real and imaginary parts) as well as the absorbance coefficient are obtained by modeling the ellipsometric measurements.

Based on our knowledge of the literature, no research works in literature concerning the optical properties of non-spherical shapes of MNPs in large spectral range (VIS-NIR) have been reported using the SE. Herein, we report a model that is based on two classical Lorentz oscillators to determine the optical responses of non-spherical GNPs (hexagonal, cubic and triangular). This model and the measuring strategy are discussed in details in the section below.

4.2 Ellipsometry technique

The Ellipsometry is an optical technique that is widely used for surface and thin film analysis. It is a fast and nondestructive technique that allows monitoring the film growth in real time. It is used in wide applications such as microelectronics, optoelectronics, photovoltaics, and chemistry etc. SE allows the determination of the optical constants over a broad spectral range and it is one of the most sensitive and precise tools for thin film thickness measurements. So, one can deduce the film thickness (d) and the optical properties of the target material. [13]

The main optical properties are: real (ϵ_r) and imaginary (ϵ_i) parts of the dielectric function, refractive index (n), extinction coefficient (k) and the absorption coefficient (α).

The measured parameters are called ellipsometric angles Ψ and Δ . The Ψ angle refers to amplitudes, whereas the Δ angle is the phase change of the ellipsometric ratio. These angles measure the change in the state of polarization of light after reflection on the sample. They depend on various parameters such as the thickness of the different layers of the sample, complex refractive index of each layer, wavelength and angle of incidence.

In addition, these angles are basically related to the ratio of the complex Fresnel reflection coefficients r_s and r_p , where r_p and r_s are the complex reflection coefficients of parallel and perpendicular polarization of light, respectively. Thereby, r_s is the reflection coefficient of the light polarized perpendicular to the plane of incidence and r_p is the reflection coefficient of the light polarized parallel to the plane of incidence. This is expressed by the following fundamental equation of ellipsometry, which describes a relationship between the ellipsometric angles (Ψ & Δ) of parallel and perpendicular polarization: [14],[15]

where,

$$\rho = \frac{r_p}{r_s} = \tan\Psi e^{i\Delta} \quad 0^\circ \leq \Delta \leq 360^\circ, (1)$$

and

$$\tan \Psi = \frac{|r_p|}{|r_s|} \quad 0^\circ \leq \Psi \leq 90^\circ. (2)$$

Ψ and Δ ellipsometric angles can be obtained using different ellipsometers such as rotating polarizer or analyzer ellipsometer. In our case we have used the UVISEL modulator photoelastic ellipsometer of Horiba. The schematic view of this spectroscopic ellipsometer is shown in Fig. 40.

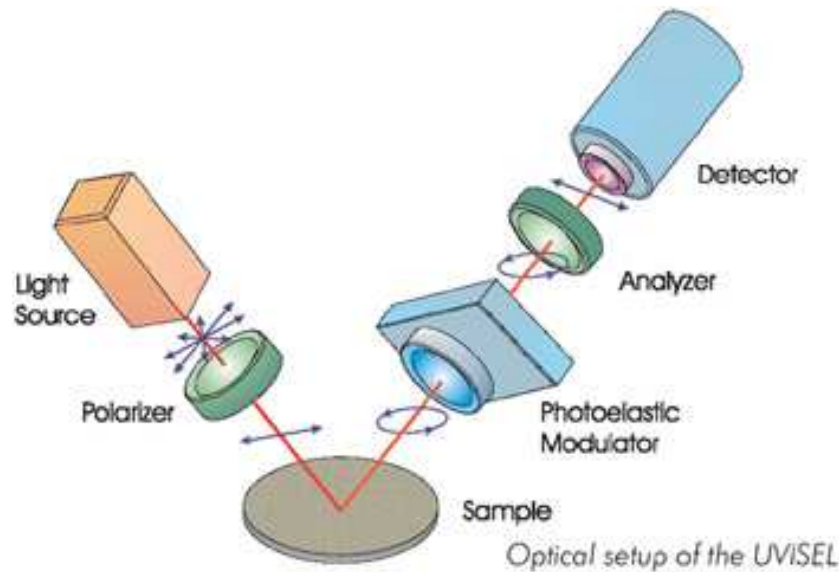


Fig. 40 Schematic view of the UVISEL spectroscopic ellipsometer.

The light source is a Xenon lamp that covers a large spectral range from 250 to 2100 nm. After passing through the first polarizer which establishes a linear polarization, the light reflects at an oblique angle (generally 70°) from the sample under study. The output head comprises a photoelastic modulator and an analyzing polarizer that resolves the polarization state of the reflected beam.

Both polarizers are fixed during the measurement while the photoelastic modulator is used to induce a modulated phase shift of the reflected beam. The light is analyzed by a grating monochromator that directs, sequentially, the light for each individual wavelength onto the detector. Two types of detectors are employed: photomultipliers for UV-VIS applications and InGaAs photodiodes for NIR applications.

Except for substrate sample, ellipsometry cannot directly evaluate the optical properties or the thickness of thin layers from measured Ψ and Δ ellipsometric angles. Data analysis using an optical model is required in order to determine the unknown parameters of samples (film thickness, optical constants, etc.). The data analysis procedure can be summarized in the following three steps:

1. First, an optical model must be constructed to describe the sample.
2. The second step concerns the theoretical calculation of Ψ and Δ which are derived from the optical model.
3. Third, the calculated Ψ and Δ values are compared with the measured ones, and the parameters of the optical model are fitted to find an optimal agreement. Finally when the optimal optical model is found, the unknown parameters are determined.

Therefore, the optical and structural properties of the targeted material are determined by a suitable modeling through the measurements of Ψ and Δ parameters. Fig. 41 presents an example of the measured ellipsometric angles as function of incident wavelength at 60° .

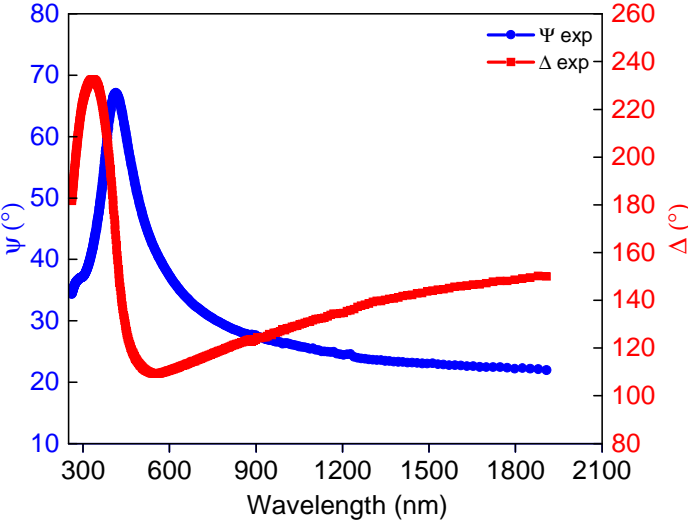


Fig. 41 Measurement of ellipsometric parameters of Ψ (blue curve) and Δ (red curve). The measurements are performed at an angle of incidence 60° on a silicon substrate coated with GNPs (40 mg of $\text{NaAuCl}_4/\text{MIBK/ethanol}$) at 10000 rpm.

These measurements are performed in air at room temperature in spectral range 250-2100 nm. The amplitude of oscillations observed in this figure depends mainly on the PMMA film thickness. These ellipsometry measurements are obtained from the sample given in Fig. 42. We notice that the measured ellipsometric parameters of all the used samples at an angle of incidence of 60° or 70° are introduced in the discussion part.

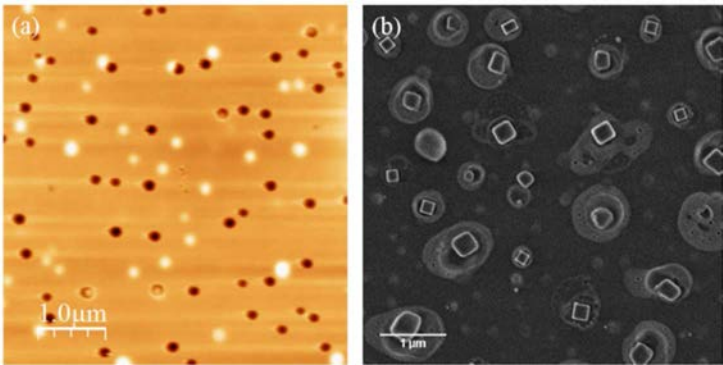


Fig. 42 (a) AFM image of GNPs loaded PMMA holes over a silicon substrate (image taken in contact mode). (b) SEM image showing clearly the GNPs inside the PMMA holes. The two samples are prepared according to the physio-chemical synthesis method that was introduced in chapter 2 (40 mg of $\text{NaAuCl}_4/\text{MIBK/ethanol}$ using 10000 rpm).

The AFM image shown in Fig. 42 (a) and SEM image in Fig. 42 (b) present two examples of the synthesized samples, where GNPs are embedded in PMMA film. Based on our fabricated samples, a physical model should take into account not only the PMMA film and the optical properties of the Si substrate but also the optical responses of the implanted GNPs.

4.2.1 Modeling

Different theoretical approaches have been developed to calculate the optical response from spherical and non-spherical metal nanoparticles, including the effective medium approximation theory (EMT) such as Maxwell-Garnet (MG) or Bruggeman theories.

Through EMT, it is possible to determine the presence of surface roughness or the volume fraction of inclusions (e.g. spherical NPs) within a host material. [4],[16],[17]

MG gives a realistic description of a medium when the volume fraction of the spherical inclusions, weakly interacting with each other, is smaller than that of the host material. This theory is highly used to describe the optical properties of metallic nanoparticles which are embedded in a host medium. Thus, the dielectric function, the refractive index and the absorption of a composite layer can be calculated. However, the shape of the particle cannot be considered in this theory. [16],[17]

Recent improvement and modifications in this model are only applicable on highly dispersed spheroidal NPs. [16] Therefore, the MG model is inappropriate to our samples with different shapes shown as an example in Fig. 42.

Unlike the MG theory, the Bruggeman effective medium approximation (BEMA) studies the optical properties of the composite medium where the inclusions and the host material have similar roles in the effective medium. [13],[18] This is not the case in our samples, therefore BEMA can't be applied.

In contrast to EMT, the Boundary Elementary Method (BEM) can be suitable to carry out the optical analysis. However, the presence of the shape distribution in our samples makes this model more difficult to be applied for the determination of the optical responses of these complex systems. In addition, it takes more time to be analyzed. [19] BEM is more adaptable when the shape distribution is not considered as it was applied in the second chapter on gold nanocubes (GNCs) of 65 nm length side and on dimer of GNCs being apart at 10 nm.

After testing various models, we have found the model given in Fig. 43 and Scheme 2 (chapter 2) is the most suitable one for modeling our samples.

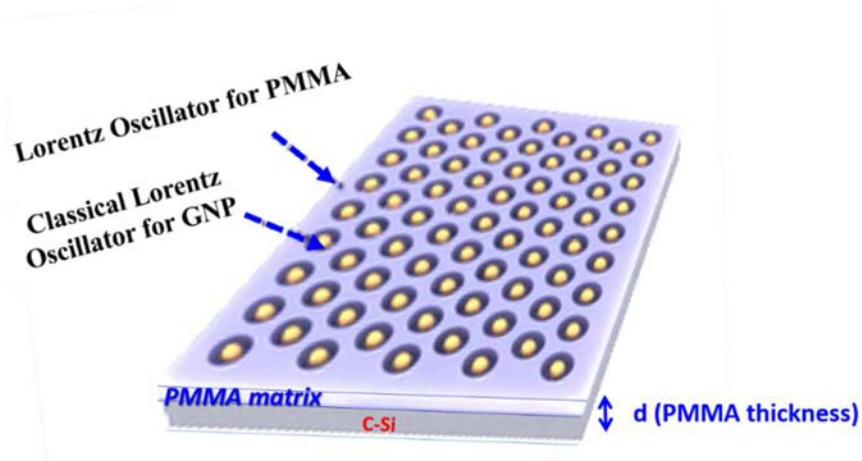


Fig. 43 Schematic representation for the physical model used ellipsometry data analysis.

In this model, the PMMA layer and the GNPs are considered as one homogenous layer. Modeling this layer was carried out using two classical Lorentz oscillators, one is for GNPs and the other is for PMMA film according to the following Lorentz dispersion equation: [20],[21]

$$\varepsilon(\omega) = \varepsilon_{\infty} + \omega_p^2 \sum_{i=1}^N \frac{f_i}{\omega_{0,i}^2 - \omega^2 + j \omega \Gamma_i} \quad (3)$$

Where; ε_{∞} is the dielectric function at high frequency, ε is the dielectric function, ω is the light energy (eV), ω_p is the plasma frequency, f_i is the oscillator strength of the i^{th} resonator, $\omega_{0,i}$ is the plasmon resonance frequency (natural frequency) of the i^{th} resonator; one for gold and the other is for polymer (PMMA) and Γ_i is the damping rate of the i^{th} resonator (friction coefficient). In our case $N=2$.

Based on equation (3), the optical properties (n , k , ε_r , and ε_i) of the targeted material will be obtained according to the following equations:

$$\varepsilon_r = n^2 - k^2, \quad (4)$$

$$\varepsilon_i = 2nk, \quad (5)$$

$$\alpha = \frac{4\pi k}{\lambda} \quad (6)$$

Based on these equations, the ellipsometric angles are highly dependent on the substrate, the film thickness and the optical constants of composite layer as shown in the discussion part.

4.2.2 Ellipsometric data analysis

Once the measurements are performed, we tackle the numeric modeling of the data in order to extract the optical properties. The values of the known optical constants of the Si substrate are measured and kept fixed for the rest of the modeling. The unknown parameters such as thickness of PMMA layer and optical constants of coated films are determined by minimizing the χ^2 error function between the experimental and the calculated ellipsometric data. The Levenberg-Marquardt [22] algorithm is performed for the calculation of χ^2 values according to the following equation:

$$\chi^2 = \sum_{i=1}^N (\Psi_{\text{exp } i} - \Psi_{\text{model } i})^2 + (\Delta_{\text{exp } i} - \Delta_{\text{model } i})^2, (7)$$

where N is the number of data collected versus wavelength (λ), Ψ_{exp} and Δ_{exp} are the experimental data. Ψ_{model} and Δ_{model} are the modeled (fitted) ellipsometric angles.

Herein, we present an example of spectral fitting in Fig. 44, where it shows clearly that the error between measured and calculated parameters is less than 1% confirming the validity of this model.

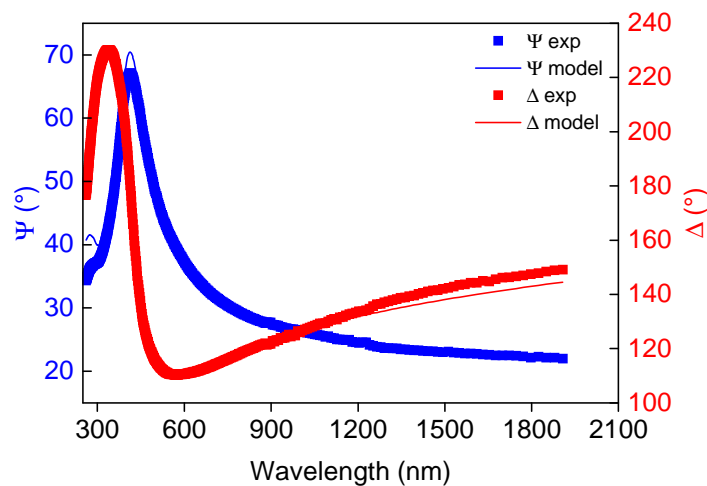


Fig. 44 Ellipsometric spectrum of the experimental parameters (Ψ_{exp}) and (Δ_{exp}) values (scattered lines) compared with fitted ones (Ψ_{model} and Δ_{model}) (solid lines). The measurements are performed at an angle of incidence 60° on a silicon substrate coated with GNPs (40 mg of NaAuCl_4 / MIBK/ethanol using 10000 rpm).

In this figure, we clearly see that experimental spectra are correctly reproduced by the proposed model (see Fig. 43). Despite the slight disagreement that was shown in the NIR regions, good

agreement is found between the calculation and the experimental spectra. Once this agreement is obtained, the optical parameters (refractive index (n), extinction coefficient (k), dielectric function (ϵ) and absorption coefficient (α)) of PMMA layers containing GNPs are determined and analyzed.

4.3 Results and Discussions

4.3.1 Optimizing the mechanical parameters

4.3.1.1 Effect of the speed (in NaAuCl₄/ MIBK/ethanol)

The AFM images in Fig. 45 display a direct increase in the density of the GNPs and a decrease in the size distribution through the increase in the ERs from 2000 to 5000 rpm. To illustrate, the size of GNPs at low ER (2000 rpm) was large and the size distribution is high. However, when the evaporation of the solvent increases to 10000 rpm, the size distribution of the GNPs over the surface of the silicon substrate decreases frequently. Between 5000 and 10000 rpm, there is no significant increase in the density of the GNPs.

In addition, the size of the PMMA holes decreases with increasing the ERs as obtained previously in chapter 2. Therefore, we expect to have a decrease in the thickness of PMMA film.

Concerning the shape of GNPs, we should have quadrilateral shapes (cubical or trapezoidal) based on the synthesis method and the used chemical parameters that were discussed clearly in shape control study (chapter 3). In Fig. 45, it seems that shape of GNPs is spherical, which is not the case as will be demonstrated below by ellipsometry. We performed SE measurements on these three samples in order to estimate the thickness and the optical properties as shown in the following section.

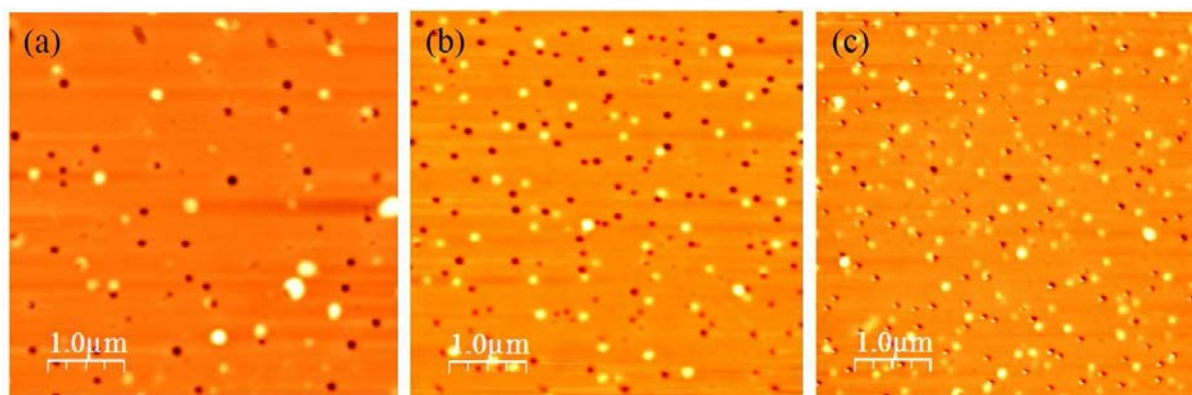


Fig. 45 Evolution of AFM images of GNPs using 40 mg of NaAuCl₄/ethanol/MIBK at increased ERs: (a) 2000 rpm, (b) 5000 rpm and (c) 10000 rpm. Images scanned in non-contact mode.

4.3.1.1.1 Ellipsometric measurements and modeling

The measured ellipsometric parameters of the above three samples at an angle of incidence of 60° are reported in Fig. 46. The three curves in this figure exhibit the same behavior with a slight shift in both parameters (Ψ & Δ) which can demonstrate similar structures and optical properties of composite layer. The above AFM images in Fig. 45 show approximately identical structures of assemblies of GNPs embedded in PMMA film over the silicon substrates in the three samples. Moreover, at low evaporation rate (2000 rpm), we observed an increase in the amplitude of the spectrum. This observation could be related to the large size distribution or due to higher thickness.

Thus, the observed difference in the Ψ and Δ amplitudes is more efficient in the visible (VIS) spectral range at low ER (2000 rpm) due to the strong contribution of large sized GNPs in the optical responses in this spectral range.

These spectra showed a shift at 2000 rpm particularly for Δ , so one should expect to have higher thickness value at this ER compared to higher ERs (5000 and 10000 rpm). In fact, it is already proved in the previous chapters that low evaporation rates (ERs) result in high thickness values. In order to confirm these observations and to extract the necessary optical constants of the embedded GNPs in the PMMA film (over Si-substrate), a correct physical model was managed.

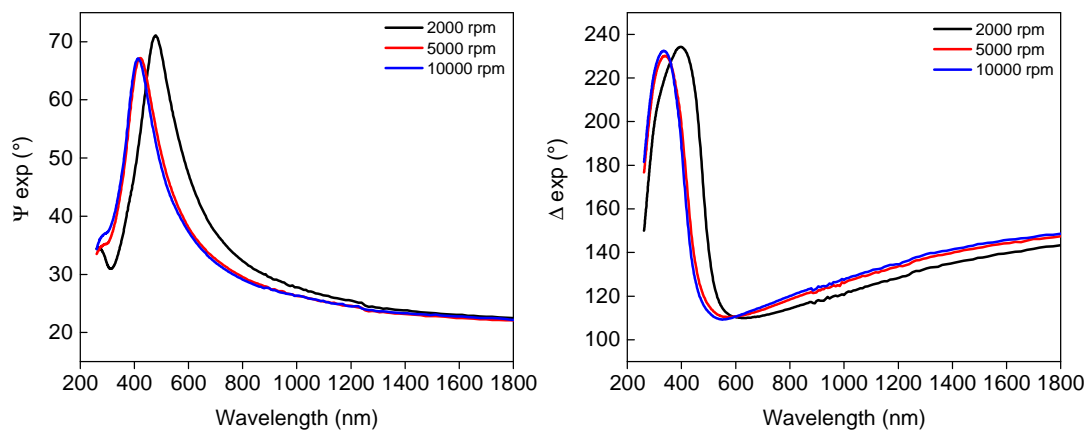


Fig. 46 Evolution of the measured ellipsometric angles (Ψ & Δ) in three different samples of GNPs (40 mg Au^{3+}). Measurements performed at room temperature at incident angle 60° . Samples prepared at increased spin-coating ERs as shown in the two spectra.

Experimental ellipsometry spectra in Fig. 46 are fitted by the given model (Fig. 43) upon minimizing the mean squares deviation (χ^2 error) between the experimental and the calculated ellipsometric data as shown in Fig. 47.

Except for the slight disagreement, it is observed in Fig. 47 that the model shows a good agreement between the experimental data and the calculated spectra. Such disagreement

(difference) can be explained by the inhomogeneity of the surface and/or by some roughness existing at low evaporation rates.

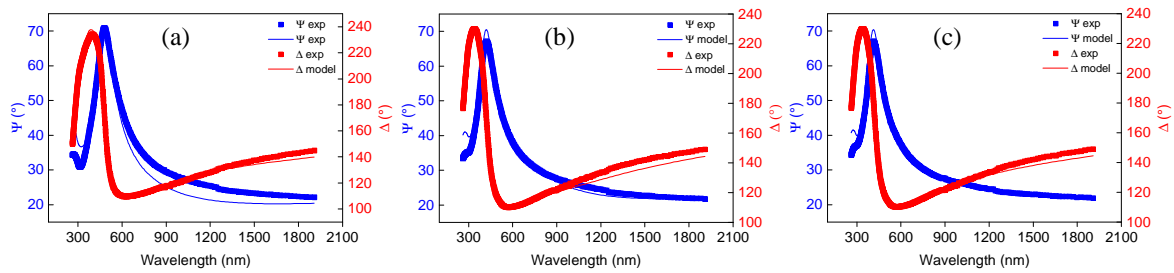


Fig. 47 Comparison between the experimental SE data (squares) and the modeled (lines) achieved by the constructed model in three ERs. (a) 2000 rpm, (b) 5000 rpm and (c) 10000 rpm.

4.3.1.1.2 Extracting the thickness values and the optical constants

The determined thickness values by SE analysis of the PMMA film with respect to increased ER are shown in Fig. 48.

Herein, the increase in the ERs from 2000 to 5000 rpm leads to a rapid decrease in the thickness of the polymer film (PMMA) from 94 to 82 nm as seen in Fig. 48. This decrease confirms what we expected with respect to the AFM images and the Ψ and Δ measurements. Concerning the measurements in Fig. 46, we link the shift at a higher wavelength (λ) which was obtained at low ER (2000 rpm) to a higher thickness value which seems true according to the resulted higher value (94 nm). In contrast, the increase in the ER from 5000 to 10000 rpm leads to a very slight decrease, where the thickness reaches 79 nm, which is the minimal thickness value. Accordingly, the speed 5000 rpm serves as a standard ER, so the thickness of the PMMA is said to be constant.

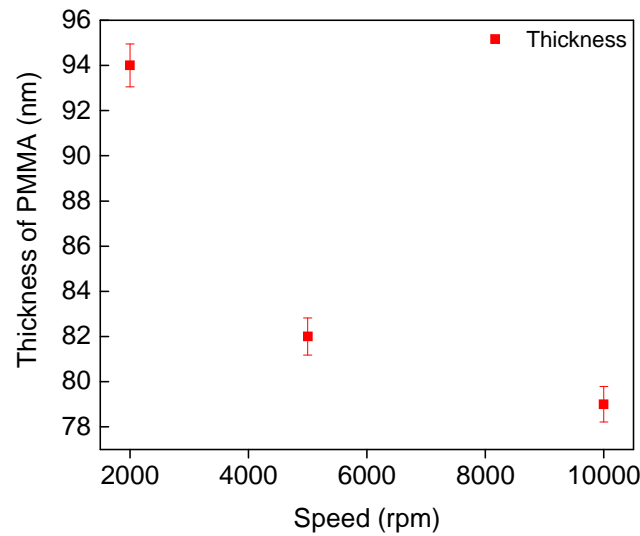


Fig. 48 Evolution of the film thickness as function of increased evaporation rates.

The imaginary ϵ_i and real ϵ_r parts of the dielectric function of GNPs loaded in PMMA holes were extracted using the proposed model as seen in Fig. 49.

At 2000 rpm, the amplitude of ϵ_i and ϵ_r is greater compared to higher speeds (5000 and 10000 rpm). Despite this difference, these samples exhibit the same behavior of the curves for both dielectric function (ϵ_i and ϵ_r) of the GNPs.

As a result, we conclude that the same behavior existing in both ϵ_i and ϵ_r curves could be explained by the low size distribution. Thus, the two samples (5000 and 10000 rpm) show the same structure of GNPs with less size distribution. Despite the slight variation in ϵ_i and ϵ_r in the first sample (2000 rpm), the behavior of ϵ_i and ϵ_r curves in the three samples is the same.

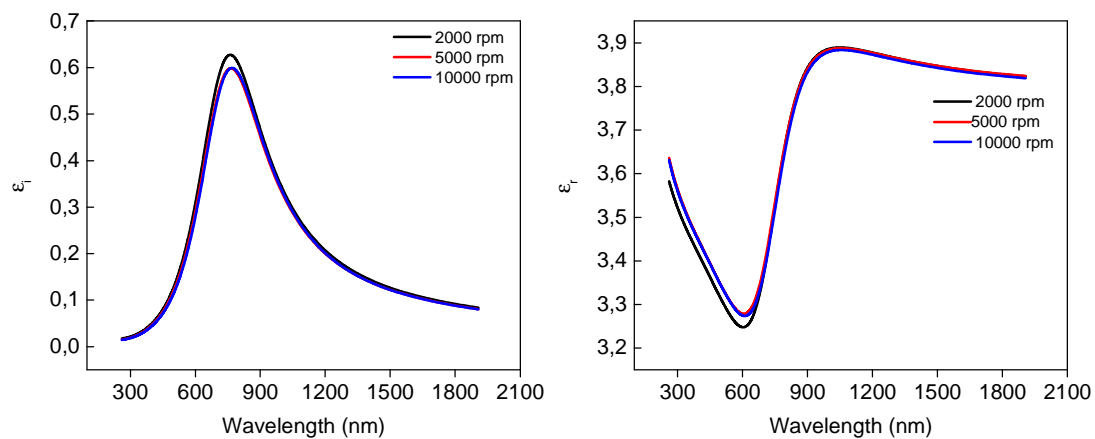


Fig. 49 Comparison between the dielectric function (ϵ_r and ϵ_i) of the three samples having increased ER that is determined using the model.

Knowing that there is an interdependent relationship between ϵ_i and α , the behavior of the absorbance spectra in Fig. 50 looks like the spectra of ϵ_i in Fig. 49. Here, higher ERs at 5000 and 10000 rpm have the same behavior of the absorbance spectra in the VIS-NIR regions. They display the same plasmon band which is positioned at 730 nm. The redshift in the samples with high ERs (5000 and 10000 rpm) is related to the increase in the density of the GNPs over the surface of the Si substrate compared to the samples with low ER (2000 rpm), where the number of the NPs is less. As a result, these samples (5000 and 10000 rpm) possess the same size and shape, based on the above AFM images (Fig. 45) and on the plasmon band (730 nm). In contrast, the low ER at 2000 rpm is blue shifted by 5 nm with respect to the high ERs (5000 and 10000 rpm), its plasmon band is positioned at 725 nm. In addition, the highest intensity observed at this ER is linked to the huge size distribution presented within such sample. Despite the slight difference in the two absorbance bands at 725 and 730 nm, we can conclude that both bands reflect one SPR band. Thus, the obtained SPR band emphasize that the obtained shape is not spherical at all. Typically, the spherical Gold nanoparticles have a single SPR band ranging from 517 to 580 nm with increased size of GNPs. [23-25]

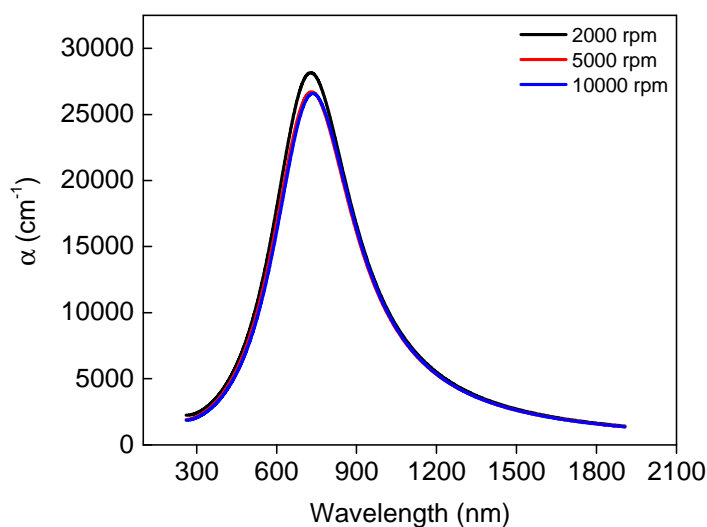


Fig. 50 The absorbance coefficient (α) spectra as a function of wavelength extracted by the model of the three samples that were performed at increased ERs.

In summary, the obtained spectral fitting of SE data was reasonable and yielded important information (thickness, dielectric function and the absorption coefficient). It is found that this technique and the developed model are suitable for these assemblies of GNPs embedded in PMMA holes. Low ER results in high thickness and in large size distribution. Consequently, we found that the speed 5000 rpm is a good choice to carry out the synthesis of non-spherical GNPs in MIBK (PMMA solvent) and therefore the ellipsometric measurements. This speed

generates higher density of non-spherical GNPs and less size distribution with a SPR in the NIR region (730 nm).

4.3.1.2 Effect of the speed (in NaAuCl₄/acetone/ethanol)

The ellipsometric measurements, modeling and analysis were presented in the following study. It was shown in the above study (4.3.1.1) that the increase in the ER leads to the decrease in the thickness and the size of the non-spherical GNPs as well to an increase in the density of GNPs. Herein, it was interesting to change the solvent of the PMMA from MIBK into acetone, in order to verify the influence of the solvent on the thickness and on the optical constants.

It was reported in the above two chapters (2 and 3) that acetone induces the reduction of GNPs and forms more monodispersed GNPs compared to MIBK, knowing that acetone is more volatile than MIBK. Moreover, acetone serves as a good solvent for PMMA, so that the repulsive interaction between: "PMMA and the couple: gold (NaAuCl₄) / NaAuCl₄ solvent" is stronger. [26] Based on the SEM images that were shown in Fig. 51, it is clearly observed that the increase in the ER from 2000 rpm to 5000 rpm leads to an increase in the density of GNPs, similarly to the obtained by MIBK and also to a decrease in the size distribution. Moreover, we found that the increase in the density of GNPs is more significant compared to the above study (4.3.1.1). However, the three ERs result in monodispersed Gold nanocubes (GNCs).

At 10000 rpm, the size and the shape are monodispersed. Whereas, at 5000 rpm, we have higher volume fraction of GNPs in comparison to the other ERs. Within the same ER, it seems clearly that assemblies of GNPs reveal a closely uniform size and shape.

Again, we found that 5000 rpm serves as a good parameter to carry out the synthesis method of higher density of smaller sized GNCs. To confirm this observation, ellipsometric measurements were made for these GNCs in the following section.

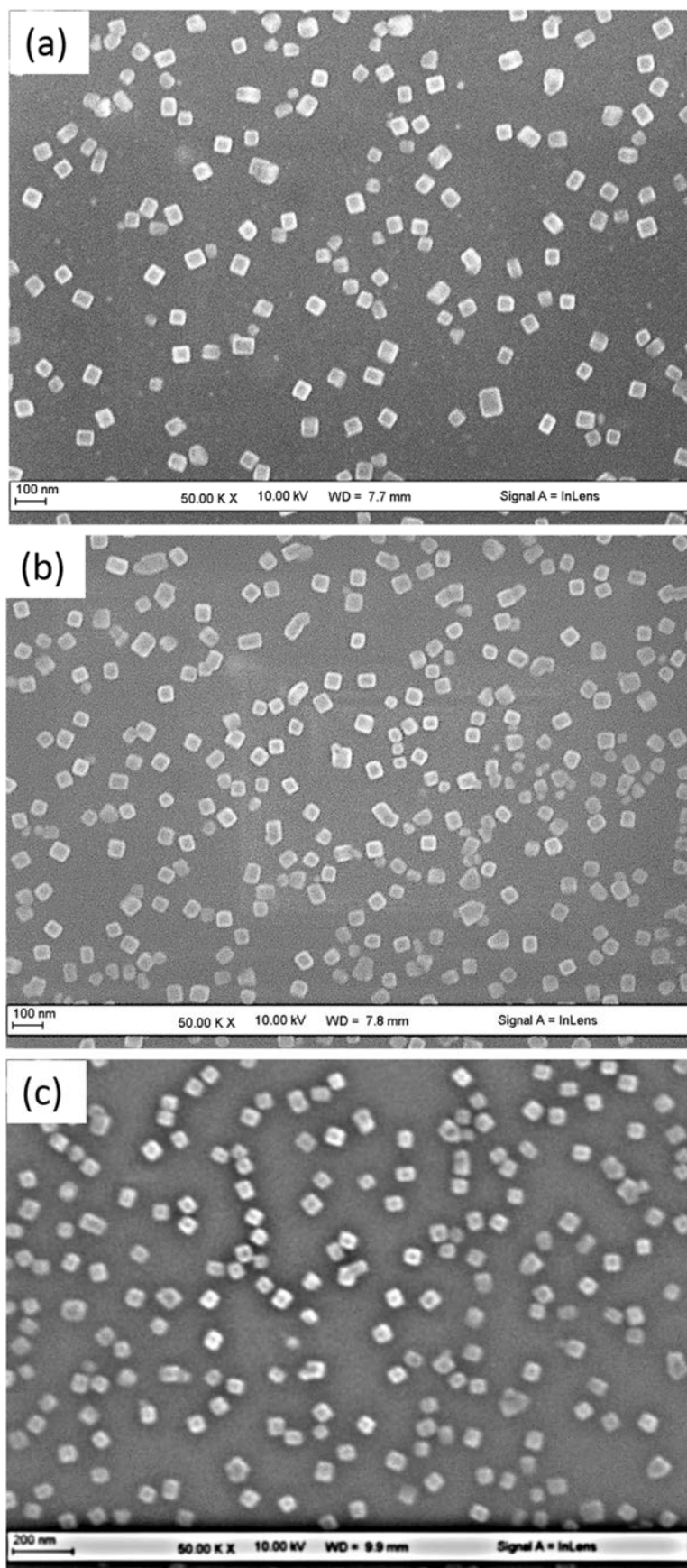


Fig. 51 SEM images of 40 mg gold precursor (NaAuCl_4 /acetone/ethanol) showing GNCs at increased ERs: (a) 2000 rpm, (b) 5000 rpm and (c) 10000 rpm.

4.3.1.2.1 Ellipsometric measurements

The ellipsometric measurements of these three samples are shown in Fig. 52.

As compared to Fig. 46, we observed distinctly in Fig. 52 a direct shift in both Ψ and Δ spectra in the VIS-NIR regions followed by an increase in the amplitude of these spectra by decreasing the ERs from 10000 to 2000 rpm. Accordingly, we expect to have higher thickness values and redshifted SPR bands in the VIS-NIR regions, knowing that the optical properties and the thickness are highly dependent on the ellipsometric measurements. Therefore, these measurements will be fitted by the model illustrated in Fig. 43 as seen in Fig. 53.

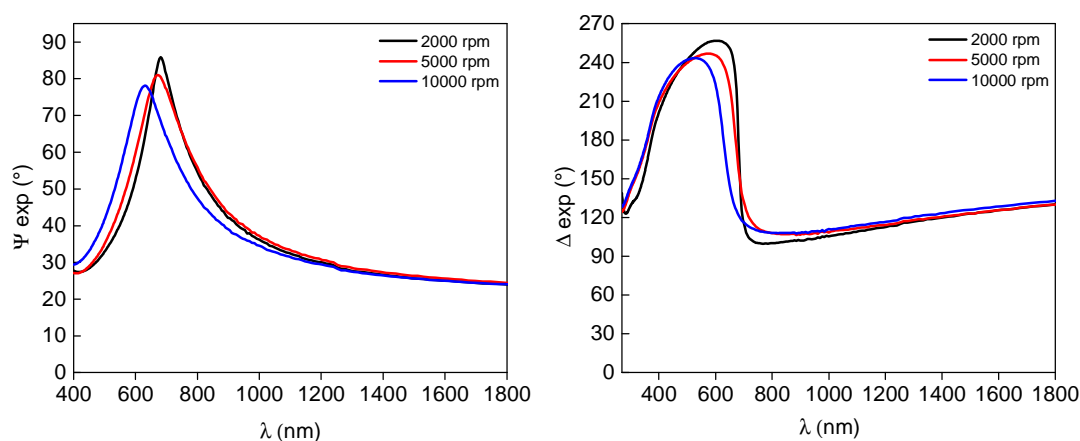


Fig. 52 Spectroscopic ellipsometric data (Ψ & Δ) of assemblies of GNCs attached to the PMMA film on silicon substrate at increased ERs. Measurements performed at room temperature at incident angle 60° .

4.3.1.2.2 Fitting the experimental measurements

The experimental ellipsometric data (Ψ & Δ) for GNCs embedded in PMMA film were fitted by the proposed model as shown in Fig. 53. The model successfully simulates important features for all Ψ and Δ curves particularly, at ~ 700 nm, where absorption may occur. The slight difference between the measured and calculated data that remains can be attributed to GNCs shape which is not considered in the modeling. Moreover, both ERs (2000 and 5000 rpm) display better fitting than 10000 rpm. Hence, the less thickness value generated at high ER (10000 rpm) can reduce the sensitivity of the interaction between light and GNPs of composite layer.

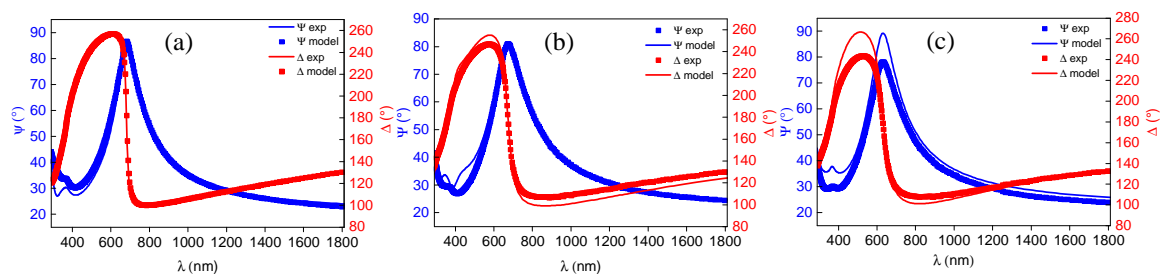


Fig. 53 Ellipsometric spectra of GNCs: squares spectra for measured (experimental) data and solid lines for the calculated (modeled). The incident angle is 60° .

4.3.1.2.3 Extracting the thickness and the optical constants

After modeling Ψ and Δ curves, the second step is to determine the thickness of the PMMA film. The numerical results of the thickness values which were determined in Fig. 54 for the three samples are in agreement with the SEM images (Fig. 51) and Ψ - Δ measurements (Fig. 52).

The three samples (in acetone) showed high thickness values ranged between 153 and 114 nm compared to the previous study (MIBK). This is related to the higher volatility of acetone compared to MIBK. This remark confirms with the above Δ measurements that presented higher shift with respect to decreased ERs (see Fig. 52).

Based on Fig. 54, the increase in the ER from 2000 to 5000 rpm showed a higher decrease in the thickness value from 153 to 124 nm. On the other hand, the increase in the ER from 5000 to 10000 leads to a slight decrease in the thickness from 124 to 114 nm as obtained in the previous study (4.3.1.1).

The imaginary ϵ_i and the real ϵ_r parts of the dielectric function of GNPs are also extracted as reported in Fig. 55.

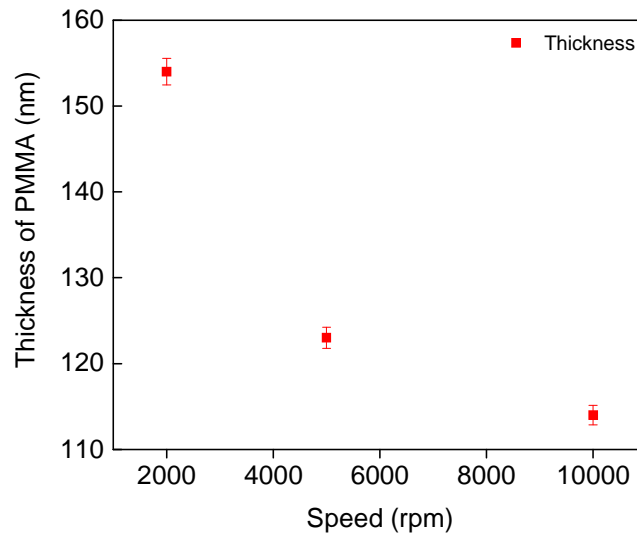


Fig. 54 Thickness plot (for PMMA film) as function of evaporation rate.

The spectra are shown in Fig. 55 and the used parameters by the proposed model were given in the experimental part (materials and methods).

The increase in the ER from 2000 rpm to 5000 rpm affects the dielectric function ϵ_i and ϵ_r . It leads to a direct shift in the wavelength and an increase in the intensity of ϵ_i . This is strongly related to the presence of more GNCs at 5000 rpm compared to 2000 rpm as shown in the SEM images in Fig. 51. In contrast, the increase in the ER from 5000 to 10000 rpm leads to a blue shift in ϵ_i without a significant change in its amplitude. This can be related to the presence of the smaller sized GNCs at 10000 rpm compared to 5000 rpm.

Similarly, despite the significant change in the amplitude of ϵ_r curves, the three samples have shown the same behavior. The increase in the refractive index of the composite layer with the increase in the ER can explain this change in the amplitude of ϵ_r . Indeed, the increase in the ER leads to an increase in the density of GNPs and a decrease in the size distribution of these GNPs. It is worth noting that the noticeable features found in the 600–800 nm region of the spectra of the dielectric function (ϵ_i and ϵ_r) reflect the absorption region of the GNCs.

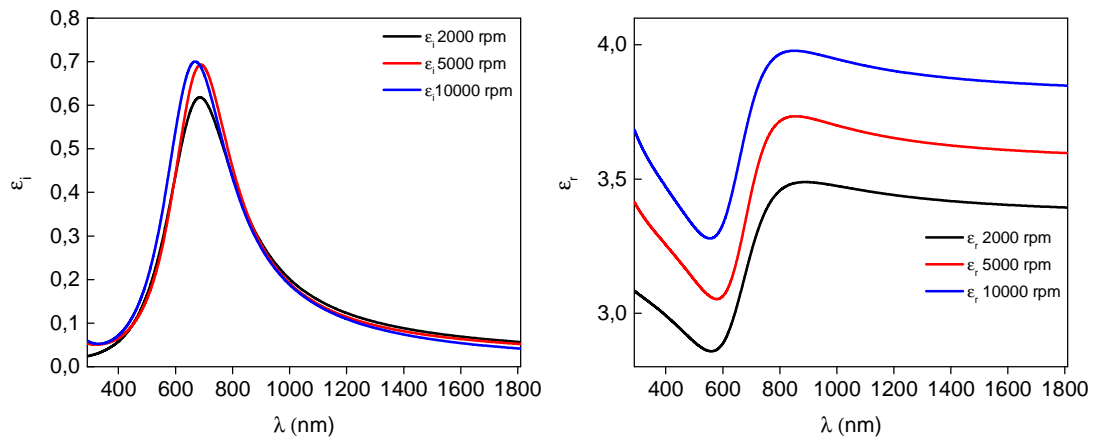


Fig. 55 Imaginary part (left) and Real part (right) dielectric function of monodispersed GNCs assembled in PMMA films.

The absorbance coefficient spectra of the three samples are shown in Fig. 56. Herein, the increase in the ER from 2000 rpm to 5000 rpm leads to a red shift in the plasmon band from 662 nm to 670 nm as well as to an increase in the amplitude. This can be attributed to the increase in the density of GNCs embedded in the PMMA film over the surface of the silicon substrate. [20] On the other hand, the increase in the ER from 5000 rpm to 10000 rpm leads to a blue shift (20 nm) in the plasmon band from 670 to 650 nm, due to presence of smaller GNCs at increased ER.

Accordingly, we found that the speed 5000 rpm records a significant increase in the density of the GNPs with respect to the other ER. As a result, it exhibits a strong absorption with the SPR band at 670 nm. Thus, the SPR band is highly dependent on the density of GNPs as well as on the size and the shape of the GNPs.

After determining the favorable evaporation rate (5000 rpm) to carry out the synthesis and the ellipsometric measurements, we performed different experiments at this speed as shown in the following sections. Thereby, the influence of the size and the shape of GNPs on the SPR bands is evaluated.

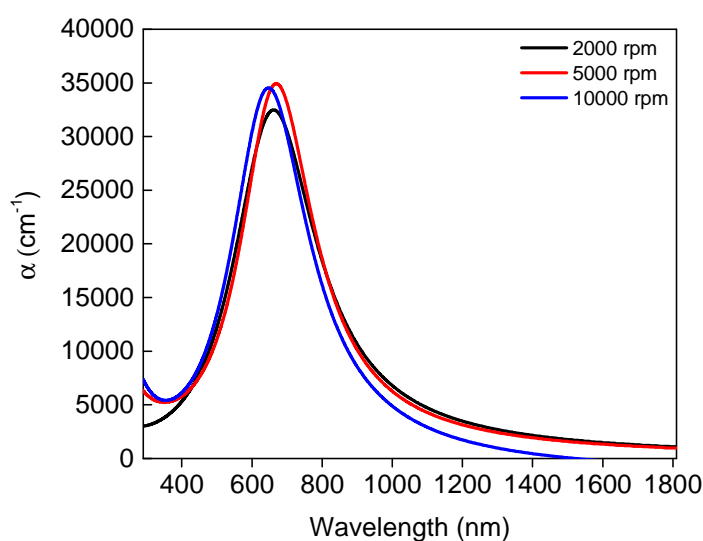


Fig. 56 Absorbance coefficient (α) plot of GNCs as a function of wavelength (nm) in increased ERs.

In summary, this study showed that the ER parameter has a direct effect on the thickness of the PMMA film, on the volume fraction or the density of the GNPs and on the size distribution (size of GNPs). The speed 5000 rpm was found to be a good parameter to improve the synthesis of GNPs where higher number of smaller GNCs are obtained, thereby, a strong SPR band is achieved.

So, higher volume fraction of smaller GNCs and also higher thickness that facilitate the ellipsometric measurements are formed at this speed (5000 rpm), knowing that the thickness of composite layer as well the volume fraction of nanoparticles are the key factors for good optical responses by ellipsometry measurements. [4]

We showed that the SPR band of GNCs is sensitive to the change in the size of the NPs.

It was observed that acetone favors the reduction of GNPs, as a result it serves as a good solvent for PMMA to synthesize monodispersed GNPs (GNCs) in comparison to MIBK.

4.3.2 Optical properties of shape-controlled gold nanoparticles (GNPs)

Based on chapter 3, the formation of various shapes (GNCs, GNHs and GNTs) of GNPs was achieved according to the simple synthesis method that we applied in this work.

By adjusting the experimental conditions (solvent of PMMA, PH of gold precursor and the solvent of gold precursor) of the synthetic method and altering the growth rate of formation, the formation of controlled shapes of GNPs was induced.

This section describes the optical properties by the SE of multiple samples of shape controlled GNPs.

4.3.2.1 Control the formation of uniform gold nanocubes (GNCs)

In chapter 3, we found that the formation of uniform GNCs is achieved by alerting the experimental conditions as illustrated in Fig. 57. As reported in chapter 3 and shown in Fig. 57, NaAuCl₄/ethanol favors the formation of uniform GNCs with acetone (see Fig. 57 b) and forms Poly-dispersed shapes of sharper corner of GNCs and gold nanorectangles (GNRs) with MIBK (see Fig. 57 d). In contrast, HAuCl₄/ethanol has no great control (produces poly-dispersed GNHs and GNTs) in acetone (Fig. 57 a) and tend to generate poly-dispersed GNHs in MIBK as seen in Fig. 57 c. As shown in chapter 3, hexagonal gold nanoparticles (HGNs) were obtained when NaAuCl₄ is replaced by HAuCl₄. Therefore, the PMMA solvent and the Au precursor are key parameters to control the shape of GNPs, because they have a direct influence on the kinetic rate of formation of GNPs. All details are given in chapter 3, but in this chapter we focus on the optical characterization of these samples by SE measurements.

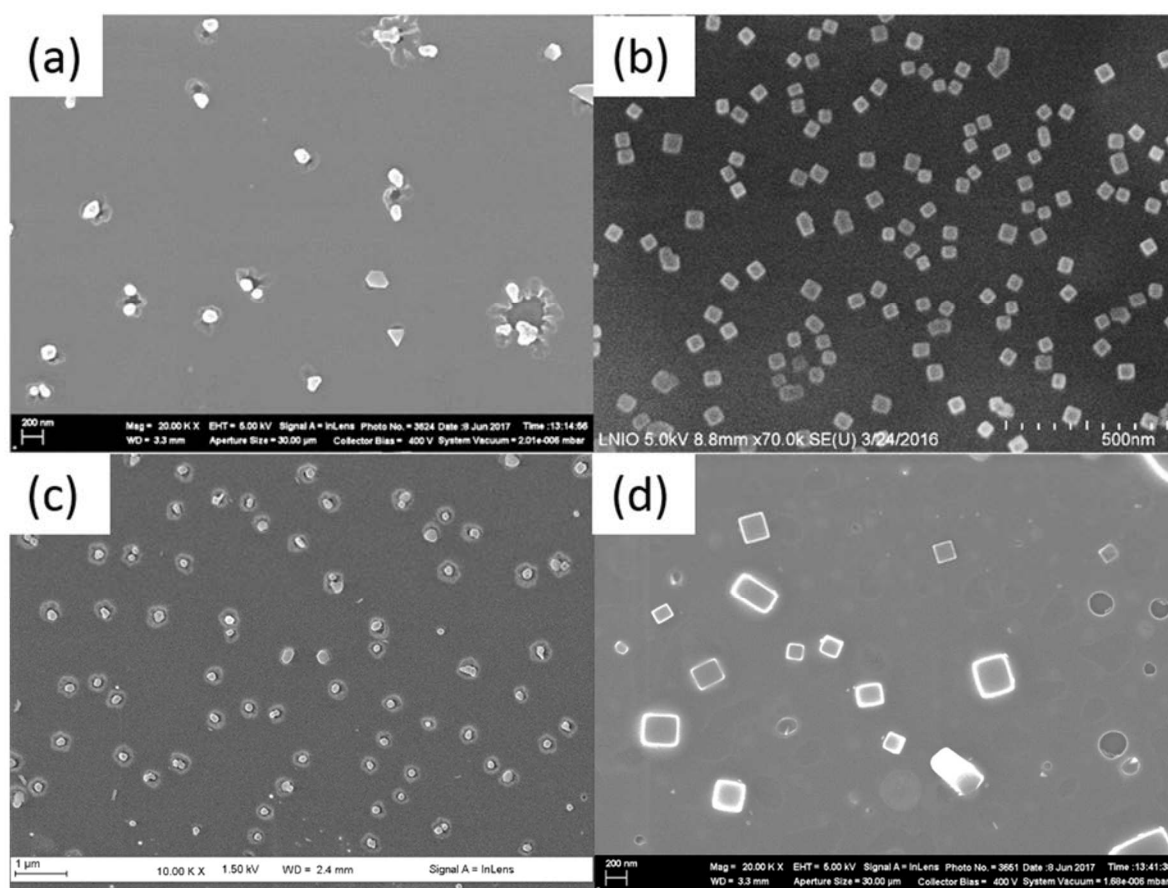


Fig. 57 SEM images showing various shapes of GNPs. (a) poly-dispersed GNHs and GNTs, (b) monodispersed GNCs, (c) poly-dispersed GNHs and (d) poly-dispersed GNCs and GNRs. (a) and (b) prepared with same PMMA solvent (acetone) and different Au precursor (a in HAuCl₄ & b in NaAuCl₄). (c) and (d) prepared at same PMMA solvent (MIBK) and different Au precursor (c in HAuCl₄ & d in NaAuCl₄). The four samples were prepared at the same standard spin-coating parameters and same solvent precursor (ethanol).

4.3.2.1.1 Ellipsometric measurements and modeling

According to Fig. 58, we observe a direct shift in the wavelength of both Ψ and Δ measurements. Samples prepared with acetone (black and red) showed a shift with respect to samples being prepared with MIBK (blue and green spectra). Knowing that acetone is more volatile, this shift is linked to the high thickness values that can be obtained in the presence of acetone compared to MIBK.

These measurements were modeled by the proposed model as shown in Fig. 59.

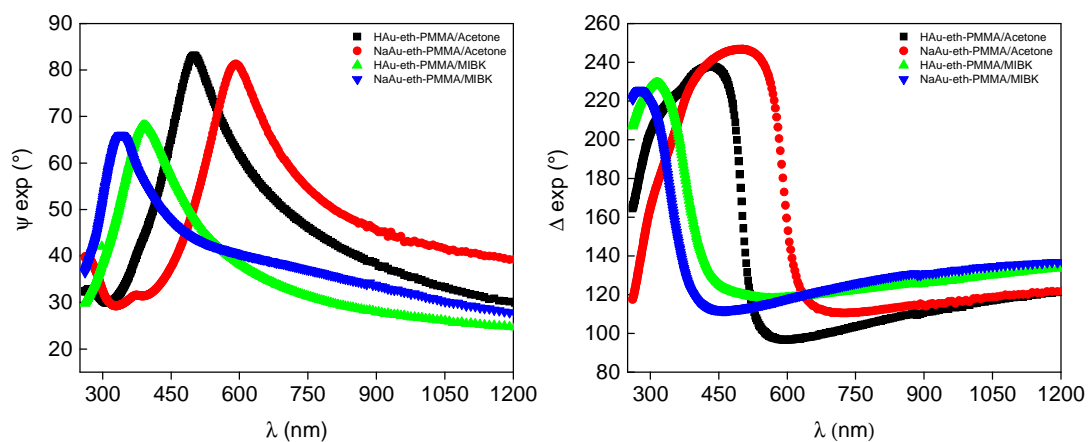


Fig. 58 Measured ellipsometric parameters of Ψ (left) and Δ (right) values for GNPs embedded in PMMA film on Si wafers prepared with different synthetic parameters. Samples prepared at same spin-coating conditions. Measurements performed at incident angle of 60° .

The comparison between measured and calculated ellipsometric spectra (Ψ model and Δ model) is shown in Fig. 59. Despite the slight fitting disagreements that can be observed, the model reproduces correctly the experimental spectra.

NaAuCl₄ precursor prepared with acetone (Fig. 59 b) shows better agreement than HAuCl₄ in acetone (Fig. 59 a). This confirms the above contribution concerning the PMMA solvent and the type of precursor. NaAuCl₄ is more selective to PMMA/Acetone than PMMA/MIBK as demonstrated in chapter 3.

In contrast, HAuCl₄ in MIBK (Fig. 59 c) validates the fitting data of UV-VIS regions, where NaAuCl₄ in MIBK (Fig. 59 d) shows some disagreements in the VIS-NIR. Thereby, HAuCl₄ is more selective to PMMA/MIBK than PMMA/Acetone as presented in chapter 3.

Furthermore, Δ spectra extend to significant longer wavelengths of broader bandwidth in acetone (a and b) compared to the samples prepared in MIBK (c and d). Accordingly, we expect to have higher thickness in PMMA film of these samples (a and b).

Thus, HAuCl_4 is selective to PMMA /MIBK and NaAuCl_4 to PMMA/Acetone, so that the repulsive interaction is stronger.

The fitting results of the experimental spectra are given in the following subsection.

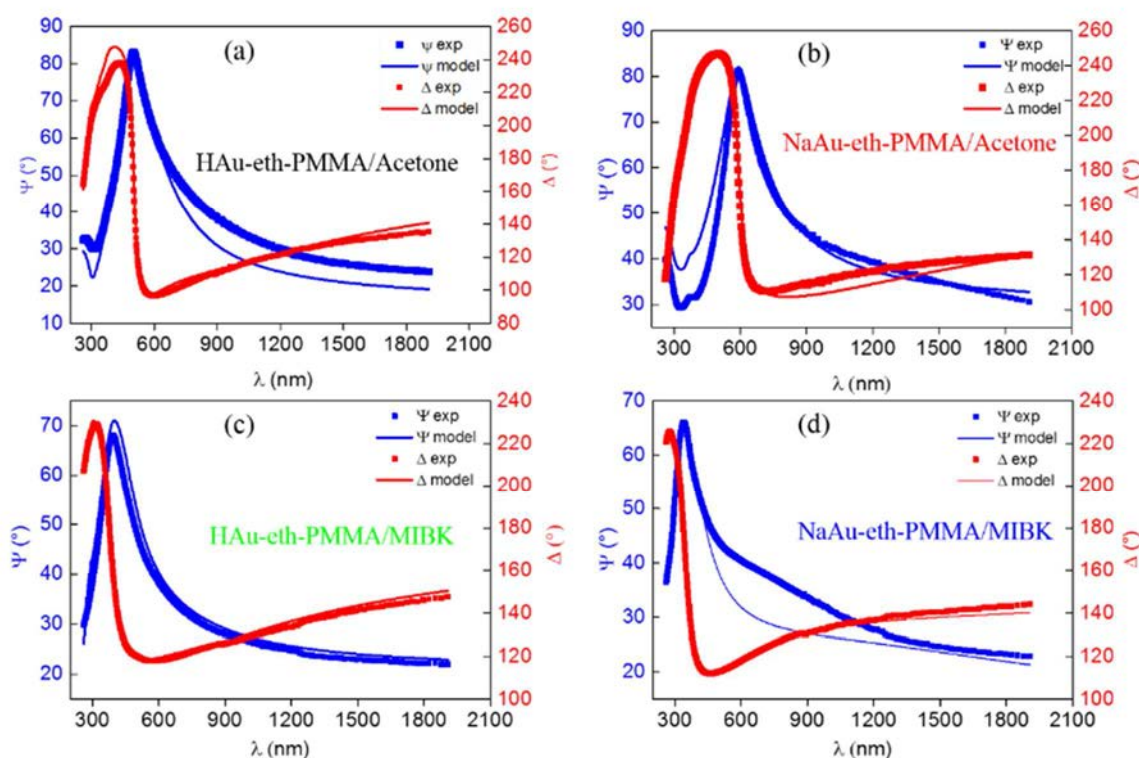


Fig. 59 Comparison between measured and calculated ellipsometric spectra for GNPs embedded in PMMA film over Si wafers prepared over various experimental conditions as shown in these spectra. Samples prepared at same spin-coating conditions and measurements performed at incident angle 60° as a function of the wavelength (λ).

4.3.2.1.2 Extracting the thickness and the optical constants

The evolution of the thickness of PMMA film of the above four samples was illustrated in Fig. 60. Due to high volatility of acetone, samples prepared with acetone show high thickness values, 130 nm and 170 nm, with HAuCl_4 and NaAuCl_4 , respectively. In contrast, samples with MIBK display low thickness values with a slight variation, 84 nm and 90 nm, with HAuCl_4 and NaAuCl_4 , respectively.

Accordingly, we need to study if there is some correlation between the thickness value and the optical properties of composite layer. This will be examined with the aid of the following figures.

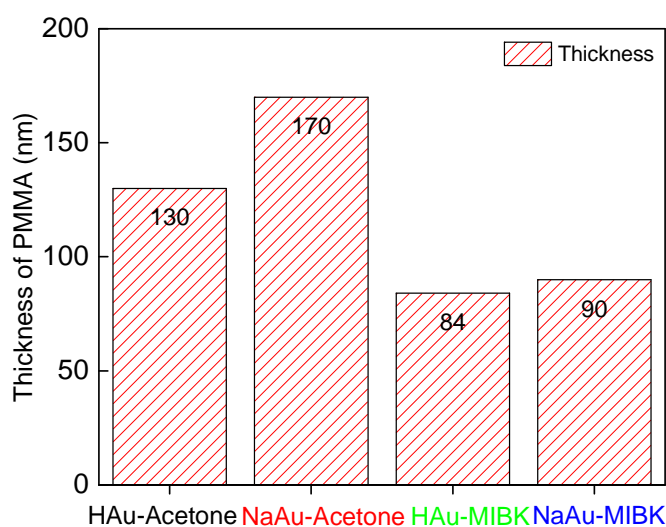


Fig. 60 Evolution of the thickness of PMMA film in four different samples. Samples prepared at same spin-coating conditions.

The resulting optical properties of the dielectric function (ϵ_i and ϵ_r) are shown in Fig. 61.

Based on the above figure (Fig. 60), we expected to have a redshift in the dielectric function for samples displaying high thickness values, which is not the case. Indeed, samples with low thickness values (samples prepared in MIBK) lead to a red shift in both dielectric function spectra (ϵ_r and ϵ_i) and also to an increase in the amplitude of these spectra as seen in Fig. 61. No direct influence of the thickness on the optical properties of these samples can be observed as seen in Fig. 61.

The change of optical responses such as the plasmonic band shift is strongly linked to the structural shape, size and density of the GNPs in PMMA films.

To illustrate, changing the PMMA solvent from acetone to MIBK increases the strength of the oscillators and sharpens the resonance peak (blue and green spectra) but it does not significantly influence its position within the same solvent. However, it leads to a redshift in these spectra compared to samples prepared with acetone (black and red spectra).

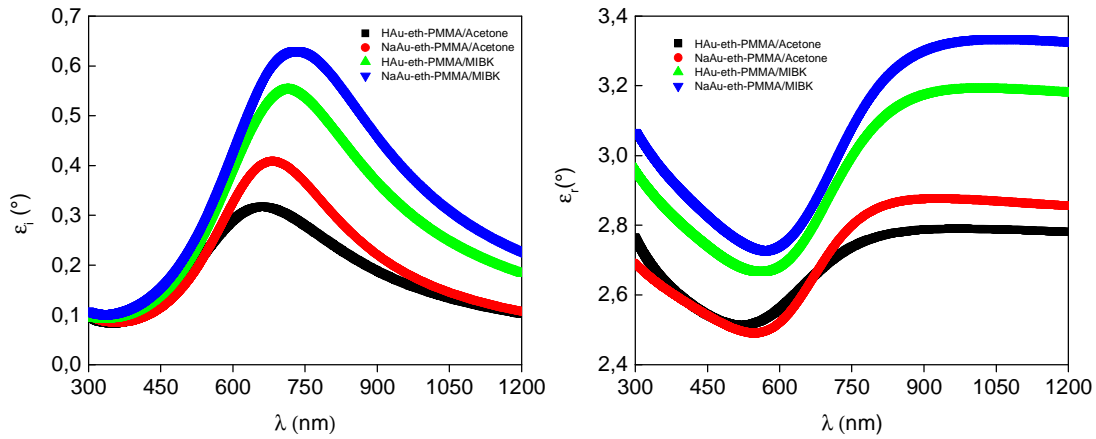


Fig. 61 Dielectric function of ϵ_i (left) and ϵ_r (right) spectra for gold nanoparticles at different experimental conditions as shown in both spectra.

As mentioned in chapter 3, the absorption spectra of the samples containing GNPs of various shapes show significant variations in the optical absorption properties as shown in Fig. 62. According to Fig. 60, high thickness value of acetone does not systematically lead to a shift in the absorbance band as shown in Fig. 62.

Furthermore, poly-dispersed GNPs of GNHs & GNTs (green spectrum) and poly-dispersed GNPs of GNRs & GNCs of sharp corners (blue spectrum) showed a red shift in the absorbance band spectra with respect to monodisperse GNCs of flattened corners (red spectrum) and the poly-dispersed GNHs and polygonal shapes (black spectrum), mainly due to increase in size of nanoparticles for each red shift.

Thus, the sample containing GNCs of flattened corners (red spectrum) reflects the best experimental conditions to obtain well controlled shape of GNPs (GNCs), with the large bandwidth and a wavelength of 640 nm.

Poly-dispersed GNRs and GNCs (blue spectra) display the most red-shifted plasmon band at 690 nm. This spectra is red shifted with respect to mono-dispersed irregular GNHs (green spectra) that is located at 677 nm. This red shift is basically linked to the significant increase in the density of sharp GNCs and to the slight increase in the size of these GNPs as explained well in chapter 3.

Note that only one plasmon mode in the VIS-NIR spectral range can be observed, since we used two oscillators in the proposed model without any additional oscillators to consider the anisotropic effect of GNPs such as sides and corner modes. [27],[28]

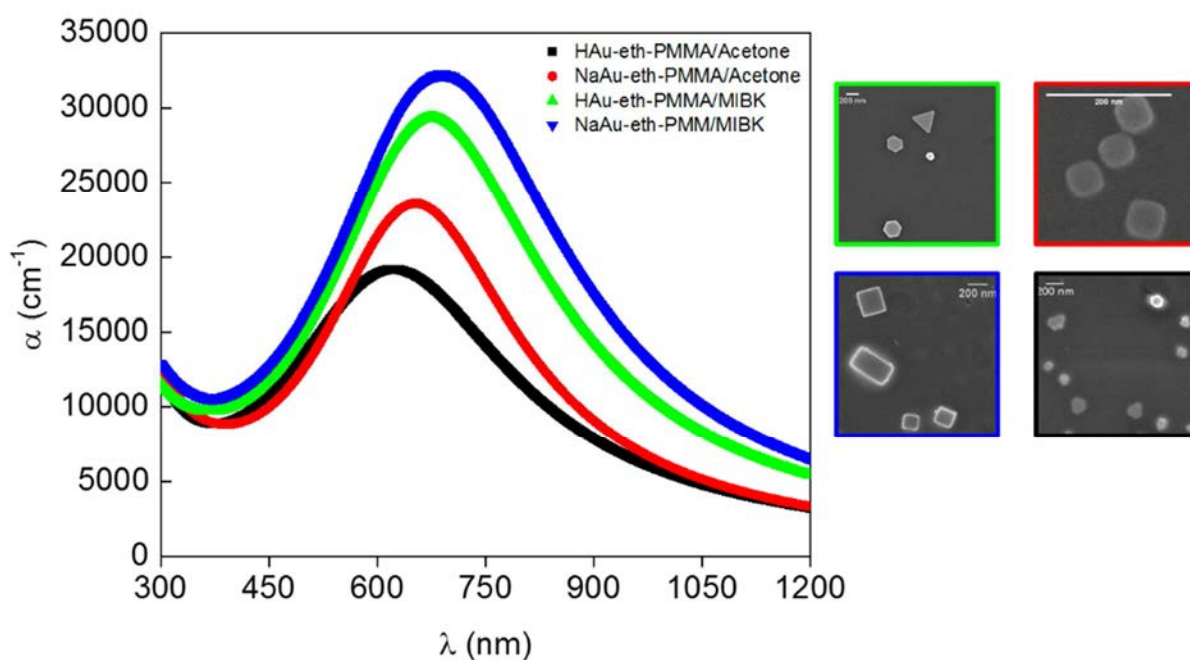


Fig. 62 UV-Vis absorption spectra of gold nanoparticles in four different samples prepared according to the experimental conditions displayed in the figure with their illustrated SEM images in the right side at scale bar of 200 nm. Samples prepared at same spin-coating parameters.

In summary, it should be pointed out that the samples prepared with high volatile PMMA solvent (acetone) produce high thickness which induces a better interaction of the light with the material without affecting the optical properties.

The optical properties were extracted and produced a localized absorption bands in VIS-NIR regions with a significant redshift from 620 to 690 nm.

This wide spectral range have been proven to be highly beneficial in sensing applications. [27],[29],[30]

4.3.2.2 Control the formation of non-cubic shapes: gold nanohexagons (GNHs) and gold nanotriangles (GNTs)

In the above study, we controlled the formation of uniform GNCs and we were able to synthesize poly-dispersed GNHs and poly-dispersed GNPs of sharp tips (GNRs and GNCs).

The formation of anisotropic GNPs (GNHs and GNTs) was controlled according to the simple synthetic adjustments which rely on the modification of some experimental parameters and on the growth rate of the formation as described in chapter 3. Hence, decreasing the growth rate via such adjustment boosts the formation of non-cubic shapes (GNHs and GNTs), knowing that GNCs have fast kinetic rate of formation as mentioned in chapter 3.

In this section, we will study the optical properties of non-cubic shapes such as monodispersed GNTs and GNHs after measuring their ellipsometric angles (Ψ and Δ).

Fig. 63 sums up the whole SPR spectra and the SEM images that will be carried in this study.

In this spectra, we can see a similar behavior of the absorbance peak despite the slight redshift in the position of the plasmon peak and that of their amplitude.

Accordingly, we will analyze these spectra in the following sections after performing the necessary SE measurements.

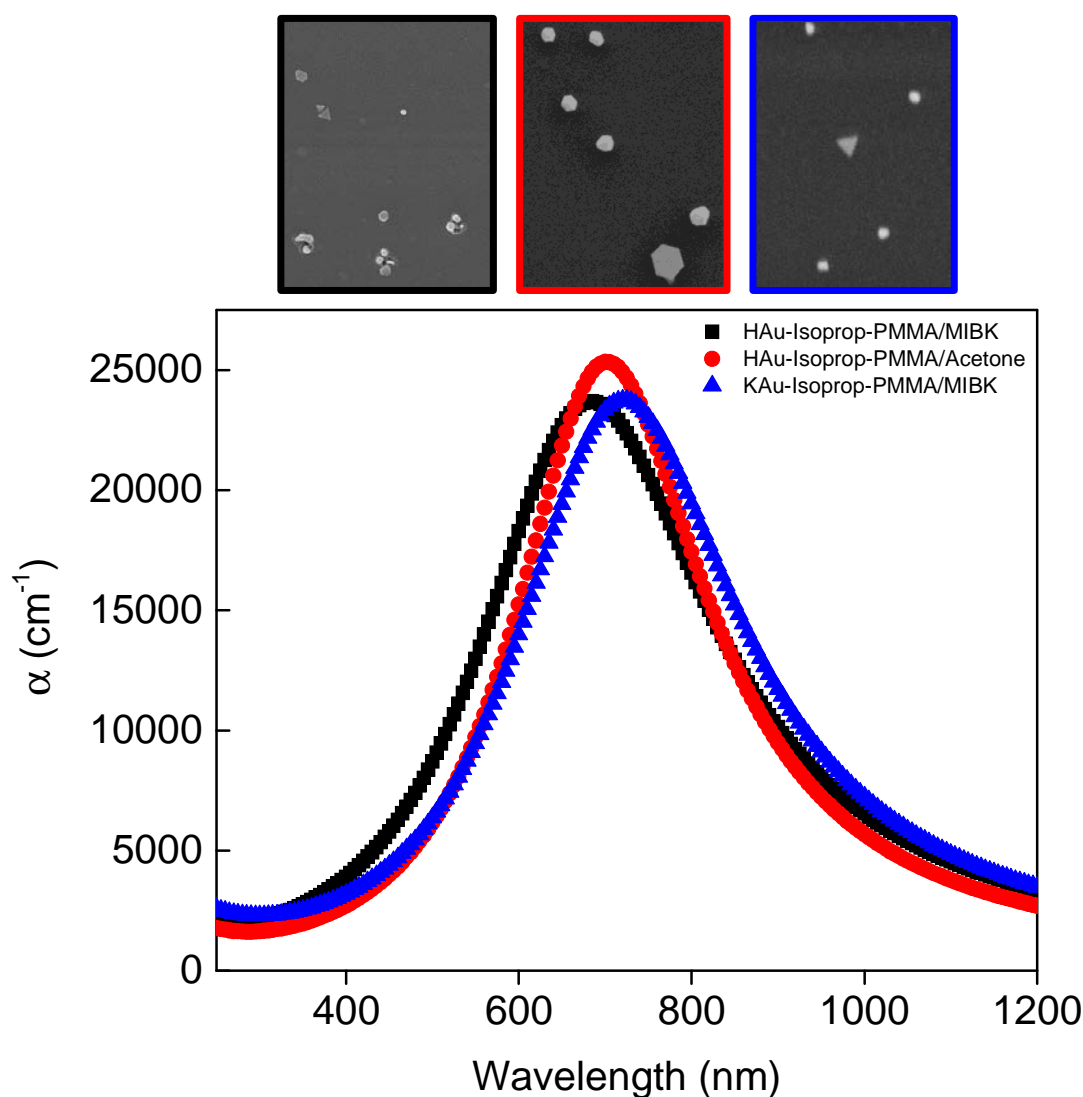


Fig. 63 Absorbance spectra showing the behavior of plasmon peak of monodispersed GNTs (blue spectrum), mono-dispersed GNHs (red spectrum) and poly-dispersed GNHs and GNTs (black spectrum). Samples prepared at same coating conditions and different gold precursors and PMMA solvents as presented in these spectra. The three insets (SEM images) correspond to various non-cubic shapes.

The SEM images in Fig. 64 show a high density of assemblies of GNPs for H_{Au}Cl₄ precursor which is prepared with acetone (b) and K_{Au}Cl₄ which is prepared with MIBK (c). In contrast, H_{Au}Cl₄ precursor with MIBK displays low density of GNPs (a).

We reported in chapter 3 that H_{Au}Cl₄ precursor with acetone has no control over GNPs, which is true in case the solvent of gold precursor is ethanol as used in the above study. Here, we used isopropanol since it allowed a better monodispersed nanoparticles (as discussed in chapter 3) as seen in Fig. 64. Therefore, we expect to have higher thickness values of the sample prepared with acetone compared to MIBK. The SEM image in Fig. 64 (c) shows a high density of GNPs for a sample prepared with K_{Au}Cl₄ precursor compared to Fig. 64 (a). We can deduce that K_{Au}Cl₄/Isopropanol have better repulsive interaction with PMMA/MIBK than H_{Au}Cl₄/Isopropanol. Thus, the thickness should be estimated to validate this conclusion.

We completed the SEM images by fitting the ellipsometric measurements as shown in Fig. 65.

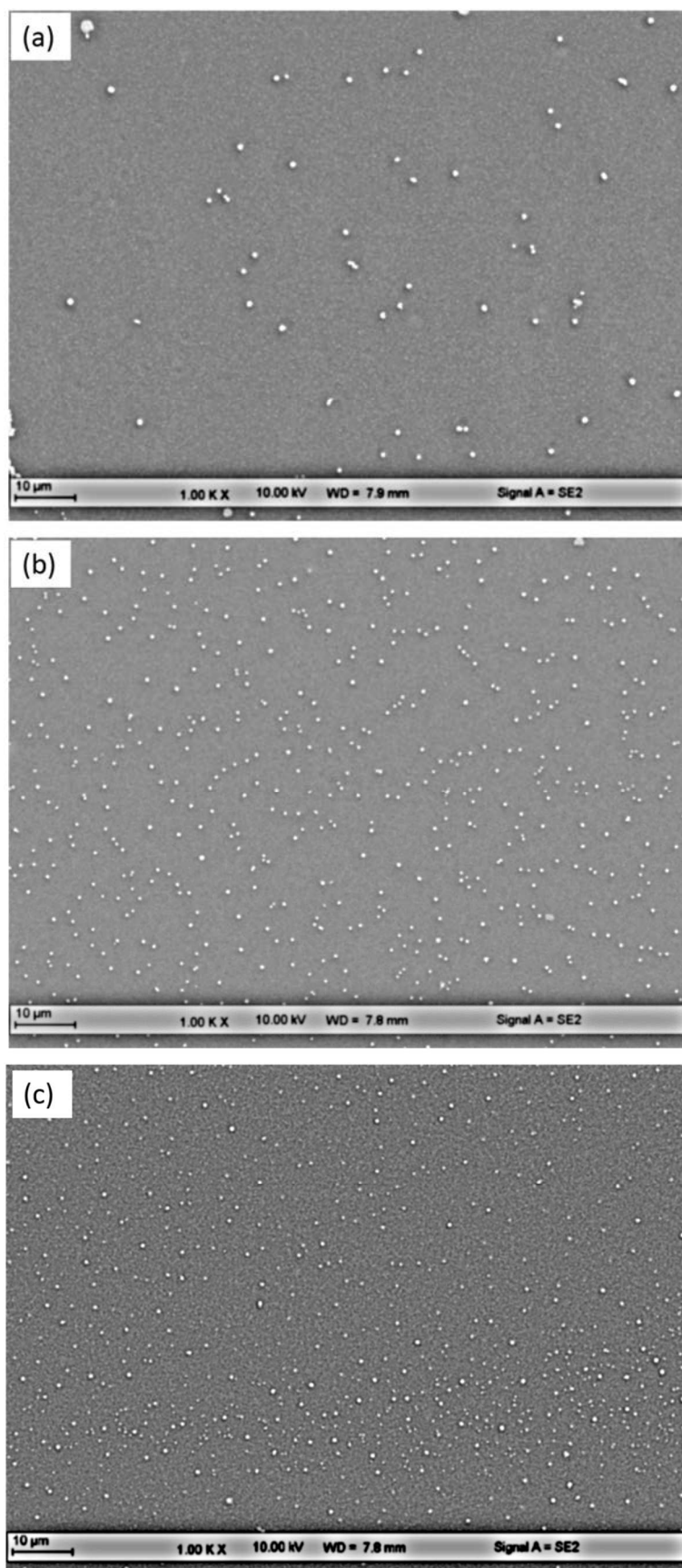


Fig. 64 SEM images of GNPs at large scan size. Samples (a) and (b) prepared with same gold precursor (HAuCl_4), and different PMMA solvents: (a) MIBK and (b) acetone. Sample (c) differs from (b) by the gold precursor which is KAuCl_4 . The three samples prepared at same coating conditions and with same gold precursor's solvent (isopropanol).

4.3.2.2.1 Ellipsometric measurements and modeling

The expected values of ellipsometric parameters are calculated and compared with the measured angles as seen in Fig. 65.

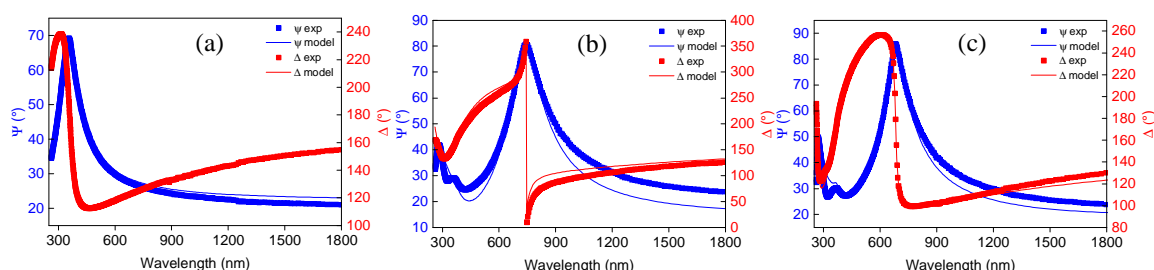


Fig. 65 Comparison between the measured and modeled ellipsometric spectra for GNPs of various shapes that correspond for samples which their SEM images are shown in Fig. 63 and Fig. 64. (a) Reflects poly-dispersed GNPs and GNTs, (b) presents the monodispersed GNPs and (c) contributes to monodispersed GNPs. Measurements are performed at incident angle 60° .

The comparison between the measured data and the calculated ones in Fig. 65 reveals a good fit despite the slight disagreement that was shown in the NIR region in the three samples (a, b and c).

Furthermore, Fig. 65 (b and c) displays a large wavelength shift for both Ψ and Δ values compared to Fig. 65 (a). This observation is contributed to the strong interaction of incident light with existed GNPs on the targeted sample of Fig. 65 (b-c). This shift is confirmed with the above SEM images in Fig. 64 (b-c) which exhibit high density of GNPs compared to the sample possessing low density of GNPs (Fig. 64 a). Accordingly, we found that the ellipsometric measurements are highly sensitive to the density of GNPs. Therefore, we expect to have a high thickness value of the PMMA film and more shifted optical constants (dielectric function and the absorption coefficient) in these two samples.

As a result, this fitting allows us to estimate the thickness of the PMMA film and the optical properties of these samples in the following part.

4.3.2.2.2 Extracting the thickness and the optical constants

A regression analysis of χ^2 (mean error) is minimized, so that the thickness and the optical constants can be determined. The thickness of PMMA film of the above samples is shown in Fig. 66.

By changing the gold precursor from HAuCl_4 into KAuCl_4 , a significant increase in the thickness of PMMA film from 72 nm to 155 nm is resulted. KAuCl_4 which is not highly soluble in isopropanol showed a lower volatility when MIBK is used, so that a high thickness value is

generated. Therefore, the repulsive interaction between KAuCl_4 and MIBK is higher than HAuCl_4 and MIBK as mentioned above. We stated before (chapter 2) that the difference in thickness values can be attributed to the effect of the matrix and polymer existing on the surface of the silicon substrate. Herein, GNPs prepared with HAuCl_4 /acetone display a high thickness value, which is 185 nm as illustrated in this figure. So, the ellipsometric measurements in Fig. 65 and the SEM images in Fig. 64 are verified. Based on the insets of the SEM images, we see clearly that monodispersed GNTs and GNHs have higher thickness values than poly-dispersed GNHs and GNTs.

Now, we will extract the optical constants of the dielectric function and that of the absorbance coefficient as given in the following figures (Fig. 67 & Fig. 68).

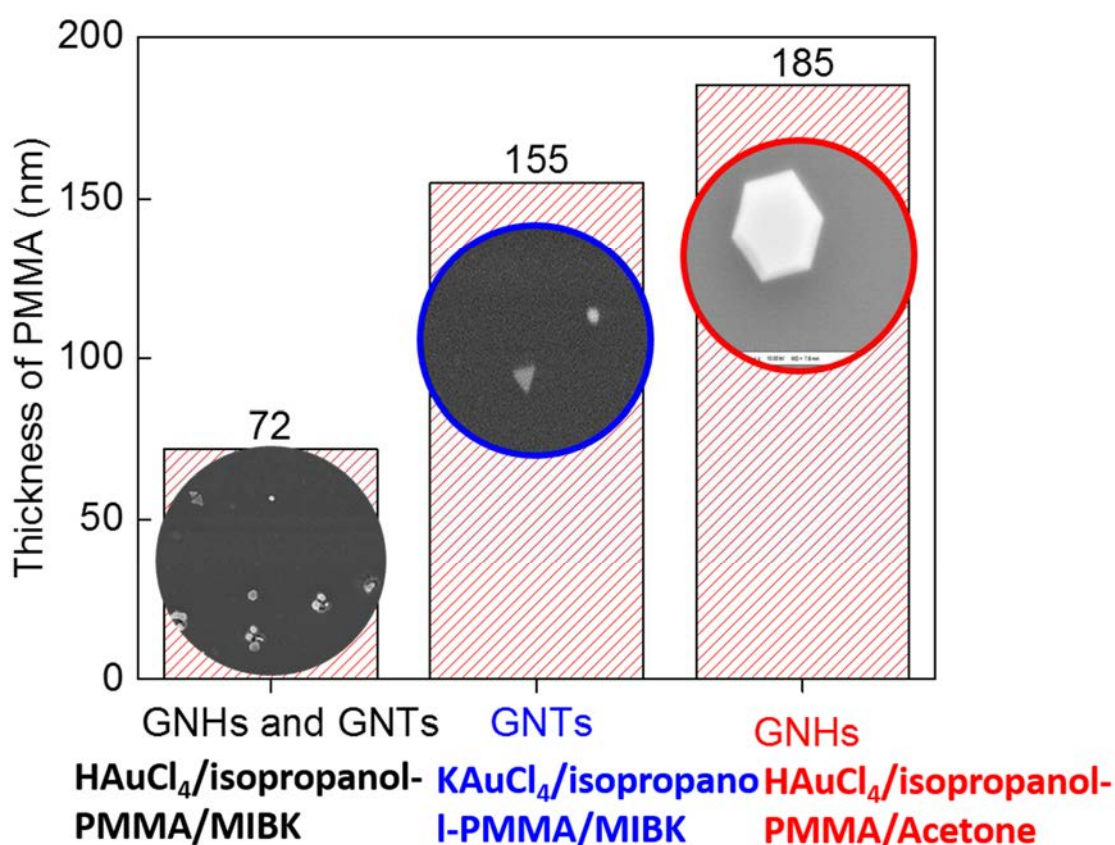


Fig. 66 Evolution of the thickness of PMMA film (nm) of the above three samples of GNPs. The insets show the various shapes of GNPs that can be obtained according to the presented experimental conditions.

The dielectric function spectra of the above three samples is shown in Fig. 67. The high thickness (185 nm) of GNHs that was obtained for HAuCl_4 with acetone was accompanied by the generation of an intense peak and red shift in the imaginary (ϵ_i) dielectric function spectra

(red spectrum) compared to the other sample that generated poly-dispersed GNHs and GNTs when prepared in MIBK (black spectrum).

In addition, the red spectrum displays higher amplitude in ϵ_i compared to the black spectrum which is attributed to a high density of GNPs that validates the SEM image seen in Fig. 64 (b). Meanwhile, the blue spectrum in Fig. 67 which refers to GNTs shows a less amplitude and a red shift in the wavelength compared to the red spectrum. The dielectric function spectra in Fig. 67 signify the presence of a strong absorption band in the NIR region as expected from the ellipsometric measurements (Fig. 65) knowing that the absorption band is highly sensitive to the dielectric constants of the surrounding medium, basically the imaginary part, where one can derive the absorbance band.

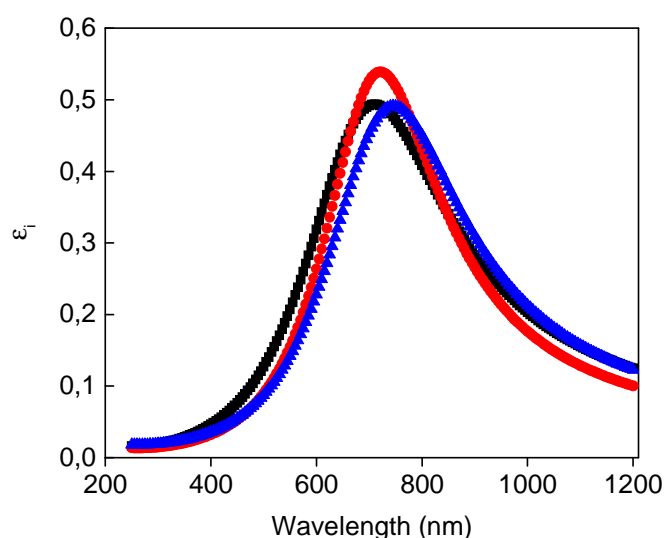


Fig. 67 Evolution of the dielectric function of imaginary (ϵ_i) part of the above three samples of GNPs. Black spectrum refers to poly-dispersed GNHs and GNTs, red spectrum contributes to monodispersed GNHs and the blue spectrum presents the monodispersed GNTs.

Fig. 68 demonstrates the absorbance spectra of the above samples with their SEM images. Based on the SEM images in Fig. 68 (a, c), we noticed that KAuCl_4 precursor forms monodispersed GNTs. In contrast, $\text{HAuCl}_4/\text{MIBK}$ forms a mixture of non-controlled GNHs and GNTs, where there is no control over the shape and the size of GNPs. That's why, we changed the gold precursor from HAuCl_4 into KAuCl_4 . Concerning these SEM images, we observed that the size of monodispersed GNTs (c) is smaller than that of the poly-dispersed GNHs and GNTs (a). The observed GNTs display sharp tips, so we expect to have a red shift in the SPR band.

Moreover, we reported previously that NaAuCl_4 precursor tends to form monodispersed GNCs in acetone, whereas here, HAuCl_4 tend to generate uniform GNHs with acetone. Thus, we

changed MIBK into acetone. Based on these images, we see clearly that the size of the monodispersed GNHs (b) is greater than that of the poly-dispersed GNHs and GNTs (a).

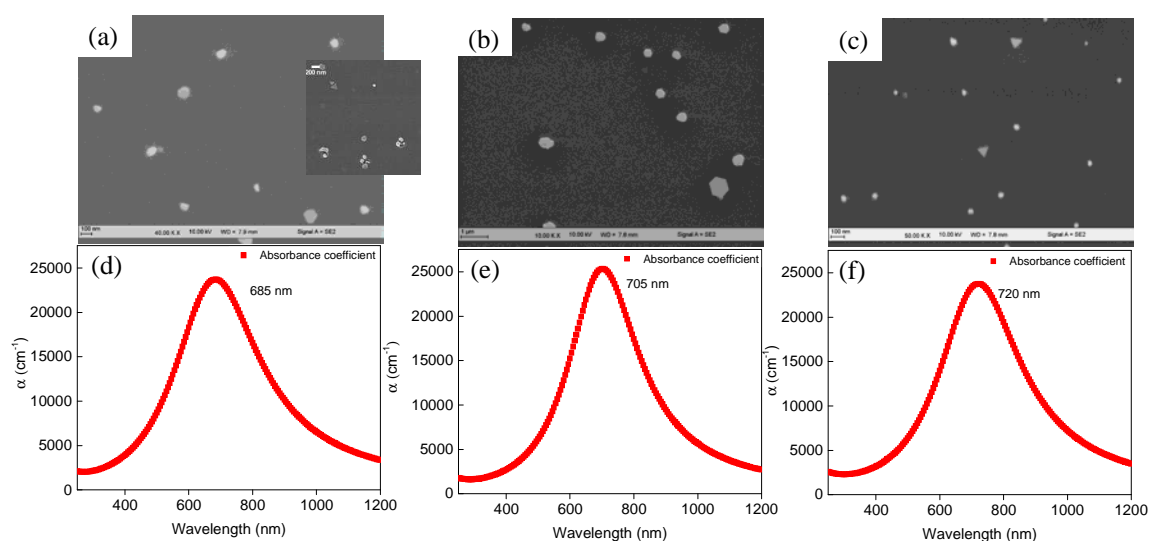


Fig. 68 The absorbance spectra in (d), (e) and (f) represent the samples for which their SEM images are shown respectively in (a), (b) and (c). (a and d) Correspond to HAuCl_4 precursor that results in the formation of poly-dispersed GNHs and GNTs in MIBK, (b and e) correspond to HAuCl_4 precursor that forms monodispersed GNHs in acetone and (c, f) correspond to KAuCl_4 precursor that yields to monodispersed GNTs in MIBK. The three samples were prepared by the same gold precursor's solvent (isopropanol) and in the same spin-coating parameters.

The red shift in the absorbance spectra in Fig. 68 validates the ϵ_i spectra that were obtained in Fig. 67 and the ellipsometric measurements in Fig. 65. It is known that the presence of the long wavelength peak in the visible-NIR spectra is a considerable remark for the presence of anisotropy in the gold nanoparticles such as GNHs and GNTs, where the increase in the edge length leads to a shift in their wavelengths. [31]

Based on the above figures (Fig. 64, Fig. 65, Fig. 66 and Fig. 67) and on the SEM image (Fig. 68 a), we found that HAuCl_4 /Isopropanol-PMMA/MIBK displays a low thickness value (72 nm) with high shape and size distribution and exhibits a plasmon peak at 685 nm. In contrast, monodispersed GNHs (Fig. 68 b) display narrow plasmon peak at 705 nm (spectrum e) with lower amplitude compared to the other sample (spectrum d). On the other hand, KAuCl_4 precursor (spectrum f) which contributes to the presence of uniform GNTs displays a red shift at 720 nm and a decrease in its amplitude with respect to the KAuCl_4 precursor (spectrum e). Besides, it is known that the small triangular GNPs exhibit a strong SPR band at 615 nm. [32] Thus, the plasmon band at 685 nm can be attributed either to the presence of larger sized GNTs or to the plasmon peak of GNHs which is very similar to that obtained in the other spectra (705

nm). Actually, it was not easy to assign the obtained absorption peak at 685 nm for sample containing a mixture of shapes (GNHs and GNTs) over a wide range of size and shape.

Moreover, it is known that several bands of GNTs can be obtained in the visible and near infrared regions by increasing the side length of these GNTs. [33] Accordingly, we admit that each size has its own plasmon peak. Thus, we can't assign the observed peak (720 nm) to a specific size. So, the redshift from 685 to 705 nm may be attributed to the increase in the size of GNPs, the increase in the density of GNPs, the change in the shape of GNPs and the coupling between high densities of GNPs on the surface of the Si substrate.

It was reported that the scattering spectra of the Nanotriangles (NTs) at variable polarizations present two different plasmon modes for isosceles NTs and one plasmon band for equilateral NTs. Equilateral GNTs (50 nm edge length) display a single plasmon band at 700 nm. [34] According to chapter 3, we found that the obtained GNTs are monodispersed, where they have the same edge length. In this sense, we can't attribute the obtained single plasmon peak to the fact that the GNTs are equilateral, because the size of GNTs is greater than 50 nm. Nevertheless, the two Lorentz oscillators based model is not able to show the other plasmon modes, knowing that the corners of the GNTs also have a plasmon mode. Thus, we can attribute the obtained redshift to the effect of tips (corners) which can be highly enhanced in the GNTs according to other researchers. [35] Moreover, the SPR peak at 720 nm could be also attributed to the influence of longitudinal oscillations of the electron cloud that incorporate the edge length of the formed small GNTs (~80 nm edge length) which seems more compatible to our results. This observation fits the DDA simulations performed in water on Au prisms of edge length 50-100 nm. [28],[36]

In summary, based on this study, we found that the shape control is highly relevant to tune the plasmon band in wide spectral range (VIS & NIR).

The gold precursor as well as the solvent of the PMMA is a significant candidate to carry on the shape control of the GNPs.

The ellispometric measurements were sensitive to the high thickness values of PMMA film, the density of GNPs and to the optical properties of GNPs loaded in PMMA film.

The difference in the absorbance spectra can be attributed either to the effect of the shape (GNTs possess longer wavelengths than GNHs as described by Mock et al. [37]) or to the effect of the size, because GNHs display larger size in comparison to that of GNTs. But the resulted three absorbance spectra of the above study didn't demonstrate a significant shift in the plasmon band. As a result, the absorbance spectra is sensitive to the size and the shape of the GNPs and

dielectric function of the surrounding medium. In addition, the increase in the amplitude of the absorbance spectra is related to the increase in the density of GNPs.

It was difficult to compare between these complex three samples. The possible presence of the different plasmon modes is not considered in our model. Going further in improving this model to take into account the shape of GNPs will certainly be an interesting investigation for future work.

4.4 Conclusion

In this chapter, we have shown that spectroscopic ellipsometry (SE) is a valuable tool to determine the complete optical responses of the GNPs embedded in PMMA layers. The two Lorentz oscillators model was found to be a good method allowing the investigation of the various optical constants such as the dielectric function and the absorption coefficient of such complex composite layers. In addition, SE was used for the verification of the homogeneity of the deposited layers by spin-coating and for the determination of the thickness values. SE measurements are highly sensitive to the thickness as well to the density of GNPs.

In this study, we have also shown that the ER parameter has a direct effect on the thickness of the PMMA film, the volume fraction or the density of the GNPs and the size distribution (size of GNPs). Accordingly, we found that the speed 5000 rpm acts as a suitable mechanical parameter to enhance the synthesis of GNPs where high number of smaller GNCs are obtained, thus a strong SPR band is achieved.

The SPR band was found to be more sensitive to the size and the shape of the GNPs as well to the dielectric function of the surrounding medium but not to the thickness of the PMMA layer. Moreover, the solvent of the PMMA plays a significant role in the structuring mechanism, so it has a strong impact on the absorption band. In comparison to MIBK, acetone favors the reduction of GNPs and yields higher values of thickness, also it can be considered as a good solvent for PMMA to synthesize monodispersed GNPs.

We have also found that upon adjusting the synthesis method such as modifying the gold precursor and the solvent of the gold precursor are significant candidates to explore the shape control of GNPs and control the optical responses (SPR band and dielectric function).

We recognized that the conversion of a shape from GNCs into non GNCs has a more significant impact on tuning the SPR bands in a wide spectral range than increasing the diameter of the GNPs. On the other hand, the ellipsometric measurements as well the optical properties of the

hexagonal and triangular GNPs have similar behavior, where the slight variations were linked to the change in their size.

The response of the two plasmon mode of the produced anisotropic GNPs was not seen in the above studies due to the usage of only two oscillators, one for GNPs and another for PMMA. Even though, we deduce that the spectroscopic ellipsometry acts as a convenient optical tool for determining the thickness of the composite layer and the optical properties of the embedded GNPs either at low volume fractions of GNPs as obtained for GNHs and GNTs or at low thickness of PMMA film as generated in MIBK solvent.

4.5 References

- [1] Zhang, J. Z. (2009). Optical properties and spectroscopy of nanomaterials. World Scientific Publishing London.
- [2] Azzam, R. M. A., & Bashara, N. M. (1977). Ellipsometry and polarized light. North-Holland, Amsterdam.
- [3] Boulouz, A., Naciri, A. E., Pascal-Delannoy, F., Sorli, B., & Koutti, L. (2009). Spectroscopic ellipsometry study of $x\text{PbO}-(1-x)\text{TiO}_2$ thin films elaborated by mixed reactive thermal co-evaporation. *Journal of Physics D: Applied Physics*, 42(24), 245304.
- [4] Battie, Y., Izquierdo-Lorenzo, I., Resano-Garcia, A., Naciri, A. E., Akil, S., Adam, P. M., & Jradi, S. (2016). How to determine the morphology of plasmonic nanocrystals without transmission electron microscopy?. *Journal of Nanoparticle Research*, 18(8), 2.
- [5] Wang, X., Ehrhardt, K., Tallet, C., Warenghem, M., Baron, A., Aradian, A., ... & Ponsinet, V. (2017). Hyperbolic-by-design self-assembled metamaterial based on block copolymers lamellar phases. *Optics & Laser Technology*, 88, 85-95.
- [6] Losurdo, M., Bergmair, M., Bruno, G., Cattelan, D., Cobet, C., de Martino, A., ... & Gajic, R. (2009). Spectroscopic ellipsometry and polarimetry for materials and systems analysis at the nanometer scale: state-of-the-art, potential, and perspectives. *Journal of Nanoparticle Research*, 11(7), 1521-1554.
- [7] Naciri, A. E., Miska, P., Keita, A. S., Battie, Y., Rinnert, H., & Vergnat, M. (2013). Optical properties of uniformly sized silicon nanocrystals within a single silicon oxide layer. *Journal of nanoparticle research*, 15(4), 1538.
- [8] Oates, T. W. H., Wormeester, H., & Arwin, H. (2011). Characterization of plasmonic effects in thin films and metamaterials using spectroscopic ellipsometry. *Progress in Surface Science*, 86(11-12), 328-376.
- [9] Oates, T. W. H., & Mücklich, A. (2005). Evolution of plasmon resonances during plasma deposition of silver nanoparticles. *Nanotechnology*, 16(11), 2606.
- [10] Oates, T. W. H. (2006). Real time spectroscopic ellipsometry of nanoparticle growth. *Applied physics letters*, 88(21), 213115.
- [11] Oates, T. W. H., & Christalle, E. (2007). Real-time spectroscopic ellipsometry of silver nanoparticle formation in poly (vinyl alcohol) thin films. *The Journal of Physical Chemistry C*, 111(1), 182-187.

- [12] Battie, Y., Destouches, N., Chassagneux, F., Jamon, D., Bois, L., Moncoffre, N., & Toulhoat, N. (2011). Optical properties of silver nanoparticles thermally grown in a mesostructured hybrid silica film. *Optical Materials Express*, 1(5), 1019-1033.
- [13] Wan, D., Chen, H. L., Lin, Y. S., Chuang, S. Y., Shieh, J., & Chen, S. H. (2009). Using spectroscopic ellipsometry to characterize and apply the optical constants of hollow gold nanoparticles. *ACS nano*, 3(4), 960-970.
- [14] Tompkins, H., & Irene, E. A. (2005). *Handbook of ellipsometry*. William Andrew.
- [15] Novotny, L., & Hecht, B. (2012). *Principles of nano-optics*. Cambridge university press.
- [16] Battie, Y., Resano-Garcia, A., Chaoui, N., Zhang, Y., & En Naciri, A. (2014). Extended Maxwell-Garnett-Mie formulation applied to size dispersion of metallic nanoparticles embedded in host liquid matrix. *The Journal of chemical physics*, 140(4), 044705.
- [17] Link, S., Mohamed, M. B., & El-Sayed, M. A. (1999). Simulation of the optical absorption spectra of gold nanorods as a function of their aspect ratio and the effect of the medium dielectric constant. *The Journal of Physical Chemistry B*, 103(16), 3073-3077.
- [18] Keita, A. S., Naciri, A. E., Delachat, F., Carrada, M., Ferblantier, G., & Slaoui, A. (2010). Spectroscopic ellipsometry investigation of the optical properties of nanostructured Si/SiN_x films. *Journal of Applied Physics*, 107(9), 093516.
- [19] Myroshnychenko, V., Rodríguez-Fernández, J., Pastoriza-Santos, I., Funston, A. M., Novo, C., Mulvaney, P., ... & de Abajo, F. J. G. (2008). Modelling the optical response of gold nanoparticles. *Chemical Society Reviews*, 37(9), 1792-1805.
- [20] Voué, M., Dahmouchène, N., & De Coninck, J. (2011). Annealing of polymer films with embedded silver nanoparticles: Effect on optical properties. *Thin Solid Films*, 519(9), 2963-2967.
- [21] Guyot, C., & Voué, M. (2007). Optical behavior of poly-(vinyl) alcohol films embedding silver nanoparticles: a statistical analysis of the film thickness effect. *J. Nanosci. Nanotechnol*, 7, 1.
- [22] Marquardt, D. W. (1963). An algorithm for least-squares estimation of nonlinear parameters. *Journal of the society for Industrial and Applied Mathematics*, 11(2), 431-441.
- [23] Njoki, P. N., Lim, I. I. S., Mott, D., Park, H. Y., Khan, B., Mishra, S., ... & Zhong, C. J. (2007). Size correlation of optical and spectroscopic properties for gold nanoparticles. *The Journal of Physical Chemistry C*, 111(40), 14664-14669.
- [24] Jana, N. R., Gearheart, L., & Murphy, C. J. (2001). Seed-mediated growth approach for shape-controlled synthesis of spheroidal and rod-like gold nanoparticles using a surfactant template. *Advanced Materials*, 13(18), 1389.
- [25] Link, S., & El-Sayed, M. A. (1999). Size and temperature dependence of the plasmon absorption of colloidal gold nanoparticles. *The Journal of Physical Chemistry B*, 103(21), 4212-4217.
- [26] Hong, S. W., Wang, J., & Lin, Z. (2009). Evolution of ordered block copolymer serpentine into a macroscopic, hierarchically ordered web. *Angewandte Chemie International Edition*, 48(44), 8356-8360.
- [27] Sriram, M., Zong, K., Vivekchand, S. R. C., & Gooding, J. J. (2015). Single nanoparticle plasmonic sensors. *Sensors*, 15(10), 25774-25792.

- [28] Verma, M., Kedia, A., Newmai, M. B., & Kumar, P. S. (2016). Differential role of PVP on the synthesis of plasmonic gold nanostructures and their catalytic and SERS properties. *RSC Advances*, 6(83), 80342-80353.
- [29] Willets, K. A., & Van Duyne, R. P. (2007). Localized surface plasmon resonance spectroscopy and sensing. *Annu. Rev. Phys. Chem.*, 58, 267-297.
- [30] Lv, Y., Qin, Y., Svec, F., & Tan, T. (2016). Molecularly imprinted plasmonic nanosensor for selective SERS detection of protein biomarkers. *Biosensors and Bioelectronics*, 80, 433-441.
- [31] Shankar, S. S., Rai, A., Ahmad, A., & Sastry, M. (2005). Controlling the optical properties of lemongrass extract synthesized gold nanotriangles and potential application in infrared-absorbing optical coatings. *Chemistry of Materials*, 17(3), 566-572.
- [32] Chu, H. C., Kuo, C. H., & Huang, M. H. (2006). Thermal aqueous solution approach for the synthesis of triangular and hexagonal gold nanoplates with three different size ranges. *Inorganic chemistry*, 45(2), 808-813.
- [33] Félidj, N., Grand, J., Laurent, G., Aubard, J., Levi, G., Hohenau, A., ... & Krenn, J. R. (2008). Multipolar surface plasmon peaks on gold nanotriangles. *The Journal of chemical physics*, 128(9), 094702.
- [34] Trügler, A. (2011). Optical properties of metallic nanoparticles. na.
- [35] Sonntag, M. D., Klingsporn, J. M., Zrimsek, A. B., Sharma, B., Ruvuna, L. K., & Van Duyne, R. P. (2014). Molecular plasmonics for nanoscale spectroscopy. *Chemical Society Reviews*, 43(4), 1230-1247.
- [36] Shuford, K. L., Ratner, M. A., & Schatz, G. C. (2005). Multipolar excitation in triangular nanoprisms. *The Journal of chemical physics*, 123(11), 114713.
- [37] Mock, J. J., Barbic, M., Smith, D. R., Schultz, D. A., & Schultz, S. (2002). Shape effects in plasmon resonance of individual colloidal silver nanoparticles. *The Journal of Chemical Physics*, 116(15), 6755-6759.

5 Summary, conclusions and perspectives

5.1 Summary and conclusions

The work presented in this thesis demonstrates a free-surfactant nanofabrication strategy and focuses on the shape control of gold nanoparticles, and their plasmonic properties. Through this novel synthesis, the formation of uniform gold nanocubes as well as gold nanohexagons and gold nanoprisms, was possible without the usage of any surfactant or reducing agent. Particularly, the thesis introduces a cheap and a facile one-step fabrication process based on polymer self-assembly. Hence, this new strategy of synthesis combines the advantages of bottom-up and top-down approaches.

The experimental parameters including the solvent evaporation rate, the concentration of metal precursor, ratio of solvent to non-solvent, solvent of gold precursor and that of polymer, the type of the metal precursor and the surface chemistry (functionalities and conductivity), are the key factors in the growth mechanism of GNPs.

In chapter 2, we synthesized mono-dispersed gold nanocubes using a simple one-step method. We reported an important red shift in the plasmonic band from 540 to 650 nm by using ellipsometry. The red shift was linked to the strong interaction between the nanoparticles separated by small interparticle distances. Gold nanocubes have been evaluated as ultrasensitive SERS sensors showing high chemical enhancement. SERS enhancement factor of 10^9 was determined for the 4,4-bipyridine, which matches with the values of the ultrasensitive SERS substrates reported in the literature.

Chapter 3 reveals the rich nature of surfactant-free shape-controlled synthesis as well as the utility of the substrate-based platform in defining growth strategies. Through this chapter, we found that varying solvents and metal precursors allows change in the growth kinetics of gold nanoparticles. In this context, the silicon electrons bounded to the counter ions including K^+ , H^+ and Na^+ of the gold precursor lead to slow, moderate, and fast kinetics, respectively. Slow kinetics was achieved by $KAuCl_4$ combination and gave rise to triangular gold nanoprism generated through epitaxial deposition on just a small portion of a single $\{100\}$ Au facet followed by the propagation of a rapid growth front away from the seed. Moderate kinetics allowed by $HAuCl_4$ resulted in hexagonal geometry realized through layer-by-layer deposition of Au on all $\{100\}$ equivalent seed facets followed by the overgrowth of all remaining facets. Fast kinetics allowed by $NaAuCl_4$ produced cubic and rectangular morphologies, where the overgrowth more closely follows the topography of the underlying seed. In addition, we found

that well-defined structures (sharp edges) of GNPs require the control of the solvent's evaporation rate and the solvent's type.

In **chapter 4**, we have shown that the two Lorentz oscillators model was found to be a good method for the investigation of the various optical constants such as the dielectric function and the absorption coefficient of such complex composite layers. In addition, SE was used for the verification of the homogeneity of the deposited layers by spin-coating and for the determination of the thickness values. We found that SE measurements are highly sensitive to the thickness as well to the density of GNPs. The spectroscopic ellipsometry acts as a convenient optical tool for determining the thickness of the composite layer and the optical properties of the embedded GNPs either at low volume fractions of GNPs as obtained for GNHs and GNTs or at low thickness of PMMA film as generated in MIBK solvent

5.2 Future work and perspectives

The work introduced in this thesis represents a step forward in the current fabrication processes of nanomaterials which could be beneficial for catalysis and biosensing because of the promising results obtained on shape control that's crucial for these applications in particular.

With respect to the synthesis method, several aspects could be further explored. Further experimental studies including the control of the spin-coating parameters, changing the substrate and the molecular weight of the PMMA, are necessary in the future, in order to attain a better control on the monodispersity of the obtained geometries (gold nanoprisms and gold nanohexagons), as achieved in chapter 2 for gold nanocubes.

The presented new approach can be also useful to incorporate a variety of inorganic metallic salts into the PMMA vesicles. Thus, the fabricated GNCs are promising to fabricate multifunctional materials (Plasmonic, photoluminescent, etc.) and bimetallic systems (Au-Ag, etc...). We started working on bimetallic systems and we obtained a material of core-shell, where the core displays the AuNPs and the shell presents Nanorings of AgNPs. (see Fig. 73 and Fig. 74 in appendix).

SERS results could be promising for biosensing applications especially diseases diagnosis that requires such a higher sensitivity (10^{-12} M) as obtained in chapter 2. Therefore, we need to go further in SERS experiments by detecting few number of bacteria after selection of the suitable morphology. Moreover, further SERS measurements are required to understand the role of shape on the sensing features of the obtained substrates.

The good agreement between experimental ellipsometry measurements and the model ones in chapter 4 is promising to establish a model that can adopt other morphologies than spherical (nanoprisms and nonohexagons).

Appendix

First, knowing that the synthesis method is substrate-mediated, changing the substrate could change the growth mechanism. For this aim, we have tested the influence of ITO substrates (see Fig. 71 and Fig. 72).

Second, we varied the concentration of the metal precursor (KAuCl_4 or HAuCl_4) in order to change the size of GNPs and to find the critical concentration of Au^{3+} that can form single shape of GNPs (gold nanoprism and nanohexagons) as made in chapter 2 for NaAuCl_4 when we obtained monodispersed GNCs. (see Fig. 69)

Third, we changed the molecular weight of PMMA as seen in Fig. 75 in the appendix. Here, the PMMA can serve as a directing agent in the structuring mechanism. Thus, we need to go further in this study to control the formation of other morphologies (e.g. GNRs).

We controlled the formation of monodispersed GNCs of uniform size and shape. In addition, we were able to form gold nanoprisms, GNTs and GNHs, so it will be interesting to go further in controlling the monodispersity of these morphologies through adjusting the speed of evaporation (as seen in Fig. 70), the type of substrate and the molecular weight of the PMMA. Consequently, we can find the best conditions which we can yield in high density of well-defined morphologies of gold nanoprisms and GNHs.

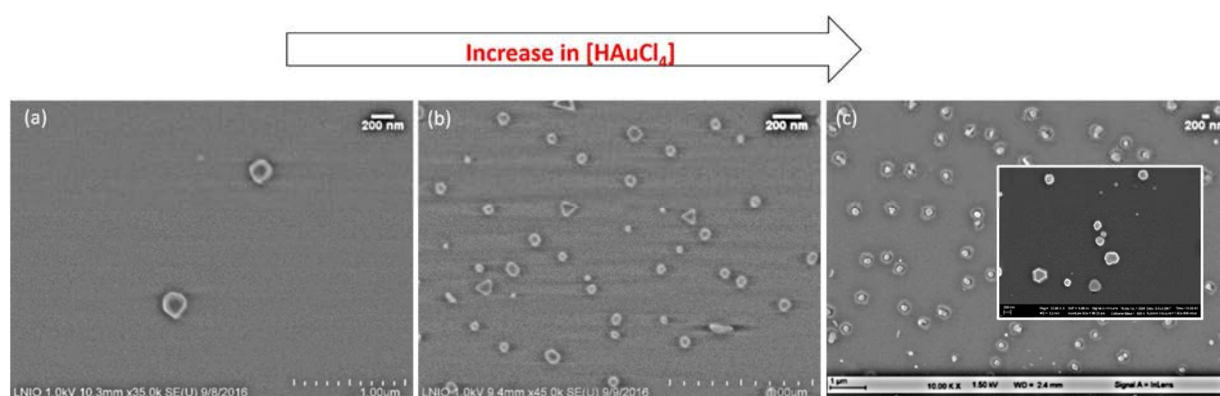


Fig. 69 The SEM images show the increase in the concentration of HAuCl_4 precursor. (a) 10 mM, (b) 50 (mM) and (c) 100 mM. The samples prepared at the same spin-coating conditions.

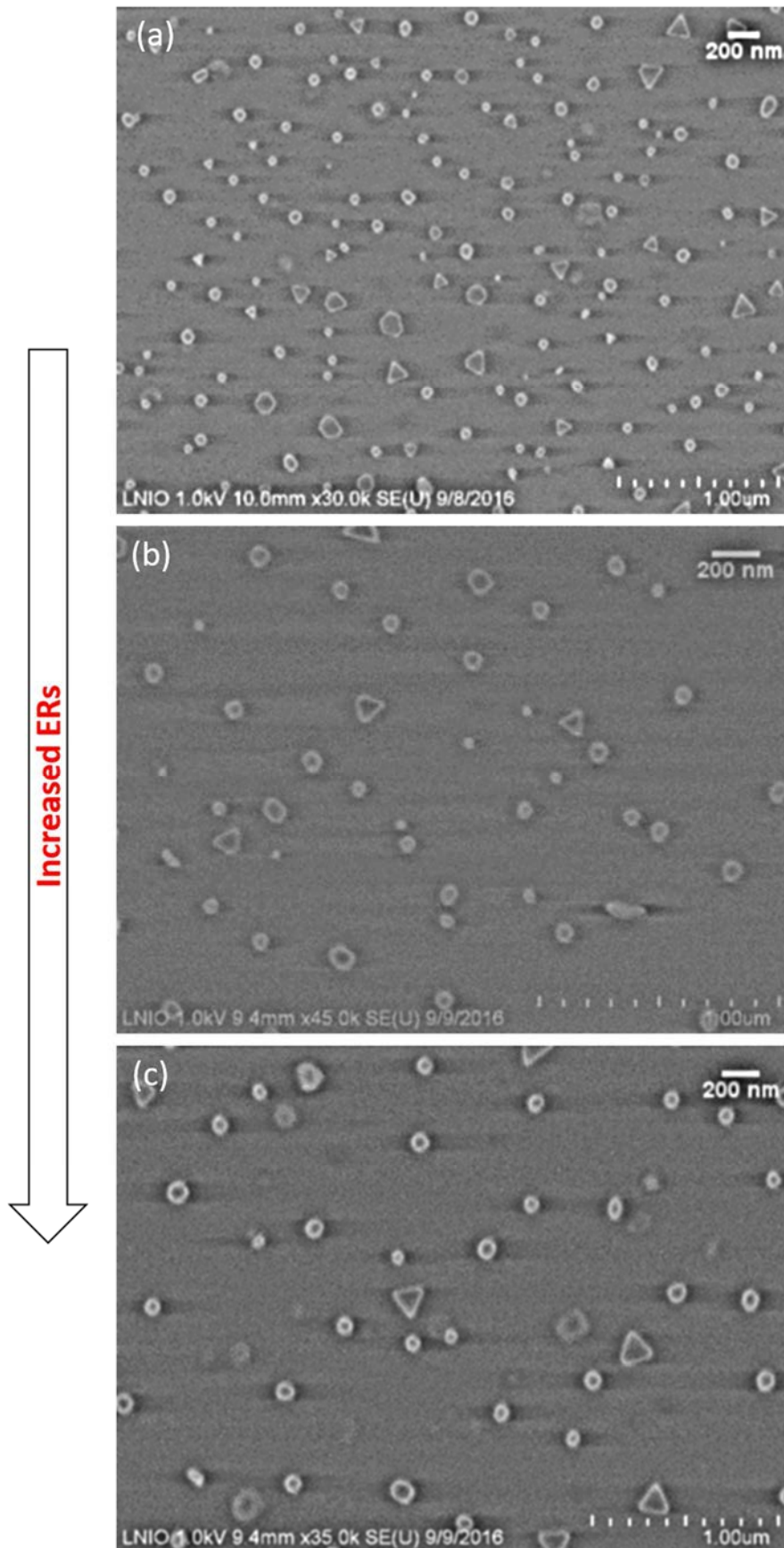


Fig. 70 The SEM images show the increase in the speed of spin-coating for 50 mM HAuCl₄. Samples were prepared on Si-As substrates.

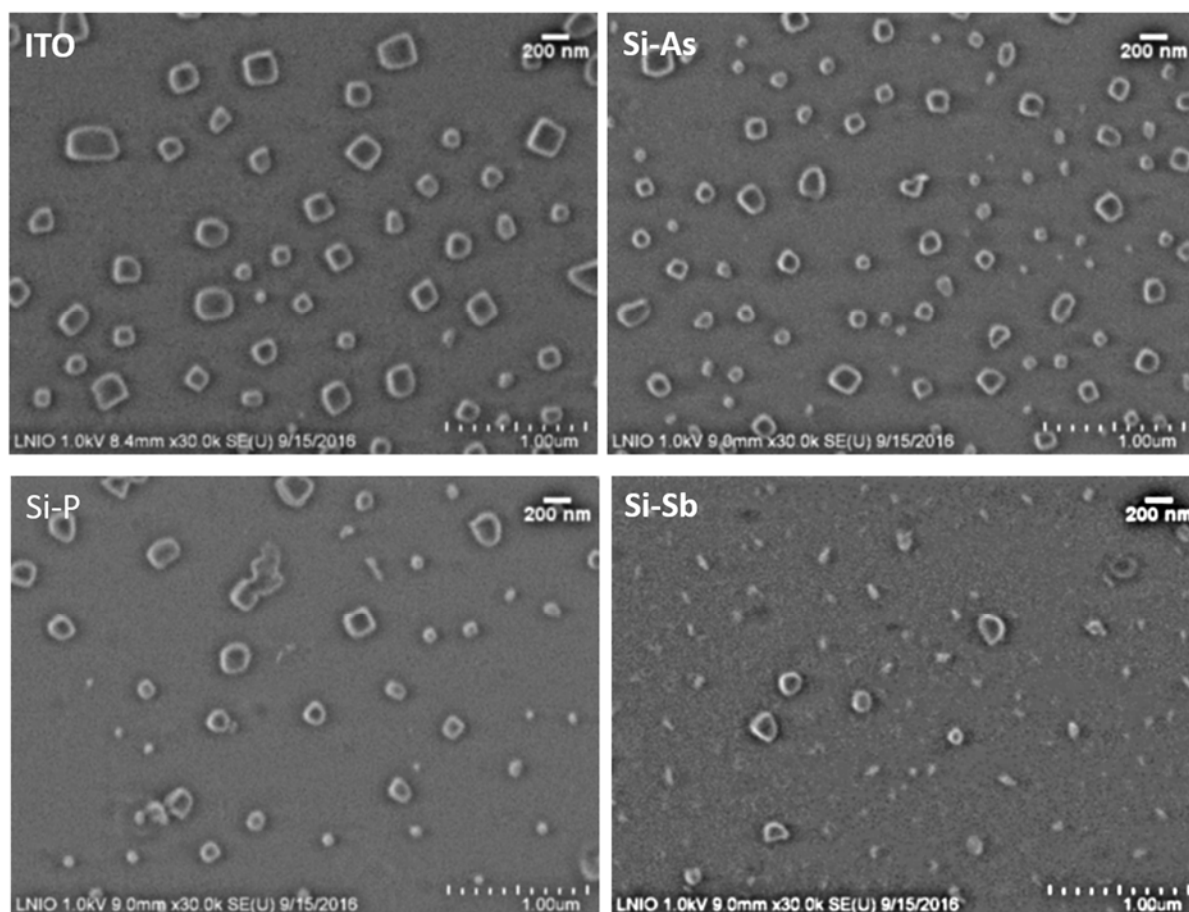


Fig. 71 The SEM images show the influence of changing the substrate of 50 mM NaAuCl₄. Samples prepared at the same spin-coating conditions.

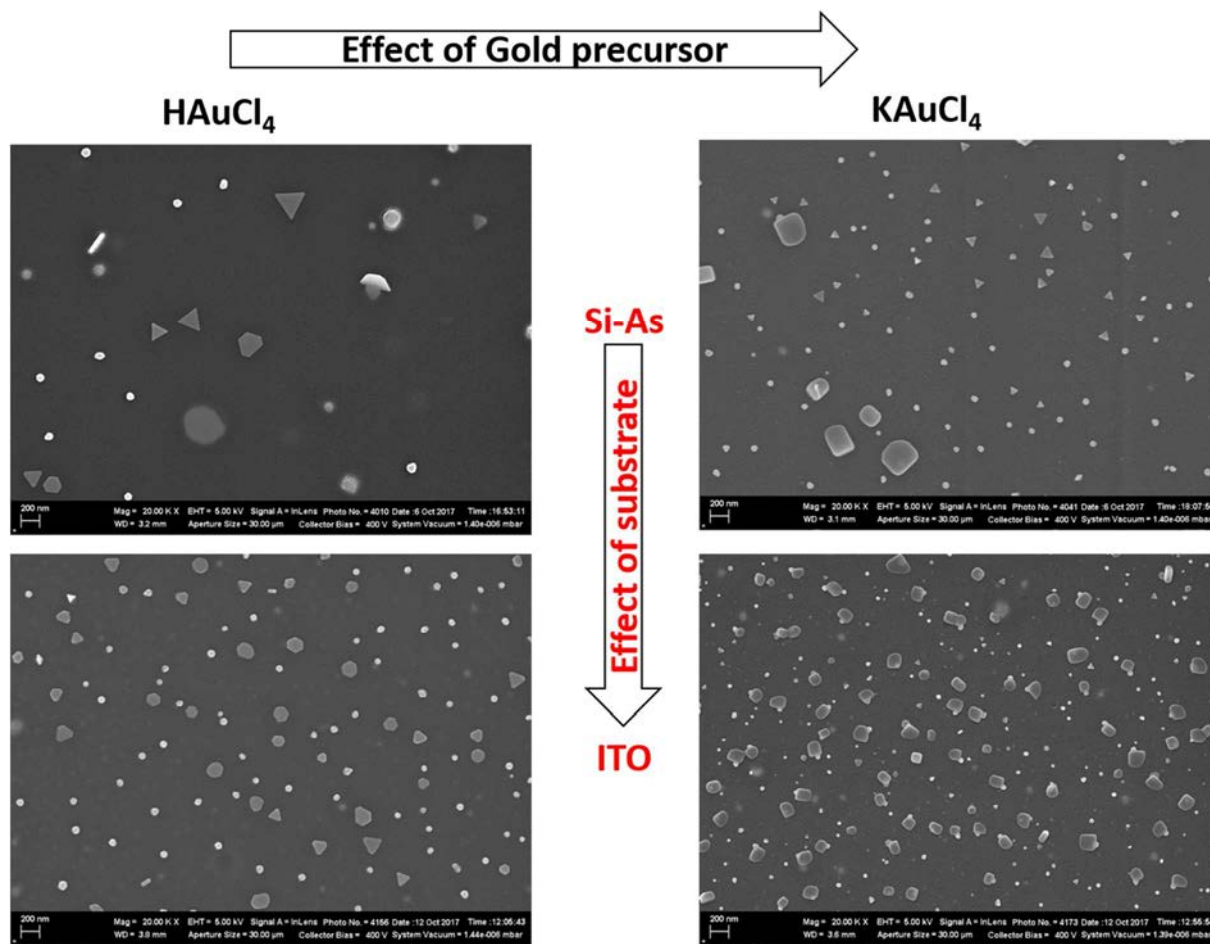


Fig. 72 The SEM images show the influence of changing the substrate from Si-As to ITO in 60 mM of HAuCl_4 and KAuCl_4 precursors. The Samples prepared at same spin-coating conditions.

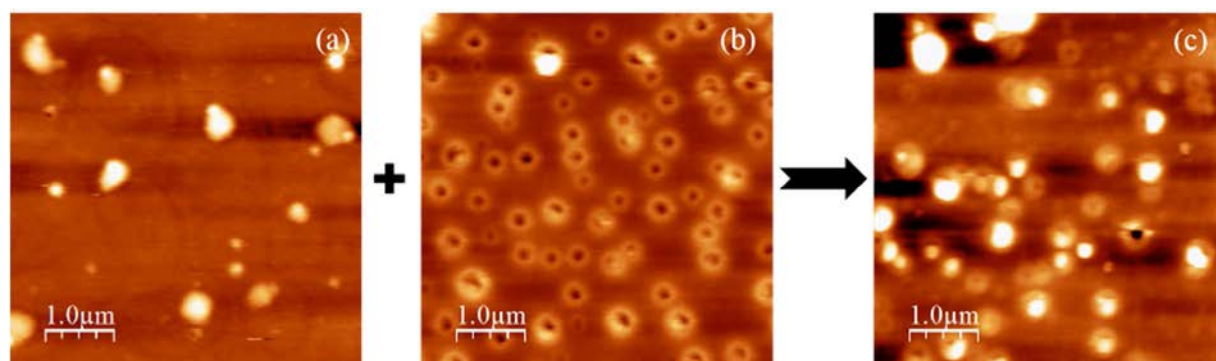


Fig. 73 AFM images of bimetallic system of Au and Ag NPs. (a) first layer of AuNPs (40 mg of Au/Isopropanol-PMMA/MIBK), (b) Second layer of AgNPs (20 mg of Ag/Isopropanol-PMMA/MIBK) and (c) highlights two layers of Au-Ag NPs.

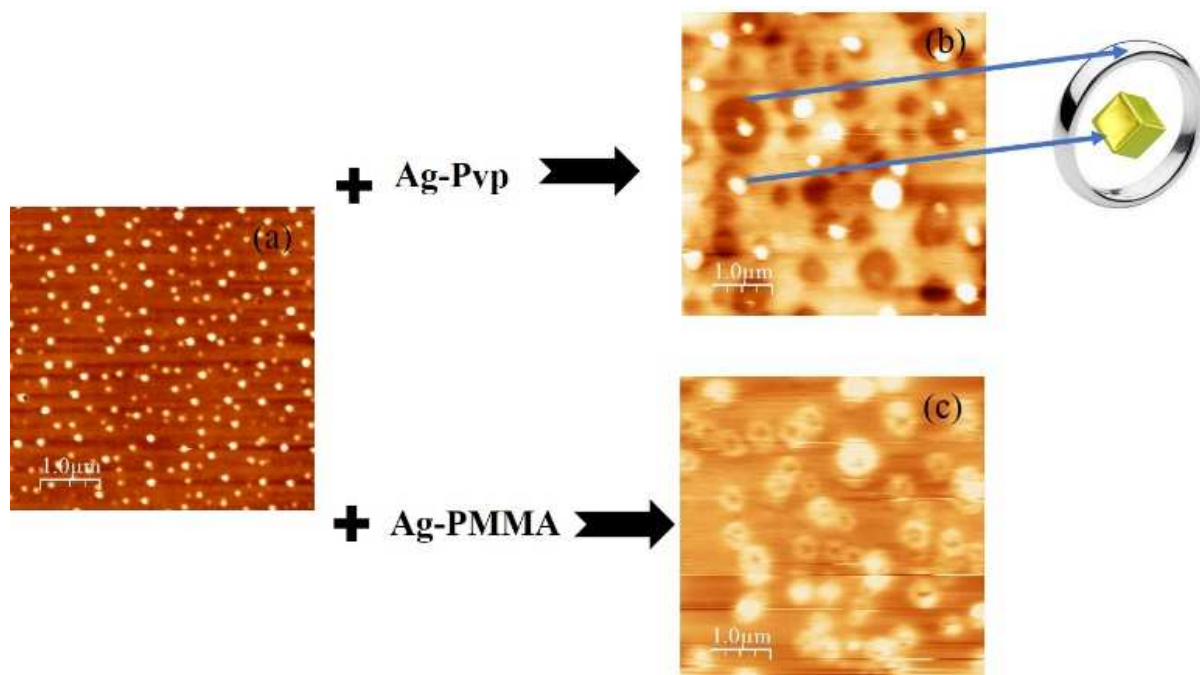


Fig. 74 (a) AFM image of the first layer of AuNPs (20mg Au/ethanol-PMMA/MIBK), (b) bimetallic material of Au-Ag using 20mg of Ag/PVP and (c) bimetallic system of Au-Ag using 20 mg of Ag/Ethanol-PMMA/MIBK). The inset shows a bimetallic system of Au-Ag NPs that demonstrates a core-shell identity. Samples prepared at the same spin-coating parameters.

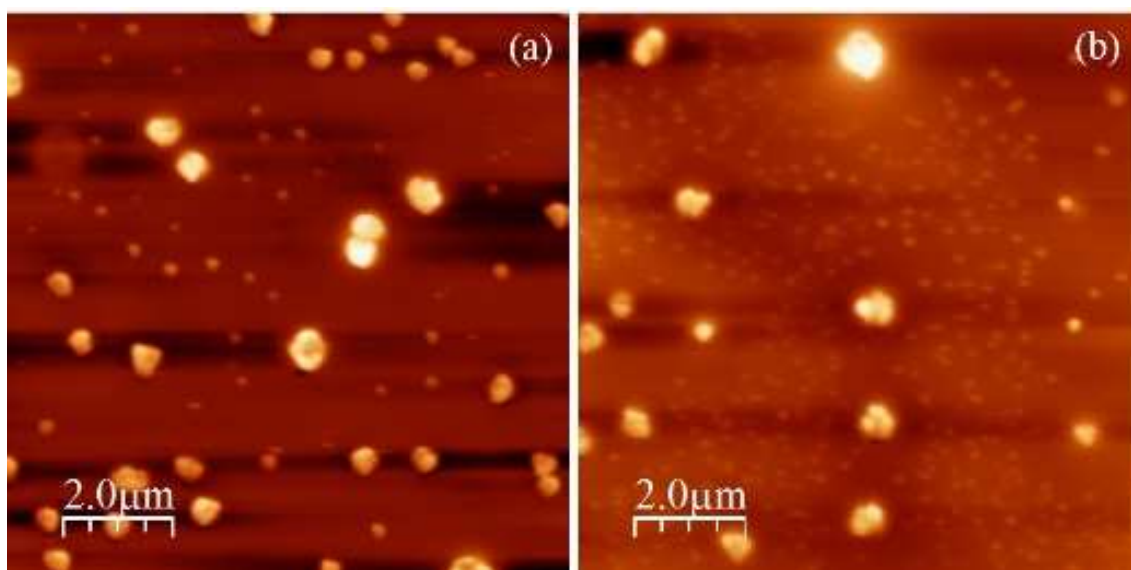


Fig. 75 AFM images of GNPs synthesized at different lots of PMMA. (a) 330,000 g/mol and (b) 120,000 g/mol. Samples prepared at the same spin-coating parameters on Si-As substrates using 100 mg of HAuCl₄ precursor.

